博士論文

Spin dynamics at finite temperatures in the Kitaev model
（キタエフ模型における有限温度スピンダイナミクス）

吉竹　純基

Doctor thesis

Spin dynamics at finite temperatures in the Kitaev model

Junki Yoshitake

Acknowledgement

I would like to express my sincere gratitude to Prof. Yukitoshi Motome for his supervision during my master and doctoral programs, and duration of research student and technical assistant, for nine years. Countless discussions and communications with him gave me priceless opportunities to foster a sense of physics and the way of consideration. I would also like to thank Dr. Yasuyuki Kato and Dr. Joji Nasu for their instructive guidances and constructive discussions. I would be grateful to the referees of the dissertation defense, Prof. Masatoshi Imada, Prof. Yoshinori Tokura, Prof. Kazushi Kanoda, and Prof. Masafumi Udagawa for reviewing this thesis and valuable comments. I acknowledge excellent discussions with Prof. Yoshitomo Kamiya, Prof. Takahiro Misawa, and Prof. Youhei Yamaji. I would like to extend my thanks to all the previous and present members of Motome, Imada and Nagaosa groups for kind supports and fruitful discussions. I wish to appreciate helpful supports from the secretaries Ms. Aya Kitano, Ms. Keiko Niwa, Ms. Michiko Takemoto, Ms. Tae Tokuyoshi, and Ms. Yasuko Tanaka. Some of the calculations were performed at the Supercomputer Center, Institute for Solid State Physics (ISSP), the University of Tokyo. I appreciate my family supporting my decisions and encouraging me to explore the research life.

Abstract

The quantum spin liquid (QSL), which does not show any long-range ordering down to the lowest temperature (T), has attracted broad interest as a new quantum state of matter. Recently, the Kitaev model was proposed as a canonical model to realize QSL ground state. The model has conserved quantities whose number is proportional to the system size, and the ground state is exactly shown to be a QSL by rewriting the model by using Majorana fermion operators. The exact solution elicits fractionalization of spin degrees of freedom into matter fermions and Z_2 fluxes. Following the prediction on the experimental realization of the Kitaev model, tremendous efforts have been paid for the search of the Kitaev QSLs in this decade. Theoretically, it was shown that the spin fractionalization strongly affects the T and energy dependences of various physical properties. Such characteristic features were indeed observed in candidate materials, such as iridium oxides $A_2\mathrm{IrO}_3$ (A=Na, Li) and a ruthenium halide α-RuCl_3. Such collaborative research between theory and experiment has brought considerable progress in understanding of QSLs, but the study was not extended to the spin dynamics at finite T thus far. Theoretical studies of dynamical properties at finite T for the Kitaev model remain a big challenge, despite the importance for experimental identification of the Kitaev QSL. This is because, for obtaining the dynamical spin correlations, one needs to include the time evolution of conserved quantities, which was hard to treat in the theoretical methods used in the previous studies.

In this thesis, we investigate spin dynamics at finite T for the Kitaev model by developing new numerical techniques, the cluster dynamical mean-field theory (CDMFT) and the continuous-time quantum Monte Carlo (CTQMC) method on the basis of a Majorana fermion representation. These methods were originally developed for correlated electron systems. We reformulate them in the Majorana fermion representation so as to be applicable to the Kitaev model. In the CDMFT, by introducing the cluster approximation, we can exactly take the summation with respect to the configurations of conserved quantities. Thus, this method provides an alternative of the quantum Monte Carlo (QMC) method developed in the previous study. The advantages of the CDMFT lie in the small calculation cost and the exact enumeration without statistical errors. On the other hand, the CTQMC enables us to treat the time evolution of local conserved quantities and calculate dynamical spin correlations for each configuration of conserved quantities. By combining CTQMC with CDMFT (CDMFT+CTQMC) or QMC (QMC+CTQMC), we calculate the magnetic susceptibility (χ), dynamical spin structure factor ($S(\mathbf{q},\omega)$), and relaxation time in the nuclear magnetic resonance ($1/T_1$) for the Kitaev models on the 2D honeycomb and 3D hyperhoneycomb structures.

We find that the dynamical quantities show peculiar T and energy dependences in the paramagnetic state when approaching the QSL ground state by decreasing T. The most prominent feature is the dichotomy between static and dynamical

spin correlations as a consequence of the spin fractionalization. At sufficiently high T, $S(\mathbf{q},\omega)$ shows almost featureless spectrum around $\omega \simeq 0$. While decreasing T below $T_{\rm H}$, the spectral weight shifts to a high ω region, and starts to acquire small wave number dependence. The shift corresponds to the increase of kinetic energy of matter fermions. With a further decrease of T, a quasi-elastic peak appears around $\omega \simeq 0$, and rapidly grows toward $T_{\rm L}$. Below $T_{\rm L}$, the quasi-elastic peak shift to a nonzero ω, reflecting the flux gap in the ground state. The dichotomy appears more clearly in the increase of $1/T_1$ below $T_{\rm H}$ where the fractionalization sets in, despite the saturation of static spin correlations. While further decreasing T, $1/T_1$ shows a peak slightly above $T_{\rm L}$, and then rapidly decreases to zero. This nonmonotonic T dependence is a consequence of the spin fractionalization and different energy scales of matter fermion and Z_2 fluxes. Meanwhile, χ follows the Curie-Weiss law at sufficiently high T, whereas it shows a deviation below $T_{\rm H}$. After showing a broad peak between $T_{\rm H}$ and $T_{\rm L}$, χ decreases substantially around $T_{\rm L}$, and converges to a nonzero value in the low T limit. The decrease around $T_{\rm L}$ can be ascribed to suppression of flux excitations. The nonzero value of χ in the low T limit is generic to the systems which do not conserve the total z component of spins. We also find that overall T dependences of $S(\mathbf{q},\omega)$, $1/T_1$, and χ are unchanged for the 2D and 3D cases, whereas in the 3D case, a phase transition at low T brings about singular T dependences of the dynamical quantities.

We discuss our theoretical results in comparison with other theoretical results for the Kitaev model and experimental results for the Kitaev candidate materials. In the comparison with the classical version of the Kitaev model, we find that the high-T and large-ω behaviors are common to the quantum and classical cases. On the other hand, there are significant differences in the low-T and small-ω properties, which are associated with gap opening in the Z_2 flux excitations in the quantum case. We also compare our results with the experimental results of $S(\mathbf{q},\omega)$, $1/T_1$, and χ for the Kitaev materials. Our results for the Kitaev model well explain the high-T behaviors of $S(\mathbf{q},\omega)$ and $1/T_1$ in experiments. On the other hand, the low-T features of $1/T_1$ and χ in our results are masked by the magnetic ordering or modified by unknown reasons in the candidate materials. However, when the magnetic orders are suppressed by applying the magnetic field, peculiar behaviors are experimentally observed for $S(\mathbf{q},\omega)$ and $1/T_1$ even at low T, which are, at least, qualitatively explained by out results for the Kitaev model at zero field. The agreement suggests the possibility of field-induced Kitaev QSLs.

Thus, through the development of new numerical techniques, we have clarified that the experimentally-measurable dynamical quantities of the Kitaev model show peculiar T and energy dependences, reflecting the fractionalization of spin degrees of freedom. Some of the peculiar behaviors are observed in the experimental results of Kitaev candidate materials, which are supportive of the realization of the Kitaev QSL. Our findings will significantly contribute to further exploration of the Kitaev QSLs in collaborative research between theory and experiment.

List of publications

- J. Yoshitake, J. Nasu, and Y. Motome, *Fractional Spin Fluctuation as a Precursor of Quantum Spin Liquids: Majorana Dynamical Mean-Field Study for the Kitaev Model*, Phys. Rev. Lett. **117**, 157203 (2016).
- J. Yoshitake, J. Nasu, Y. Kato, and Y. Motome, *Majorana dynamical mean-field study of spin dynamics at finite temperatures in the honeycomb Kitaev model*, Phys. Rev. B **96**, 024438 (2017).
- J. Yoshitake, J. Nasu, and Y. Motome, *Temperature evolution of spin dynamics in two- and three-dimensional Kitaev models: Influence of fluctuating Z_2 flux*, Phys. Rev. B **96**, 064433 (2017).

Related publications

- J. Nasu, Y. Kato, J. Yoshitake, Y. Kamiya, and Y. Motome, *Spin-Liquid-to-Spin-Liquid Transition in Kitaev Magnets Driven by Fractionalization*, Phys. Rev. Lett. **118**, 137203 (2017).
- S.-H. Do, S.-Y. Park, J. Yoshitake, J. Nasu, Y. Motome, Y. S. Kwon, D. T. Adroja, D. J. Voneshen, K. Kim, T.-H. Jang, J.-H. Park, K.-Y. Choi, and S. Ji, *Majorana fermions in the Kitaev quantum spin system α-$RuCl_3$*, Nature Physics **13**, 1079 (2017).
- J. Nasu, J. Yoshitake, and Y. Motome, *Thermal Transport in the Kitaev Model*, Phys. Rev. Lett. **119**, 127204 (2017).
- Y. Nagai, T. Jinno, J. Yoshitake, J. Nasu, Y. Motome, M. Itoh, and Y. Shimizu, *Two-step gap opening across the quantum critical point in a Kitaev honeycomb magnet*, arXiv:1810.05379.

Contents

Acknowledgement i

Abstract ii

List of publications iv

Related publications v

1 Introduction 1
- 1.1 Quantum spin liquids . . . 1
- 1.2 Kitaev quantum spin liquid . . . 3
  - 1.2.1 Kitaev model and the exact solution . . . 3
  - 1.2.2 Fractional excitations and phase diagram . . . 5
  - 1.2.3 Kitaev interactions in real materials . . . 6
  - 1.2.4 Stability of the Kitaev spin liquid . . . 9
- 1.3 Candidate materials for the Kitaev spin liquid . . . 11
  - 1.3.1 Na_2IrO_3, α-Li_2IrO_3, and $H_3LiIr_2O_6$ . . . 11
  - 1.3.2 α-$RuCl_3$ . . . 12
  - 1.3.3 β- and γ-Li_2IrO_3 . . . 13
- 1.4 Signatures of the Kitaev quantum spin liquid . . . 14
  - 1.4.1 Thermal fractionalization . . . 14
  - 1.4.2 Dynamical spin structure factor in the ground state . . . 18
  - 1.4.3 Raman scattering . . . 20
- 1.5 Purpose of this thesis . . . 22
- 1.6 Organization of this thesis . . . 24

2 Model 25
- 2.1 Jordan-Wigner transformation . . . 25
- 2.2 Majorana fermion representation . . . 27

3 Method 29
- 3.1 Quantum Monte Carlo method . . . 29
- 3.2 Cluster dynamical mean-field theory . . . 31
- 3.3 Continuous-time quantum Monte Carlo method . . . 34
- 3.4 Maximum entropy method . . . 37
- 3.5 Physical quantities . . . 38

4 Results by CDMFT + CTQMC method **41**
4.1 Benchmark . . . 41
4.1.1 CDMFT method . . . 41
4.1.2 CDMFT+CTQMC method . . . 43
4.2 Dynamical spin structure factor . . . 45
4.3 NMR relaxation rate . . . 53
4.4 Magnetic susceptibility . . . 55
4.5 Korringa ratio . . . 56
4.6 Effect of the Z_2 variables $\{\eta_r\}$ on the dynamical properties . . . 60
4.7 Summary of this chapter . . . 63

5 Results by QMC + CTQMC method **65**
5.1 Results for 2D honeycomb structure . . . 66
5.1.1 Magnetic susceptibility and NMR relaxation rate . . . 66
5.1.2 Dynamical spin structure factor . . . 68
5.2 Results for 3D hyperhoneycomb structure . . . 72
5.2.1 Magnetic susceptibility and NMR relaxation rate . . . 72
5.2.2 Dynamical spin structure factor . . . 73
5.3 Comparison between 2D and 3D results . . . 76
5.4 Summary of this chapter . . . 77

6 Discussion **78**
6.1 Comparison with theoretical results . . . 78
6.1.1 Classical Kitaev model . . . 78
6.1.2 Other calculations for the quantum Kitaev model . . . 81
6.2 Comparison with experimental results . . . 83
6.2.1 Dynamical spin structure factor . . . 83
6.2.2 NMR relaxation rate . . . 86
6.2.3 Magnetic susceptibility . . . 89
6.3 Summary of this chapter . . . 90

7 Summary **92**

A Kitaev Hamiltonian in reciprocal space **96**

B Plots of $1/T_1$ and χ in the T-linear scale **98**

C Benchmark of the maximum entropy method **102**

D Low-T behavior of χ **106**

E Convergence of the hybridization expansion in QMC+CTQMC calculations **108**

1
Introduction

1.1 Quantum spin liquids

Matter can exist in one of three states: solid, liquid, or gas. Solid breaks a translational or rotational symmetry. Meanwhile, both liquid and gas preserve the translational and rotational symmetries, and hence, they are distinguished from solid by phase transitions with symmetry breaking. While there is also a phase transition between liquid and gas, the two states can be connected adiabatically by bypassing the end point of the transition line because they share the same symmetry.

We can conceive analogs of the three states of matter in spin states of magnetic materials. A spin-disordered paramagnetic state at sufficiently high temperature (T) corresponds to gas, as it preserves all the symmetries of the system. At low T, most magnets exhibit magnetic orders, such as ferromagnetic (FM) and antiferromagnetic (AFM) orders. Such ordered phases are regarded as solid, as it breaks some symmetries of the system, e.g., time reversal symmetry. The two states, the paramagnetic and ordered states, are distinguished by a phase transition, similar to gas and solid in conventional matters.

Then, what is the spin state corresponding to liquid? Is there a spin state which is distinguished from the paramagnetic state but still preserves all the symmetries of the system? The answer is yes. Such a state is called a quantum spin liquid (QSL). The concept of the QSL was first introduced by P. W. Anderson [1]. As an example of the QSL, he introduced the resonating valence bond (RVB) state as a possible ground states for two-dimensional (2D) quantum spin systems. The RVB state is defined by a superposition of all possible valence bond states (direct products of spin-singlet dimers), which preserves all the symmetries of the system.

The QSLs cannot be distinguished from the paramagnetic state by the conventional symmetry argument. This has stimulated the development of new concepts to characterize the apparently featureless QSLs. One is the topological order [2–4]. It is distinct from the conventional orders defined by local order parameters, and able to characterize the topological nature of the system dictated by long-range quantum entanglement and nontrivial ground-state degeneracy. A well-known example of the topological order is found for the fractional quantum Hall states [4–6]. Another new concept is fractional excitations [7]. In the QSLs, the elementary spin excitations can be fractionalized into new quasiparticles. For example, in the RVB state, spin excitations are fractionalized into emergent quasiparticles called spinons and visons [8, 9]. The spinon is a particle-like excitation carrying no charge but spin $S = 1/2$. Meanwhile, the vison is a topological excitation characterized by the parity of broken singlet pairs by its trace.

Owing to the exotic nature, the QSLs have been long sought since the proposal by Anderson. In particular, the possibility of the RVB ground state has been intensively studied, since it was considered to have relevance to high-temperature superconductivity [10]. Through the studies for decades, there have been found several candidate materials for QSLs, especially in the systems on triangular-based lattice structures [11,12]. A typical example is an organic Mott insulator κ-$(ET)_2Cu_2(CN)_3$ with a quasi-2D structure of triangular layers. The material exhibits no magnetic ordering even at tens of mK, which is four orders of magnitude lower than the energy scale of the dominant exchange interactions [13]. Other examples are found in another organic material $EtMe_3Sb[Pd(dmit)_2]_2$ with similar triangular layers [14], copper oxides with layered kagome structures, e.g., $Cu_3V_2O_7(OH)_2{\cdot}2H_2O$, $ZnCu_3(OH)_6Cl_2$, and $BaCu_3V_2O_8(OH)_2$ [15–17], and an iridium oxide $Na_4Ir_3O_8$ with the so-called hyperkagome structure [18]. In these triangular-based lattice systems, the AFM exchange interactions compete with each other, which prevents the systems from magnetic ordering. These are called geometrically frustrated magnets. On the theoretical side, the QSLs in such geometrically frustrated magnets have long been studied by many different theoretical methods [19, 20]. Despite the tremendous efforts, it remains elusive whether the QSLs like the RVB state are realized in realistic Hamiltonians relevant to the experiments. This is mainly because of the keen competition between energetically-degenerate states and the difficulty in the application of reliable theoretical methods.

Another route to the QSLs has been studied in magnets with the frustration between directionally-dependent exchange interactions [21–25]. Such directional dependence originates from the coupling between the spin and orbital degrees of freedom, via the relativistic spin-orbit coupling and the spin-orbital coupled exchange interactions under strong electron correlations. In contrast to the geometrical frustration, the frustration from the directionally dependent interactions may arise even on geometrically nonfrustrated lattice structures.

In 2006, A. Kitaev proposed a simple spin model [26], which brought a breakthrough in the research of QSLs. The model belongs to the second category of the frustrated magnets: it is defined on a nonfrustrated honeycomb structure with directionally-dependent exchange interactions. What distinguishes this Kitaev model from others is twofold. One is that the model has an exact solution for the ground state and it is a QSL [26]. The exact solution allows us to clarify the nature of the QSL without any approximation, not only in the ground state but also at finite T, by treating the fractional excitations explicitly. The other distinguished aspect is that the model gives a good description for some magnetic materials [27]. This allows us to study the QSL through the cooperative studies between theories and experiments. These virtues will be reviewed in the following sections.

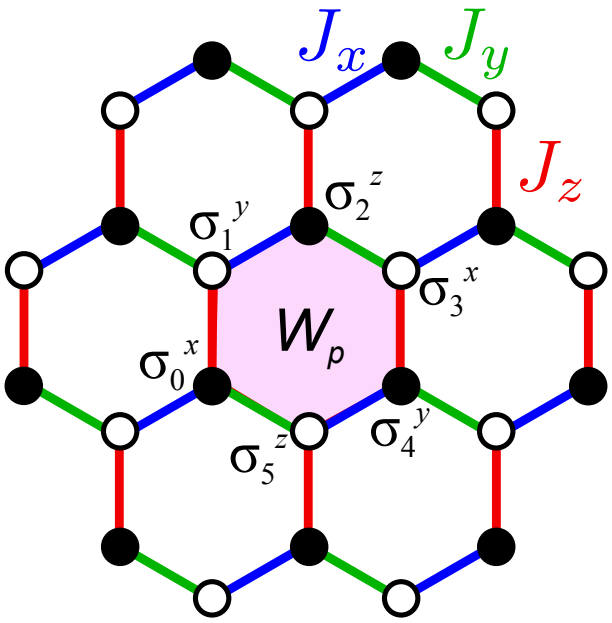

Figure 1.1: Schematic picture of the Kitaev model on the 2D honeycomb structure. The blue, green, and red bonds represent the x, y, and z bonds in Eq. (1.1), respectively. The magenta hexagon represents a conserved quantity W_p defined by a product of spin operators on the vertices of the hexagon; see Eq. (1.2). The black and white circles denote the sites j and j' in Eq. (1.10), respectively. They also correspond to b and w in Eq. (2.13).

1.2 Kitaev quantum spin liquid

1.2.1 Kitaev model and the exact solution

The Kitaev model is a quantum spin model on a 2D honeycomb structure, whose Hamiltonian is given by [26]

$$\mathcal{H} = -J_x \sum_{\langle j,j' \rangle_x} S_j^x S_{j'}^x - J_y \sum_{\langle j,j' \rangle_y} S_j^y S_{j'}^y - J_z \sum_{\langle j,j' \rangle_z} S_j^z S_{j'}^z, \tag{1.1}$$

where S_j^γ represents the γ component of the $S = 1/2$ spin operator ($\gamma = x, y, z$) defined by the Pauli matrix σ_j^γ as $S_j^\gamma = \frac{1}{2}\sigma_j^\gamma$, and $\langle j, j' \rangle_\gamma$ represents the nearest-neighbor (NN) bonds in three different directions, as shown in Fig. 1.1. In this model, although the lattice structure is bipartite (no geometrical frustration), there is severe frustration arising from competition between the three bond-dependent Ising-type interactions. Indeed, the classical analog of this model leads to macroscopic degeneracy in the ground state. Nonetheless, the quantum version is exactly solvable [26] and the obtained ground state is a QSL (see Sec. 1.2.2).

A key aspect of the model for obtaining the exact solution is the existence of the macroscopic number of conserved quantities. The conserved quantity is defined by

a product of six Pauli matrices for each hexagonal plaquette p as

$$W_p = \sigma_0^x \sigma_1^y \sigma_2^z \sigma_3^x \sigma_4^y \sigma_5^z, \tag{1.2}$$

as shown in Fig. 1.1. W_p commutes with not only the Hamiltonian in Eq. (1.1) but also W_p for other plaquette, namely,

$$[W_p, \mathcal{H}] = 0 \quad \text{for all } p, \tag{1.3}$$
$$[W_p, W_{p'}] = 0 \quad \text{for } p \neq p'. \tag{1.4}$$

Besides, W_p satisfies $W_p^2 = 1$. Hence, W_p can be diagonalized simultaneously with the Hamiltonian, and the eigenvalue takes ± 1, which is called a Z_2 flux. The existence of the conserved quantities W_p allows us to solve the problem in each subspace specified by the eigenvalues of W_p as shown below.

The ground state of the model in Eq. (1.1) is exactly obtained by introducing Majorana fermion operators. Following the seminal paper by Kitaev [26], we introduce four Majorana fermion operators, c_j and b_j^γ with $\gamma = x, y, z$, for each spin operator. Thus, in this representation, the Hilbert space in the original spin representation, 2^N, is extended to 4^N (N is the number of spins). The Majorana fermion operators satisfy the following anticommutation relations:

$$\{c_j, c_{j'}\} = 2\delta_{j,j'}, \tag{1.5}$$
$$\{b_j^\gamma, b_{j'}^{\gamma'}\} = 2\delta_{j,j'}\delta_{\gamma,\gamma'}, \tag{1.6}$$
$$\{c_j, b_{j'}^\gamma\} = 0. \tag{1.7}$$

Then, when one introduces an operator $\tilde{S}_j^\gamma = \frac{i}{2} b_j^\gamma c_j$ in the extended Hilbert space, it satisfies the relation

$$\tilde{S}_j^x \tilde{S}_j^y \tilde{S}_j^z = \frac{i}{8} b_j^x b_j^y b_j^z c_j = \frac{i}{8} D_j, \tag{1.8}$$

where $D_j = b_j^x b_j^y b_j^z c_j$. This is similar to the relation for the spin $S = 1/2$ operators S_j^γ, except for the factor of D_j. Thus, if we restrict ourselves to the subspace in which all the eigenvalues of D_j are 1, $\tilde{S}_j^\gamma$ can be regarded as the spin operator S_j^γ (the restricted subspace is called the physical subspace). Note that we can diagonalize D_j for all j simultaneously with the Hamiltonian and that the eigenvalues of D_j take ± 1, as D_j commutes with the Hamiltonian and other $D_{j'}$ and as $D_j^2 = 1$.

This Majorana representation allows us to solve the problem by considering the Hamiltonian in the extended Hilbert space instead of that in the original Hilbert space by replacing S_j^p by $\tilde{S}_j^p$; the physical solution is given by projecting the obtained eigenstates to the physical subspace. The projection is executed by multiplying the projection operator

$$\mathcal{P} = \prod_j \frac{D_j + 1}{2}, \tag{1.9}$$

to a state in the extended Hilbert space.

The benefit to consider the extended Hilbert space is that the Hamiltonian is easy to handle. In the extended Hilbert space, the Hamiltonian in Eq. (1.1) is written as

$$\tilde{\mathcal{H}} = i\frac{J_x}{4}\sum_{(j,j')_x} u^x_{j,j'}c_j c_{j'} + i\frac{J_y}{4}\sum_{(j,j')_y} u^y_{j,j'}c_j c_{j'} + i\frac{J_z}{4}\sum_{(j,j')_z} u^z_{j,j'}c_j c_{j'}, \tag{1.10}$$

where the sum over $(j,j')_\gamma$ is taken for the NN sites on a γ bond with $j \in b$ and $j' \in w$ (see Fig. 1.1); $u^\gamma_{j,j'} = ib^\gamma_j b^\gamma_{j'}$ is defined on each γ bond connecting j and j' sites, and it satisfies $u^\gamma_{j,j'} = -u^\gamma_{j',j}$.

In Eq. (1.10), $u^\gamma_{j,j'}$ can be treated as a Z_2 variable taking ± 1, as $u^\gamma_{j,j'}$ commutes with the total Hamiltonian as well as with other $u^{\gamma'}_{k,k'}$ and as $(u^\gamma_{j,j'})^2 = 1$, similar to W_p. Thus, the model in Eq. (1.10) describes itinerant free Majorana fermions $\{c_j\}$ (called matter fermions) coupled to the Z_2 variables $u^\gamma_{j,j'}$. The Hamiltonian in Eq. (1.10) can be diagonalized in each subspace specified by the eigenvalues of $u^\gamma_{j,j'}$, in the same manner by W_p. In fact, there is a relation between $u^\gamma_{j,j'}$ and W_p: W_p is given as a product of $u^\gamma_{j,j'}$ on the six edges surrounding the plaquette. For instance,

$$W_p = u^z_{0,1}u^x_{1,2}u^y_{2,3}u^z_{3,4}u^x_{4,5}u^y_{0,5}, \tag{1.11}$$

for the example shown in Fig. 1.1.

For a given set of $u^\gamma_{j,j'}$, $\{u^\gamma_{j,j'}\}$, it is easy to obtain the lowest-energy state in the subspace specified by $\{u^\gamma_{j,j'}\}$, as it is a noninteracting one-body fermion problem. Then, the ground state of the model in Eq. (1.10) is the one with the lowest energy $E_0(\{u^\gamma_{j,j'}\})$ among all possible $\{u^\gamma_{j,j'}\}$. According to Lieb's theorem [28], one can show that the lowest-energy state is given by $\{u^\gamma_{j,j'}\}$ with all $u^\gamma_{j,j'} = 1$ for $j \in b$ and $j' \in w$ (see Fig. 1.1), when, at least, two of J_γ are equal (the model is symmetric with respect to mirror reflection). To obtain the physical solution, one needs to project the obtained solution in the extended Hilbert space to the physical subspace, as described above. For the eigenvalue, the multiplication of the projection operator $\mathcal{P}$ in Eq. (1.9) does not change the result as $\mathcal{P}$ commutes with the Hamiltonian. Meanwhile, the projection of the eigenstate does not result in a null vector and gives the ground state. This is guaranteed by the facts that D_j anticommutes with $u^\gamma_{j,j'}$ and that all $u^\gamma_{j,j'} = 1$ for the ground state before the projection.

1.2.2 Fractional excitations and phase diagram

There are two types of elementary excitations from the ground state. One is an excitation of matter fermions $\{c_j\}$, which does not change $\{W_p\}$, and the other is given by flipping W_p. Thus, the spin excitations in the Kitaev model are fractionalized into the excitations of matter fermions and Z_2 fluxes.

The excitation spectrum of the matter fermions is obtained by solving the free fermion problem for the subspace of all $W_p = 1$. The result is given by gapless or gapped excitations depending on the parameters of the model, J_x, J_y, and J_z, as shown in the phase diagram in Fig. 1.2 [26]. The gapless phase appears around the isotropic point with $J_x = J_y = J_z$, whereas the gapped phases exist in the regions

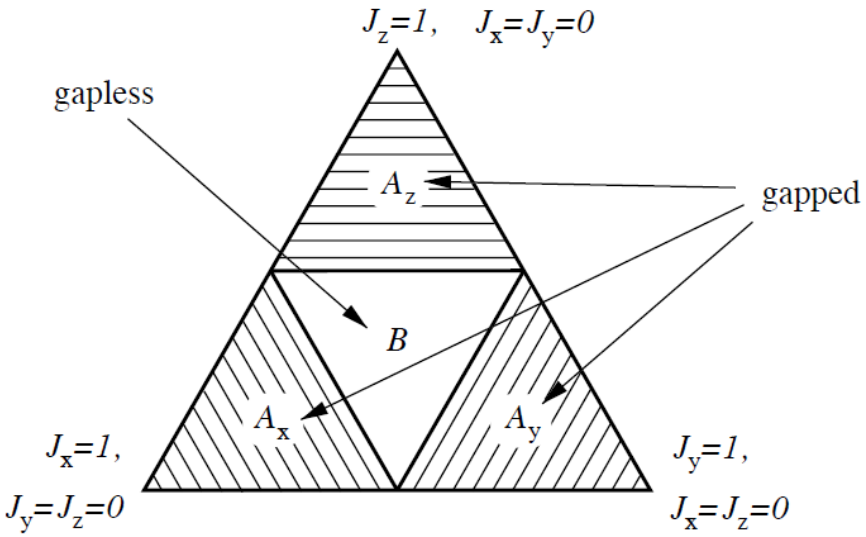

Figure 1.2: Phase diagram of the Kitaev model. The triangle is the section of the positive octant ($J_x, J_y, J_z \geq 0$) by the plane $J_x + J_y + J_z = 1$. The figure is taken from Ref. [26].

with strong anisotropy. On the other hand, the the spectrum for excitations by flipping W_p is always gapped.

Both gapless and gapped phases in Fig. 1.2 are shown to be QSLs with extremely short-range spin correlations: the spin correlations are nonzero only for the NN bonds as well as the same site [29]. This peculiar nature comes from the conservation of the fluxes $\{W_p\}$. For any operator, the expectation value vanishes when it changes the configurations of W_p. The spin correlation is defined by a product of two spin operators, $S_j^\gamma S_{j'}^{\gamma'}$. It conserves all W_p only if $\gamma = \gamma'$ and j and j' are on a NN γ bond, which is confirmed by the definition of W_p in Eq. (1.2). This means that, in addition to the trivial nonzero component for the same site with $j = j'$, the spin correlations remain nonzero only for $\langle S_j^\gamma S_{j'}^\gamma \rangle$ with j and j' on a γ bond at all temperatures, including the ground state.

Although the original work by Kitaev was done for the model on the honeycomb structure, all the procedures for obtaining the exact solution are common to extensions of the model to other tricoordinate structures where similar three types of bond-dependent interactions can be defined. Such extensions have been studied in both two and three dimensions [30–37].

1.2.3 Kitaev interactions in real materials

As shown in Eq. (1.1), the Kitaev model has the Ising-type anisotropic interactions that depend on the bond directions. In the pioneering work, Kitaev wrote "it would be interesting to find a solid state realization" of such interactions [26]. This interesting possibility was theoretically studied by G. Jackeli and G. Khaliullin; they

showed that the bond-dependent Ising interactions can be realized in Mott insulators with the strong relativistic spin-orbit coupling [27]. We will briefly review their arguments below.

We start from an isolated magnetic ion with five d electrons in the t_{2g} manifold under an octahedral crystal field, which comprises the low-spin $(t_{2g})^5$ configuration. The spin-orbit coupling splits the sixfold degeneracy of the one-body t_{2g} states into lower-energy fourfold states with the total angular momentum $j_{\rm eff} = 3/2$ and higher-energy twofold states with the total angular momentum $j_{\rm eff} = 1/2$, as shown in Fig. 1.3(a). In the $(t_{2g})^5$ case, the fourfold $j_{\rm eff} = 3/2$ states are fully occupied, and the twofold $j_{\rm eff} = 1/2$ states are occupied by the rest one electron, resulting in half filling of the $j_{\rm eff} = 1/2$ states. This situation is realized in some $4d$ and $5d$ ions, such as Ru^{3+}, Ir^{4+}, and Rh^{4+} surrounded by octahedral ligands.

The spin-orbital entangled states with $j_{\rm eff} = 1/2$ are described by coherent superpositions of different orbital and spin states as [27]

$$\left| j^z_{\rm eff} = \pm\frac{1}{2} \right\rangle = \frac{1}{\sqrt{3}} \left(-\left| s^z = \pm\frac{1}{2}, l^z_{\rm eff} = 0 \right\rangle + \left| s^z = \mp\frac{1}{2}, l^z_{\rm eff} = \mp 1 \right\rangle \right). \tag{1.12}$$

Here, $|s^z = \pm\frac{1}{2}\rangle$ represent the states with spin $s^z = \pm\frac{1}{2}$, and $|l^z_{\rm eff} = 0, \pm 1\rangle$ represent the states with the effective orbital angular momentum $l^z_{\rm eff} = 0, \pm 1$, which are related with the t_{2g} orbital basis as

$$|l^z_{\rm eff} = 0\rangle = |xy\rangle, \tag{1.13}$$

$$|l^z_{\rm eff} = \pm 1\rangle = -\frac{1}{\sqrt{2}}(i|zx\rangle \pm |yz\rangle). \tag{1.14}$$

The $j_{\rm eff} = 1/2$ states in Eq. (1.12) comprise a time-reversal Kramers pair. This allows us to treat them as the isospin states with the effective magnetic moment of $1/2$.

When the magnetic ions are aligned periodically to form a crystal, they start to interact with each other. If the Coulomb repulsion is strong enough, the half-filled $j_{\rm eff} = 1/2$ states give rise to a Mott insulating state. This is called the spin-orbit Mott insulator [38]. In this case, we can derive the effective magnetic interactions between the localized $j_{\rm eff} = 1/2$ isospins, by taking into account the electron hopping as a perturbation.

To derive the effective magnetic interactions, let us consider two octahedra of ligands, each of which capsules a magnetic ion in the $j_{\rm eff} = 1/2$ state. Suppose the two octahedra are connected with sharing one ligand edge on the xy plane, as shown in Fig. 1.3(b). In the perturbation theory, we consider an indirect electron hopping between the two magnetic ions via one of the shared ligands, which we call the d-p-d hopping. In the case of the ideal octahedra, from the symmetry, the d-p-d hopping has nonzero matrix element only between the zx and yz orbitals or the yz and zx orbitals via the p_z orbital of the ligand; see Fig. 1.3(b). The hopping Hamiltonian is described as

$$\mathcal{H}_t = -t \sum_{\sigma} (c^\dagger_{0,zx,\sigma} c_{1,yz,\sigma} + c^\dagger_{0,yz,\sigma} c_{1,zx,\sigma} + \text{h.c.}), \tag{1.15}$$

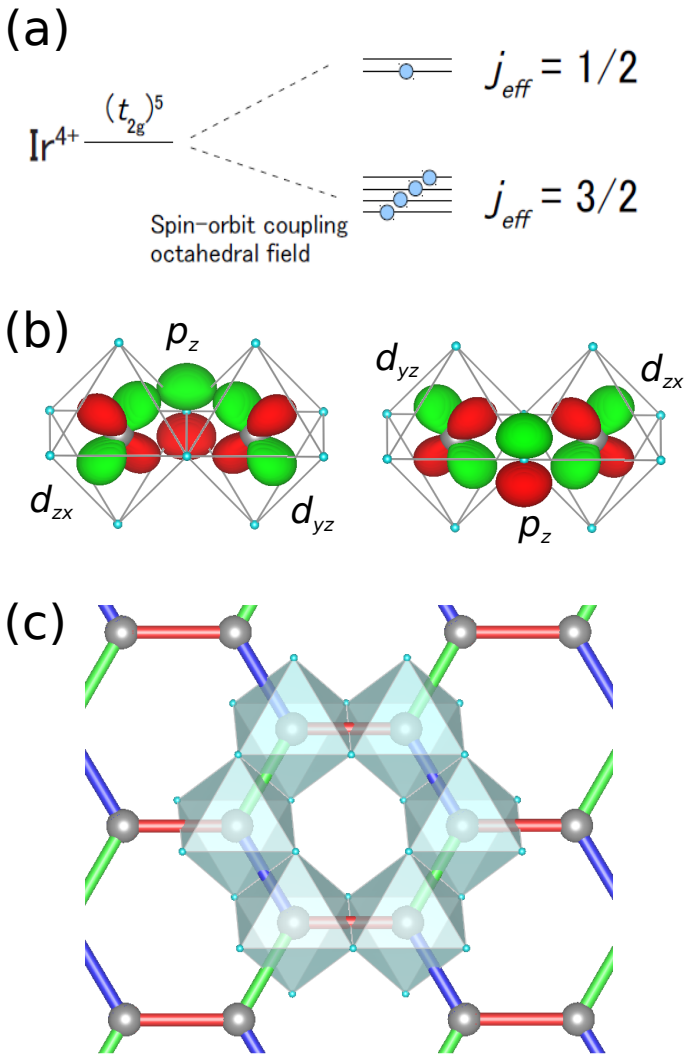

Figure 1.3: (a) Schematic picture of the energy splitting of the sixfold t_{2g} states into the fourfold $j_{\rm eff} = 3/2$ states and the twofold $j_{\rm eff} = 1/2$ states. (b) Schematic pictures of edge-sharing octahedra with two different d-p-d hopping processes in Eq. (1.15). Magnetic ions locate at the centers of each octahedron, whereas ligands locate at the vertices of the octahedra. The red and green ovals represent the d and p orbitals indicated in the figures, respectively. (c) Schematic picture of a honeycomb network composed of edge-sharing octahedra.

where $c^\dagger_{j,\mu,\sigma}$ ($c_{j,\mu,\sigma}$) is a creation (annihilation) operator for $\mu = yz, zx$ orbital at site $j = 0, 1$ with spin $\sigma = \uparrow, \downarrow$.

In this setup, we consider the second-order perturbation in terms of $\mathcal{H}_t$. As the intermediate states in the perturbation, all $(t_{2g})^4$ and $(t_{2g})^6$ states are taken into account. The resulting effective Hamiltonian is given in the form of [27]

$$\mathcal{H}_{\rm eff} = -JS^z_0 S^z_1. \tag{1.16}$$

Thus, the effective magnetic interaction has Ising-type anisotropy. Note that the

result in Eq. (1.16) is derived for the two octahedra sharing the edge on the xy plane. For edge-sharing on a different plane, we obtain a similar Ising-type interaction with a different spin component.

Therefore, if the crystal is composed of a honeycomb network of the edge-sharing octahedra as shown in Fig. 1.3(c), the effective magnetic interactions between the $j_{\rm eff} = 1/2$ isospins are of Ising type with the x, y, and z component for three different bond directions. This is nothing but the Kitaev model in Eq. (1.1).

In the arguments above, only the *d*-*p*-*d* hopping for the ideal octahedra is taken into account. In reality, there are additional contributions from other hopping processes like the *d*-*d* direct hopping and the distortions of the octahedra [39–43] . These lead to another types of magnetic interactions, e.g., the isotropic Heisenberg exchange interaction [Eq. (1.18)] and the symmetric off-diagonal interaction [Eq. (1.19)]. As will be seen in the next subsection, however, the Kitaev spin liquid remains stable against such additional interactions when they are small.

Although the arguments above are for the $(t_{2g})^5$ systems, there were also several theoretical studies which predict another platform to realize the Kitaev-type interactions. One possibility is the high-spin $(t_{2g})^5$-$(e_g)^2$ systems, where similar $j_{\rm eff} = 1/2$ states appear in the presence of the strong spin-orbit coupling [44, 45]. Another candidates are studied for f-electron compounds [46–48] .

1.2.4 Stability of the Kitaev spin liquid

In real materials, as discussed above, there might be subdominant interactions in addition to the Kitaev-type interactions. To clarify the effect of such additional interactions, several extensions of the Kitaev model have been studied. For instance, the model which includes all the symmetry-allowed magnetic interactions for nearest-neighbor spins has been intensively studied; the Hamiltonian is given by

$$\mathcal{H}_{\rm total} = \mathcal{H}_{\rm Kitaev} + \mathcal{H}_{\rm Heisenberg} + \mathcal{H}_{\Gamma} \tag{1.17}$$

where $\mathcal{H}_{\rm Kitaev}$ is the Kitaev Hamiltonian in Eq. (1.1),

$$\mathcal{H}_{\rm Heisenberg} = -J_{\rm Heisenberg} \sum_{\langle j,k \rangle} \mathbf{S}_i \cdot \mathbf{S}_j, \tag{1.18}$$

$$\mathcal{H}_{\Gamma} = -\sum_{\gamma=x,y,z} J_{\Gamma}^{\gamma} \sum_{\langle j,k \rangle_{\gamma}} (S_j^{\alpha} S_k^{\beta} + S_j^{\beta} S_k^{\alpha}). \tag{1.19}$$

Here, Eq. (1.18) describes the isotropic Heisenberg exchange interactions, and Eq. (1.19) represents the symmetric off-diagonal interactions, where α and β denote the two spin components besides γ.

The ground state of the model in Eq. (1.17) has been studied by many theoretical methods, e.g., the exact diagonalization method, the density matrix renormalization group method, and the tensor-network method [49–54].

A representative result obtained by the exact diagonalization for a 24-site cluster is shown in Fig. 1.4 [50]. Here, $\mathcal{H}_{\Gamma}$ in Eq. (1.19) is omitted, and the model is called

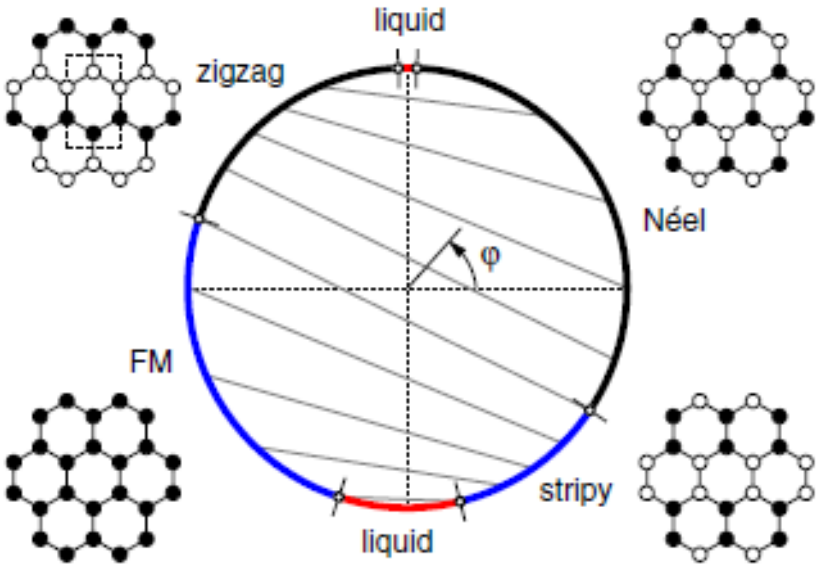

Figure 1.4: Phase diagram of the Kitaev-Heisenberg model obtained by the exact diagonalization for a 24-site cluster of the honeycomb structure. The result contains two spin liquid regions and four magnetically-ordered phases, whose ordering patterns are shown schematically in the figure (the black and white circles represent up and down spins, respectively). The gray lines inside the circle connect the points related by unitary transformations (see Ref. [50]). The figure is taken from Ref. [50].

the Kitaev-Heisenberg model. In this study, the Kitaev interaction is taken to be isotropic, $J_x = J_y = J_z = J_{\mathrm{Kitaev}}$, and the coupling constants are parametrized as

$$J_{\mathrm{Kitaev}} = -2A\sin\varphi, \tag{1.20}$$
$$J_{\mathrm{Heisenberg}} = -A\cos\varphi. \tag{1.21}$$

The result in Fig. 1.4 indicates that the Kitaev spin liquid remains stable around the pure Kitaev case with $J_{\mathrm{Heisenberg}} = 0$, for both the FM ($J_{\mathrm{Kitaev}} > 0$) and AFM ($J_{\mathrm{Kitaev}} < 0$) cases. The region is substantially wider for FM than AFM. When the Heisenberg interaction becomes larger, several different types of magnetic orderings appear, as shown in Fig. 1.4.

Effects of the J_Γ term in Eq. (1.19) were also studied for the full Hamiltonian in Eq. (1.17). The phase diagram obtained by the exact diagonalization for a 24-site cluster is shown in Fig. 1.5 [51]. In this study, the Kitaev and Heisenberg interactions are parametrized in a different way from Eqs. (1.20) and (1.21) as

$$J_{\mathrm{Kitaev}} = -\sin\phi, \tag{1.22}$$
$$J_{\mathrm{Heisenberg}} = -\cos\phi, \tag{1.23}$$

and the radial direction represents the strength of $J_\Gamma = J_\Gamma^x = J_\Gamma^y = J_\Gamma^z$: the circumference of the phase diagram corresponds to the Kitaev-Heisenberg model with

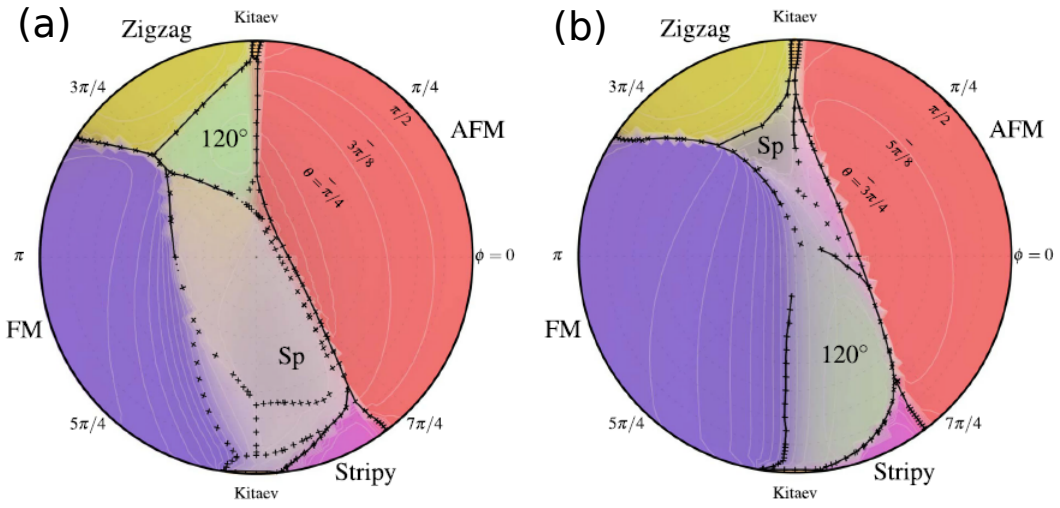

Figure 1.5: Phase diagram of the model in Eq. (1.19) for (a) $J_\Gamma < 0$ and (b) $J_\Gamma > 0$ obtained by the exact diagonalization for a 24-site cluster of the honeycomb structure. The result contains two spin liquid regions and several magnetically-ordered phases. The figures are taken and modified from Ref. [51].

$J_\Gamma = 0$, whereas the center of the phase diagram corresponds to the model with the J_Γ term only. The result indicates that the Kitaev spin liquid also remains stable against both the FM and AFM J_Γ, as shown in Figs. 1.5(a) and 1.5(b), respectively. For nonzero J_Γ, several magnetic orderings appear in addition to the ordered states in the Kitaev-Heisenberg case in Fig. 1.4.

1.3 Candidate materials for the Kitaev spin liquid

Along with the theoretical arguments in Sec. 1.2.3, a lot of efforts have been made for exploring candidate materials for the Kitaev model. The requisites are (i) Mott insulators with spin-orbital entangled Kramers doublet and (ii) quantum interference between different perturbation processes. To date, the possibility has been mostly pursued for materials with $4d$ and $5d$ electrons with the low-spin $(t_{2g})^5$ configurations, such as A_2IrO_3 (A=Na, Li) and $RuCl_3$. In this section, we briefly review the candidate materials and their properties.

1.3.1 Na_2IrO_3, α-Li_2IrO_3, and $H_3LiIr_2O_6$

Na_2IrO_3 and α-Li_2IrO_3 have been studied as Kitaev candidate materials since the early stage of the research. The prefix α for Li_2IrO_3 indicates the existence of polytypes as introduced in Sec. 1.3.3. The possibility of the dominant Kitaev interactions in these materials was already predicted in the theoretical paper by G. Jackeli and G. Khaliullin introduced in Sec. 1.2.3 [27].

These materials have quasi-2D lattice structures. Each layer is composed of

a honeycomb network of edge-sharing IrO_6 octahedra, as schematically shown in Fig. 1.3(c). Na and Li ions are located between the layers as well as the centers of hexagons in the honeycomb layer.

Mott insulating nature and the validity of $j_{\rm eff} = 1/2$ description in these materials have been confirmed through many experiments, such as the electronic conductivity [55, 56], photoemission spectroscopy [57], magnetic susceptibility [55, 56], and resonant inelastic X-ray scattering [58]. In addition, the predominant Kitaev-type bond-dependent interactions between $j_{\rm eff} = 1/2$ were confirmed by the X-ray scattering [59]. Also, the peculiar electronic and magnetic properties have been further supported by first-principles calculations [39–41, 43].

Despite the dominant Kitaev interactions, both two materials show magnetic ordering at low T. Na_2IrO_3 shows a zigzag order below $T_{\rm N} \simeq 15$ K (see Fig. 1.4) [56,60,61] , while α-Li_2IrO_3 shows a spiral magnetic order with an incommensurate wave number below $T_{\rm N} \simeq 15$ K [62]. Thus, the lowest-T states in these materials are not the Kitaev spin liquid. However, the estimated entropy per spin at just above $T_{\rm N}$ is about 15% and 20% of $k_{\rm B}$ln2 for Na_2IrO_3 and α-Li_2IrO_3, respectively [55, 56]. Such small entropy suggests strong frustration and possible proximity to the Kitaev spin liquid state.

Very recently, another iridium compound was synthesized in the form of $H_3LiIr_2O_6$ [63]. In this compound, the interlayer Li ions in α-Li_2IrO_3 are all replaced by H, which presumably enhances the two-dimensionality of the system. Notably, no magnetic order was found down to as low as 0.05 K [63]. Theoretically, the relevance of randomness has been discussed for explaining the absence of magnetic ordering [64–66].

1.3.2 α-$RuCl_3$

α-$RuCl_3$ is also a quasi-2D material, composed of honeycomb layers of edge-sharing $RuCl_6$ octahedra. In contrast to the iridates above, the honeycomb layers are weakly coupled by the van der Waals force. In this compound, the Mott insulating nature with the isospin $j_{\rm eff} = 1/2$ was also confirmed experimentally [67–69], and supported by first-principles calculations [67–69].

α-$RuCl_3$ shows a magnetic order at low T [70–73]. The order pattern is zigzag type, but the interlayer stacking pattern depends on samples [71–73]. The transition temperature $T_{\rm N}$ varies depending on the stacking of the honeycomb layers from ~ 7 K to ~ 14 K [70–73], and is reported as 6.5 K in a high quality sample almost free from stacking fault [74].

From the experimental point of view, there are several advantages in this compound, compared to the iridates. One is that the neutron scattering experiments can be performed easily compared to the iridates in which Ir ions are neutron absorbers. Another advantage is that the van der Waals material can be exfoliated to atomically thin films [75,76]. In addition, the magnetic order can be suppressed by applying an in-plane magnetic field [77–85]. Because of these advantages, a tremendous number of experiments have been performed for this compound. We will overview some of them in comparison with theoretical results in Sec. 1.4. We will also discuss the experimental results in comparison with our theoretical calculations in Chap. 6.

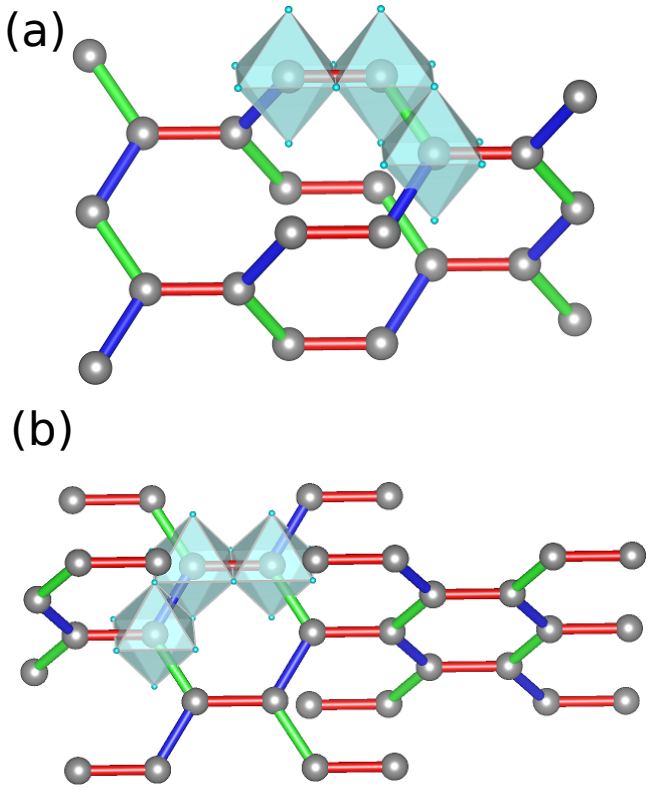

Figure 1.6: Schematic picture of (a) hyperhoneycomb and (b) stripy-honeycomb structures composed of edge-sharing octahedra.

1.3.3 β- and γ-Li_2IrO_3

As mentioned in the end of Sec. 1.2.2, the Kitaev model can be straightforwardly extended to other tricoordinate structures, even in three dimensions. Surprisingly, two different types of such three-dimensional (3D) tricoordinate structures are realized in β- and γ-Li_2IrO_3 [86, 87]. These are polytypes of α-Li_2IrO_3 introduced in Sec. 1.3.1. In these polytypes, the edge-sharing IrO_6 octahedra form the so-called hyperhoneycomb and stripy-honeycomb structures, as shown in Figs. 1.6(a) and 1.6(b), respectively. Both materials show complex incommensurate magnetic orders at low T at the transition temperature $T_N \simeq 38$ K for β-Li_2IrO_3 [86, 88] and $T_N \simeq 39.5$ K for γ-Li_2IrO_3 [89].

As will be introduced in Sec. 1.4.1, 3D Kitaev models may exhibit interesting finite-T phase transitions from high-T paramagnet to low-T QSL phases. In addition, many different types of topology appear in the excitation spectrum of matter fermions, such as the Fermi node, Fermi surfaces, nodal lines, and Weyl nodes [32, 33, 35]. Thus, the 3D candidate materials have attracted much attention from these theoretical interests.

1.4 Signatures of the Kitaev quantum spin liquid

Owing to the solvability of the Kitaev model, many theoretical predictions have been made for experimentally capturing the signatures of the Kitaev QSL. As discussed in the previous section, most of the candidate materials exhibit a magnetic long-range order at low T, and hence, the ground state is not the QSL. Nevertheless, the signatures of the QSL could be observed as the proximity effect to the QSL, if the Kitaev interaction is predominant over other exchange interactions that cause the parasitic long-range order. Such signatures would be observed, e.g., in the paramagnetic state above the Néel temperature and in the high-energy excitations even at low T. In this section, we introduce some of the examples in comparison with available experimental results.

1.4.1 Thermal fractionalization

Although the exact solution for the Kitaev model is limited to the ground state as introduced in Sec. 1.2.1, thermodynamic properties at finite T are obtained numerically. This has been done by using a quantum Monte Carlo (QMC) method based on the Majorana fermion representation, which will be reviewed in Chap. 3 [90, 91].

The representative results are shown in Fig. 1.7 for the isotropic case with $J_x = J_y = J_z = 4/3$ in Eq. (1.1). As shown in Fig. 1.7(a), the specific heat shows two peaks at $T \simeq 0.50$ and $T \simeq 0.016$. Both are crossovers, and we call the crossover temperatures $T_{\rm H}$ and $T_{\rm L}$. Associated with these two crossovers, while decreasing T, a half of the total entropy of $\ln 2$ per site is released at $T \sim T_{\rm H}$, and the rest half at $T \sim T_{\rm L}$, as shown in Fig. 1.7(b). This successive release of the entropy is the signature of fractionalization in the Kitaev QSL. Indeed, as shown in Fig. 1.7(b), the thermal average of W_p, $W = \langle W_p \rangle$, grows rapidly at $T \sim T_{\rm L}$, suggesting that the entropy release at $T_{\rm L}$ comes from the Z_2 fluxes. On the other hand, as shown in Fig. 1.7(c), the spin correlations grow rapidly at $T \sim T_{\rm H}$ and are almost saturated below $T_{\rm H}$. As the spin correlations correspond to the kinetic energy of matter fermions, their rapid growth is interpreted as the "Fermi degeneracy" of the matter fermions. This suggests that the high-T crossover at $T_{\rm H}$ is associated with the matter fermions. Thus, the two peaks in the specific heat and the successive release of the entropy are the signatures of the peculiar property of the QSL, the fractionalization of spins. This is called thermal fractionalization [91].

The signature of the thermal fractionalization was tested by the specific heat measurement for Na_2IrO_3 and α-Li_2IrO_3 [92], and α-$RuCl_3$ [70, 74]. For example, Fig. 1.8 shows the specific heat divided by T, $C_{\rm mag}/T$, and the entropy $S_{\rm mag}$ measured for α-$RuCl_3$ [70]. The broad maximum observed around 85 K is similar to the peak around $T_{\rm H}$ obtained in theoretical results for the Kitaev model as shown in Fig. 1.7(a). Furthermore, the entropy per site below the peak around $T_{\rm H}$ is roughly half of ln2 ($\simeq 2.88$ J/mol·K), which also well corresponds to the theoretical prediction. On the other hand, the broad peak in the low-T side in Fig. 1.7(a) is replaced by the sharp peak, reflecting the magnetic ordering at the transition temperature.

Another signature was discussed in the optical conductivity measurement for α-

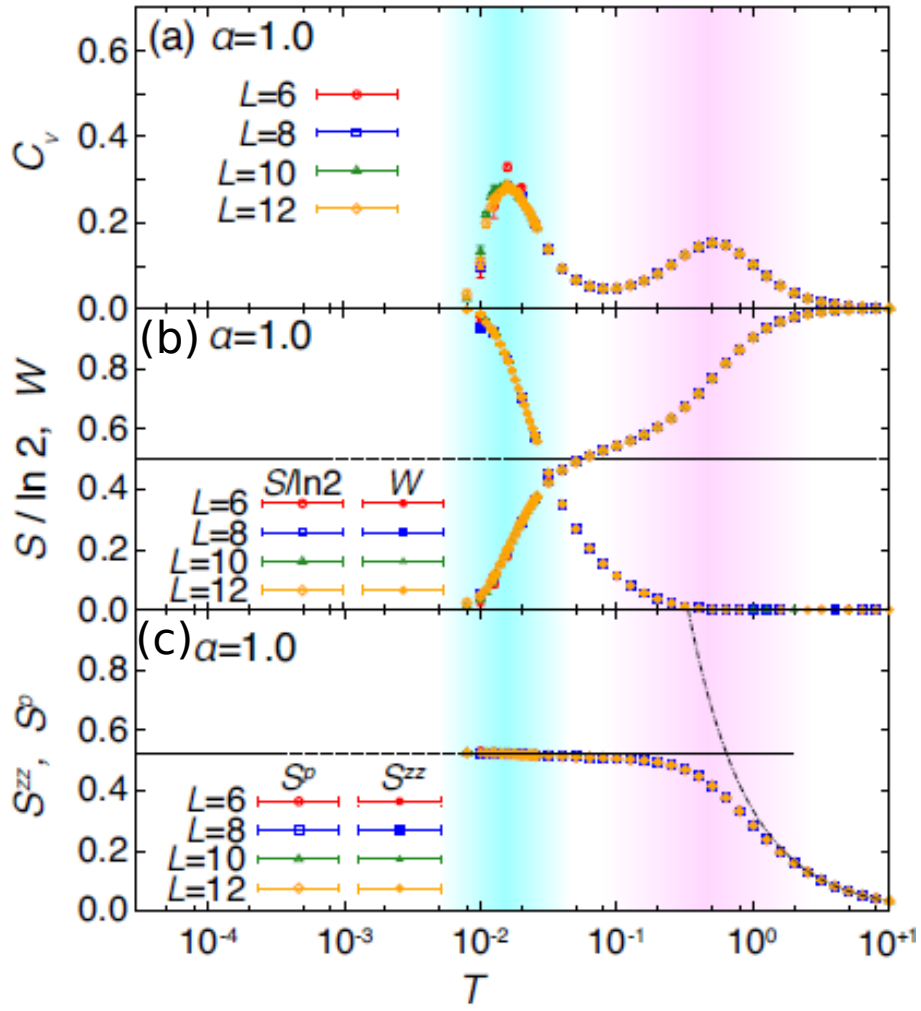

Figure 1.7: QMC results at finite T for the Kitaev model on the 2D honeycomb structure with the isotropic interactions with $J_x = J_y = J_z = 4/3$ in Eq. (1.1) for several different sizes of clusters $N = 2L^2$. T dependences of (a) the specific heat per site, C_v, (b) the entropy per site, S, and the thermal average of the flux $W = \langle W_p \rangle$, and (c) the equal-time spin correlations, S^{zz} and $S^p = (S^{xx} + S^{yy})/2$; $S^{\gamma\gamma}$ is defined as $S^{\gamma\gamma} = \langle S_j^\gamma S_{j'}^\gamma \rangle$ with j and j' are NN sites on a γ bond . The horizontal line in (b) denotes the half of $\ln 2$. In (c), the horizontal line represents the value at $T = 0$ which is calculated analytically [29], and the dashed-dotted curve represents the high-T Curie behavior $S_{zz} \sim J_z/4T$. The figures are taken from Ref. [91].

$RuCl_3$ [93]. As shown in Fig. 1.9(a), the optical conductivity exhibits several peaks. Among them, the low-energy peak around 1.2 eV denoted as α in the figure shows strong T dependence compared to other peaks. The integrated intensity of the peak α, $W_\alpha(T)$, is plotted as a function of T in Fig. 1.9(b). As the optical response originates from the kinetic energy of electrons, which corresponds to the magnetic exchange energy in Mott insulators [94], $W_\alpha(T)$ is ascribed to spin correlations [93].

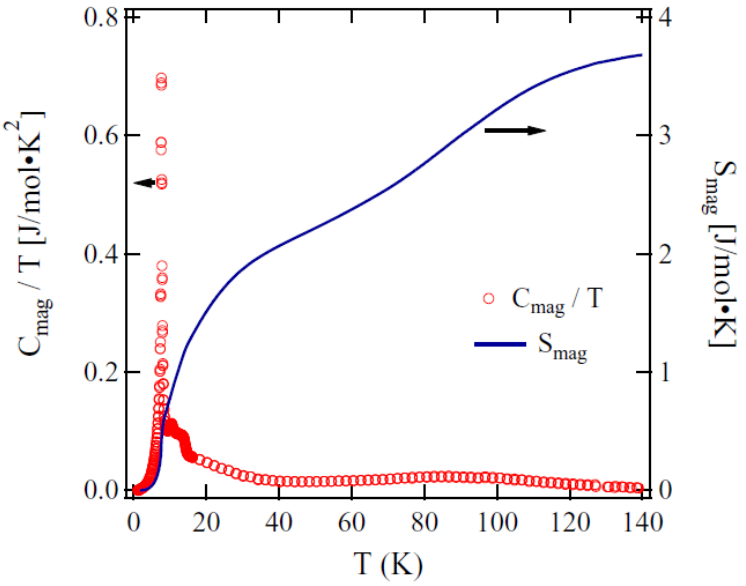

Figure 1.8: T dependence of the specific heat divided by T (open circles) and the entropy (solid curve) in α-$RuCl_3$. The figure is taken from Ref. [70].

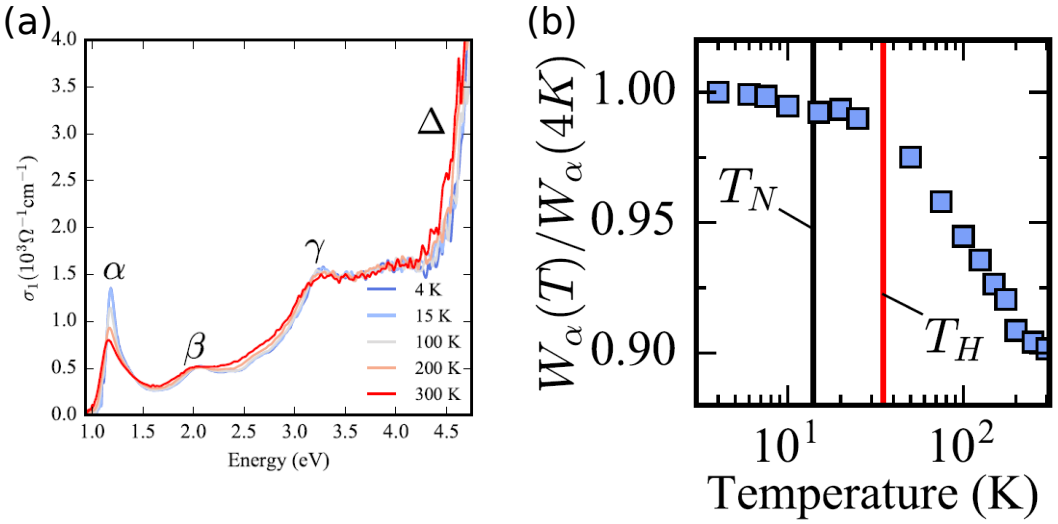

Figure 1.9: (a) Real part of the optical conductivity measured at several T obtained for α-$RuCl_3$. (b) T dependence of the spectral weight $W_\alpha(T)$ normalized by the value at 4 K. The magnetic ordering temperature T_N and the crossover scale T_H are indicated in the figure. The figures are taken and modified from Ref. [93].

As shown in Fig. 1.9(b), the T dependence of $W_\alpha(T)$ appears to be consistent with the theoretical result on the spin correlations for the Kitaev model in Fig. 1.7(c). From the comparison of the characteristic T for the saturation, the Kitaev interaction is estimated as 8 meV [93], which is in good agreement with the estimates in

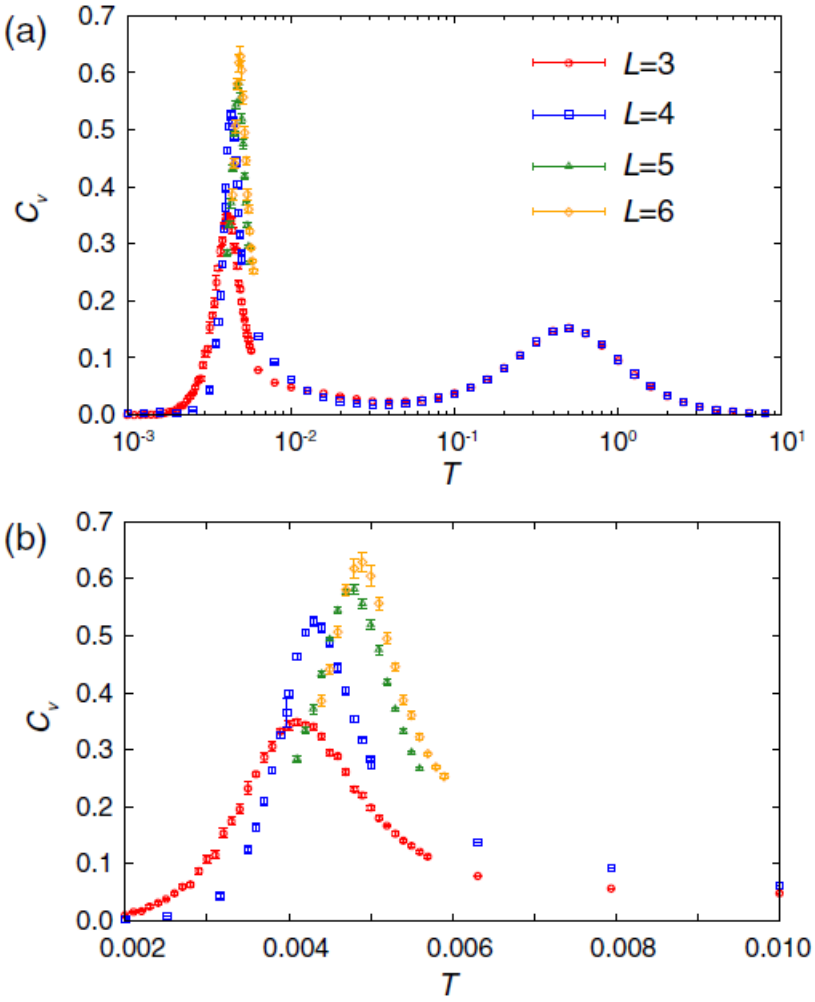

Figure 1.10: QMC results at finite T for the Kitaev model on the 3D hyperhoneycomb structure with the isotropic interactions with $J_x = J_y = J_z = 4/3$ in Eq. (1.1) for several different sizes of clusters $N = 4L^3$. (a) T dependence of the specific heat per site, and (b) the enlarged view in the vicinity of the low-T peak. The figures are taken and modified from Ref. [90].

other experiments [95–97].

Interestingly, the spatial dimension of the system matters to the thermodynamics. Figure 1.10 shows the T dependence of the specific heat obtained for the Kitaev model on the 3D hyperhoneycomb structure with the isotropic interactions $J_x = J_y = J_z = 4/3$. The specific heat has two peaks similar to the 2D case in Fig. 1.7(a), but the low-T peak shows substantial dependence on the system size: the peak height becomes higher and the width gets narrower while increasing the linear dimension of the system, L, as shown in Fig. 1.8(b). This behavior suggests that the 3D Kitaev model exhibits a finite-T phase transition, instead of the crossover in 2D. This phase transition separates the high-T paramagnetic state and

the low-T QSL connected to the exact solution at $T = 0$. The existence of the phase transition was further supported by the simulation for much larger sizes up to $L = 24$ for an effective model in the anisotropic limit [31]. The presence of the phase transition is ascribed to the constraint on the Z_2 fluxes W_p [31,90]. In the 3D case, W_p cannot be flipped independently because of the constraint for each closed volume imposed by the algebra for the Pauli matrices, and consequently, the flipped W_p always form closed loops. Thus, the phase transition can be interpreted as a confinement-deconfinement transition of the loops. In contrast, in the 2D case, W_p can be flipped independently, and such particlelike excitaions do not lead to a phase transition but just a crossover.

1.4.2 Dynamical spin structure factor in the ground state

As explained in Sec. 1.2.1, we can obtain the ground state and the excitations in the Kitaev model exactly. Nevertheless, it is not straightforward to calculate the spin dynamics in general. The difficulty comes from the time evolution of W_p including the flipping processes. For example, to calculate the dynamical spin structure factor $S(\mathbf{q}, \omega)$, which is measured by the inelastic neutron scattering and defined as

$$S(\mathbf{q}, \omega) = \sum_{\gamma} \sum_{j,j'} e^{i\mathbf{q}\cdot(r_j - r_{j'})} S^{\gamma}_{j,j'}(\omega), \tag{1.24}$$

where

$$S^{\gamma}_{j,j'}(\omega) = \int_0^{\infty} dt e^{i\omega t - \delta t} \langle S^{\gamma}_j(t) S^{\gamma}_{j'} \rangle, \tag{1.25}$$

we need to calculate dynamical spin correlations $\langle S^{\gamma}_j(t) S^{\gamma}_{j'} \rangle$ in Eq. (1.25), which include the flipping processes of W_p by the spin operators in the time evolution.

The difficulty was solved by mapping the problem to the X-ray edge problem and using the suitable expression for numerical evaluation developed in the field [98]. Similar to the case of static spin correlations, nonzero contributions to the dynamical spin structure factor come from $S^{\gamma}_j(\omega) S^{\gamma}_{j'}$ for j and j' on a same γ bond (including the onsite contributions), due to the conservation of W_p.

The representative results are shown in Fig. 1.11. The most characteristic feature is that the dynamical spin structure factor exhibits a broad continuum in a wide range of energy with less $\mathbf{q}$ dependence. This is distinct from the magnetic excitation spectrum in conventional magnets, where sharp dispersive modes show up from magnon excitations.

Another characteristic feature is the spin gap. In both isotropic and anisotropic cases, the dynamical spin structure factor shows a gap at low energy, while the gap for the continuum becomes larger for larger anisotropy. This originates from both the gap in the flux excitations discussed in Sec. 1.2.2 and the gap in the matter fermion spectrum in the anisotropic region, as the spin-flip excitation is a composite of the flux excitation and the matter fermion excitation. In addition, for sufficiently anisotropic cases, the spectrum has a δ-function contribution in addition to the

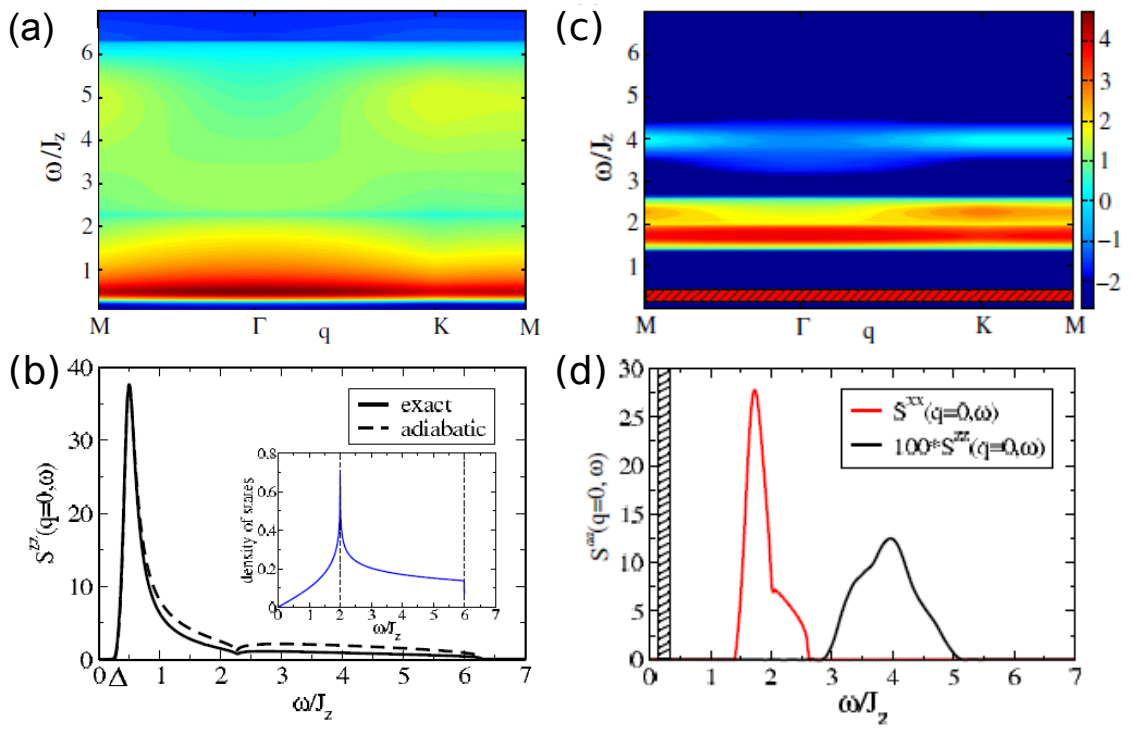

Figure 1.11: Exact results for the dynamical spin structure factor [Eq. (1.24)] of the Kitaev model on the 2D honeycomb structure for (a) the isotropic case with $J_x = J_y = J_z$ and (c) an anisotropic case with $J_x = J_y = 0.15J_z$. Corresponding data at the Γ point ($\mathbf{q} = 0$) are shown in (b) and (d), respectively. The inset in (b) represents the density of states for matter fermions. The hatched areas in (c) and (d) represents the δ-function contribution (see the text). The figures are taken and modified from Ref. [90].

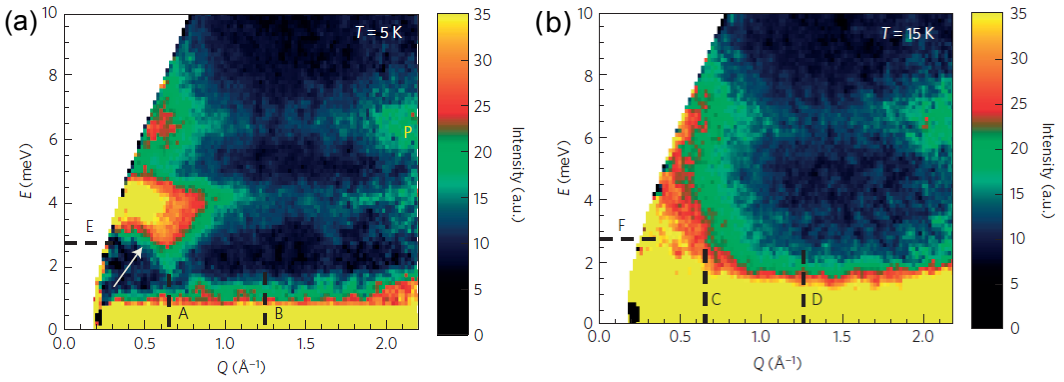

Figure 1.12: Inelastic neutron scattering data for α-$RuCl_3$ at (a) $T = 5$ K (below T_N) and (a) $T = 15$ K (above T_N). The figures are taken and modified from Ref. [96].

broad continuum. This originates from different parity between the ground state and the first excited state.

Inelastic neutron scattering experiments were performed for powder samples of α-$RuCl_3$ [96, 99]. Figure 1.12 displays the representative data [96]. As shown in the figures, the spectra show a broad continuum up to ~ 8 meV. In particular, the incoherent weight around 6.5 meV does not change below and above T_N, as shown in Figs. 1.12(a) and 1.12(b), respectively, and persists at least up to ~ 70 K [96]. The broad feature and the T dependence of the incoherent spectra are distinct from the typical behavior of spin waves in conventional magnets. Instead, the broad continuum up to the order of the Kitaev interaction is in agreement with the theoretical results shown in Fig. 1.11. Thus, these experimental results were reasonably interpreted as the proximity effect to the Kitaev spin liquid. Further analyses including experiments for single crystals will be discussed in comparison with our theoretical results in Chap. 6

1.4.3 Raman scattering

The Raman scattering experiment is another important probe for the spin dynamics. For the Kitaev model, the Raman scattering intensity was computed for both the ground state and at finite T as follows. By using the Loudon-Fleury formalism [100, 101], the Raman scattering intensity is calculated as [102]

$$I(\omega) = \int_{-\infty}^{\infty} dt e^{i\omega t} \langle \mathcal{R}(t)\mathcal{R}(0)\rangle, \tag{1.26}$$

where the Raman vertex operator $\mathcal{R}$ for the Kitaev model is given by

$$\mathcal{R} = \sum_{\gamma} \sum_{\langle j,j'\rangle_\gamma} (\epsilon_{in}\cdot \mathbf{d}^\gamma)(\epsilon_{out}\cdot \mathbf{d}^\gamma) J^\gamma S_j^\gamma S_{j'}^\gamma. \tag{1.27}$$

Here, ϵ_{in} and ϵ_{out} are the polarization directions of incoming and outgoing light, respectively, and $\mathbf{d}^\gamma$ denotes the direction of the γ bond. In the Kitaev model, since $\mathcal{R}$ commutes with the Z_2 fluxes, it is much easier to compute the Raman intensity $I(\omega)$, compared to the dynamical spin structure factor in the previous section. The calculations were first done exactly for the ground state [102], and later, numerically at finite T [97] by using the same QMC method used in Sec. 1.4.1.

Figure 1.13 shows the Raman intensity for the Kitaev model and the Kitaev-Heisenberg model on the honeycomb structure at $T = 0$ [102]. The result for the Kitaev model is calculated exactly, and that for the Kitaev-Heisenberg model are calculated by treating the Heisenberg coupling as a perturbation. The Raman intensity exhibits a broad continuum, which reflects the density of states of itinerant matter fermions. This is understood by considering the Majorana fermion representation of the Raman vertex operator $\mathcal{R}$ in Eq. (1.27), which is given as

$$\tilde{\mathcal{R}} = \sum_{\gamma} \sum_{\langle j,j'\rangle_\gamma} (\epsilon_{in}\cdot \mathbf{d}^\gamma)(\epsilon_{out}\cdot \mathbf{d}^\gamma) \frac{J^\gamma}{4} u_{j,j'}^\gamma c_j c_{j'}. \tag{1.28}$$

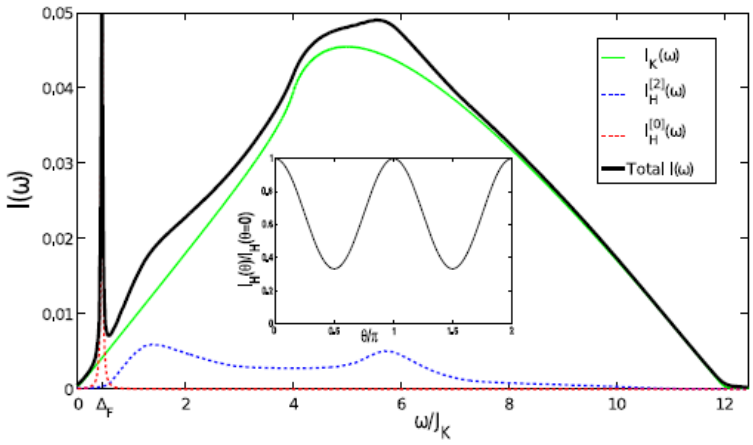

Figure 1.13: Raman scattering intensity calculated for the Kitaev model (green) and the Kitaev-Heisenberg model (black) on the honeycomb structure at $T = 0$. The calculation is performed for $J_x = J_y = J_z = 4J_{\mathrm{K}}$ in Eq. (1.1), and $J_{\mathrm{Heisenberg}} = J_\gamma/10$ in Eq. (1.18). The figure is taken from Ref. [102].

Because all $u^{\gamma}_{j,j'}$ and $\mathcal{R}$ commute with all W_p, the operation of $\mathcal{R}$ to a state excites matter fermions without changing fluxes. On including a weak Heisenberg interaction by which the system remains in the Kitaev spin liquid phase, the broad feature of the Raman intensity almost does not change. Similar broad continua were also predicted for the 3D hyperhoneycomb and stripy-honeycomb structures [103].

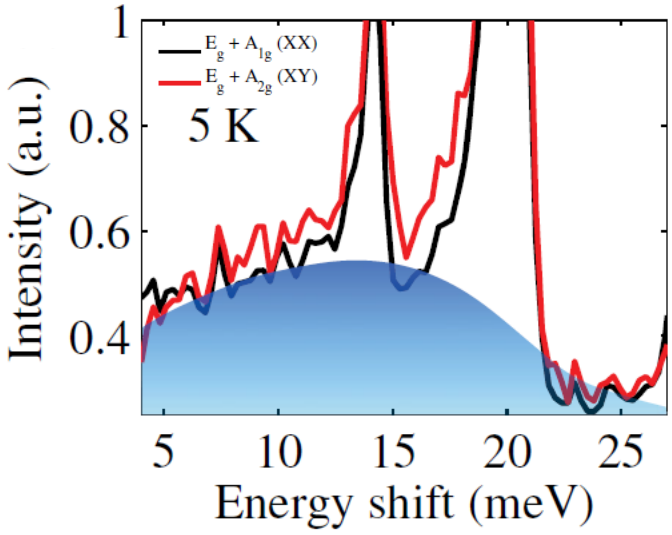

Figure 1.14: Raman scattering intensity for α-$RuCl_3$ at $T = 5$ K. The strong peak around 14 meV and 20 meV comes from phonon contributions. The shaded blue region is a guide to the eye for the continuum contribution. The figure is taken and modified from Ref. [95].

The Raman scattering experiment was performed for α-$RuCl_3$ [95]. The data at $T = 5$ K is shown in Fig. 1.14. The scattering intensity extends over a broad energy range. This is consistent with the theoretical prediction shown in Fig. 1.13, which suggests that the magnetic excitation of α-$RuCl_3$ is well described by the Kitaev model.

In the experiment, the T dependence of the incoherent intensity was also studied, as plotted in the inset of Fig. 1.15. The data do not follow conventional bosonic behavior expected for magnon and phonon excitations. This peculiar T dependence was explained by a theoretical calculation by using the Majorana QMC method [97]. The comparison between theory and experiment is shown in the main panel of Fig. 1.15; the experimental data are well fitted by the summation of the theoretical result for the Kitaev model and a bosonic background. As shown in the figure, the theoretical result is well described by $(1-f)^2$ (f is the Fermi distribution function), reflecting the fact that the continuum is dominated by pair creation or annihilation of matter fermions [97]. Thus, the good agreement between theory and experiment strongly suggests that α-$RuCl_3$ locates near the Kitaev QSL with fractionalized fermionic excitations, although it shows a long-range magnetic order at low T. In addition, the result also indicates that the effect of fractionalization can be observed in a wide T range of the order of the Kitaev interaction.

The Raman scattering experiments were also performed for 3D Kitaev candidate materials, β- and γ-Li_2IrO_3 [104]. Similar incoherent continua and fermionic T dependences are seen for these materials.

1.5 Purpose of this thesis

As discussed in the previous sections, the Kitaev model has brought about many significant breakthroughs in the study of quantum spin liquids. In particular, the exact solution enables us to treat the fractionalization of spins explicitly, which has been very difficult since the fractionalization is a direct consequence of quantum many-body effects. As discussed in Sec. 1.4, several consequences of the fractionalization were theoretically obtained for the temperature and energy dependences of the physical observables, and they have been tested for the candidate materials. The critical comparisons between theories and experiments have promoted the understanding of the quantum spin liquids.

On the other hand, it remains a challenge to compute the spin dynamics at finite T even for the exactly-soluble Kitaev model. This is because such calculations need to handle the dynamical spin correlations in the presence of thermally-excited Z_2 fluxes. Note that the calculation of the dynamical spin structure factor in Sec. 1.4.2 was limited to the ground state because of this difficulty. Nonetheless, such finite-T dynamical properties are crucial for identifying the proximity to the Kitaev quantum spin liquid in the candidate materials, as they are also expected to reflect the fractionalization. We also note that such calculations are necessary to compute the magnetic susceptibility, which is a fundamental quantity for magnets. It is highly desired to invent new theoretical methods and to compute the finite-T spin dynamics

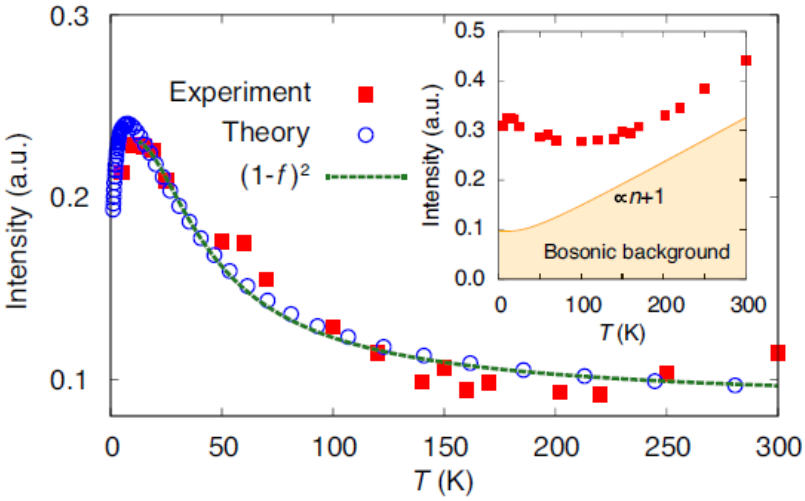

Figure 1.15: Comparison between the numerical results and the experimental data for α-$RuCl_3$. Main panel: blue circles represent QMC data for a L = 20 cluster for the integrated Raman intensity in the middle energy range $I_{\rm mid}$. Red squares are the experimental data in the energy window from 5 meV to 12.5 meV, from which the nonmagnetic background is subtracted. Green dashed lines represent the fitting by $a_M[1-f]^2 + b_M$. In calculating $I_{\rm mid}$, J is taken as $J = 10$ meV and integral energy range are set to corresponds to the one used for experimental data. Inset: red squares show the experimental raw data and the orange curve indicates the bosonic background. The figure is taken from Ref. [97].

for further understanding of the physics of quantum spin liquids.

The aim of this thesis is to solve this difficulty and clarify the spin dynamics at finite T of the Kitaev model. For this purpose, we develop new numerical techniques to calculate the dynamical spin correlations. The most important technique is the continuous-time quantum Monte Carlo method (CTQMC) on the basis of the Majorana fermion representation. This allows us to compute the dynamical spin correlations for any flux configuration at any T. Another new technique is the cluster dynamical mean-field theory (CDMFT) also based on the Majorana fermion representation. This provides a concise alternative of the QMC method described in Sec. 1.4.1, and furthermore, it might be applicable to the extended Kitaev models with additional interactions described in Sec. 1.2.4, for which available numerical techniques are limited. We combine the two methods (CDMFT+CTQMC) to calculate the spin dynamics of the Kitaev model in a wide T range down to just above $T_{\rm L}$ where the mean-field nature of the CDMFT leads to an artificial phase transition. To access all T regions including much lower T than $T_{\rm L}$, we also combine the CTQMC method with the QMC method (QMC+CTQMC). By using these techniques, we compute the physical observables reflecting the spin dynamics, such as the magnetic susceptibility, the dynamical spin structure factor, and the NMR relaxation rate $1/T_1$. We find that the T dependences of all these quantities show

distinct features from those for conventional magnets, which can be a smoking gun of the fractionalized excitations in the Kitaev quantum spin liquid. We compare the results with experimental data to identify such signatures.

1.6 Organization of this thesis

The organization of this thesis is as follows. In Chap. 2, we introduce a Majorana fermion representation of the Kitaev model used in this thesis. In Chap. 3, we describe the method that we use in this thesis: QMC, CDMFT, CTQMC and the maximum entropy method (MEM). In Chaps. 4 and 5, we present the numerical results of $S(\mathbf{q}, \omega)$, $1/T_1$, and χ for the Kitaev model. We show that these dynamical quantities exhibit distinct behavior from conventional magnets. In Chap. 4, the results obtained by CDMFT+CTQMC are presented for the 2D honeycomb case. In Chap. 5, we present the results obtained by QMC+CTQMC for both 2D honeycomb and 3D hyperhoneycomb structures. In Chap. 6, we discuss our theoretical results in comparison with other theoretical results for the Kitaev model and experimental results for the Kitaev candidate materials. Chapter 7 is devoted to summary and perspectives.

2
Model

In this chapter, we introduce a Majorana fermion representation of the Kitaev model, which is suitable for the numerical simulations at finite T. The Hamiltonian of the Kitaev model is given by

$$\mathcal{H} = -J_x \sum_{\langle j,j' \rangle_x} S_j^x S_{j'}^x - J_y \sum_{\langle j,j' \rangle_y} S_j^y S_{j'}^y - J_z \sum_{\langle j,j' \rangle_z} S_j^z S_{j'}^z, \tag{2.1}$$

as already introduced in Eq. (1.1). In Sec. 1.2.1, we discussed the exact solution of the ground state by introducing a Majorana fermion representation with four Majorana operators per spin. In this chapter, we introduce another Majorana fermion representation, which uses two Majorana operators for representing each spin. This is suitable for numerics as it does not extend the Hilbert space and as the projection to the original Hilbert space is not needed. In Sec. 2.1, we rewrite the Hamiltonian in Eq. (2.1) by replacing the spin operators by fermion operators via the Jordan-Wigner transformation. Then, in Sec. 2.2, we further rewrite the Hamiltonian by introducing the Majorana fermion operators.

2.1 Jordan-Wigner transformation

The spin operators at the same site satisfy the anticommutation relations:

$$\{S_j^+, S_j^-\} = 1, \quad \{S_j^+, S_j^+\} = 0, \quad \{S_j^-, S_j^-\} = 0, \tag{2.2}$$

where $S_j^+ = S_j^x + iS_j^y$ and $S_j^- = S_j^x - iS_j^y$. The relations are similar to those for fermion operators, which infers the possibility of representing the spin operators by fermion operators. On the other hand, the spin operators at different sites satisfy the commutation relations,

$$[S_j^+, S_{j'}^-] = 0, \quad [S_j^+, S_{j'}^+] = 0, \quad [S_j^-, S_{j'}^-] = 0, \tag{2.3}$$

instead of the anticommutation relations. Hence, for representing the spin operators by fermion operators, we need to modify the commutation relations to the anticommutation ones. This is achieved by considering new operators $a_j^\dagger$ and a_j defined as

$$a_j^\dagger = \prod_{j'=0}^{j-1} (-2S_{j'}^z) S_j^+, \quad a_j = \prod_{j'=0}^{j-1} (-2S_{j'}^z) S_j^-. \tag{2.4}$$

Then, the operators satisfy the fermionic anticommutation relations for arbitrary j and j' as

$$\{a_j^\dagger, a_{j'}\} = \delta_{j,j'}, \quad \{a_j^\dagger, a_{j'}^\dagger\} = 0, \quad \{a_j, a_{j'}\} = 0. \tag{2.5}$$

By using these new operators, the spin operators are represented as

$$S_j^+ = \prod_{j'=0}^{j-1}(-2S_{j'}^z)a_j^\dagger, \tag{2.6}$$

$$S_j^- = \prod_{j'=0}^{j-1}(-2S_{j'}^z)a_j, \tag{2.7}$$

$$S_j^z = a_j^\dagger a_j - \frac{1}{2} = n_j - \frac{1}{2}, \tag{2.8}$$

where n_j is the number operator defined by $n_j = a_j^\dagger a_j$. This is called the Jordan-Wigner transformation.

In order to apply the Jordan-Wigner transformation to the Kitaev model in Eq. (2.1), we regard the whole lattice as a one-dimensional chain composed of the x and y bonds (see Fig. 2.1). Then, interaction terms in the Hamiltonian are transformed as

$$S_j^x S_{j+1}^x = \frac{1}{4}(a_j^\dagger - a_j)(a_{j+1}^\dagger + a_{j+1}), \tag{2.9}$$

$$S_j^y S_{j+1}^y = \frac{1}{4}(a_j^\dagger + a_j)(-a_{j+1}^\dagger + a_{j+1}), \tag{2.10}$$

$$S_j^z S_{j'}^z = \left(n_j - \frac{1}{2}\right)\left(n_{j'} - \frac{1}{2}\right), \tag{2.11}$$

where j runs along the xy chains, and j, j' in Eq. (2.11) are the NN sites on a z bond connecting the xy chains.

Note that, in the Jordan-Wigner transformation, an additional nonlocal contribution arises from the boundary when the chain form a closed loop. For instance, when the sites 0 and $j(\neq 1)$ at the both ends are connected by the x bond, the additional contribution is written in the form of

$$S_0^x S_j^x = \frac{1}{4}(a_0^\dagger - a_0)\prod_{j'=1}^{j-1}(-2n_{j'} + 1)(a_j^\dagger + a_j). \tag{2.12}$$

In the QMC calculation in previous studies [90, 91], whose results are used in this thesis, the lattices are broken up into one-dimensional chain(s) with open boundary condition(s) so as to avoid the boundary contributions. In the CDMFT calculations in Chap. 4, we will consider periodic boundary conditions and neglect such a nonlocal term in Eq. (2.12), assuming that the lattice is sufficiently large and the boundary contributions do not affect the results.

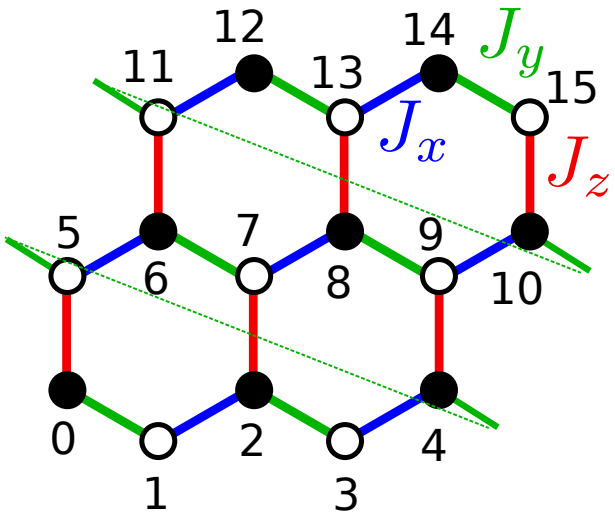

Figure 2.1: Example of site assignment to form a one-dimensional chain in the Jordan-Wigner transformation. The dotted lines connect the sites at the boundaries.

2.2 Majorana fermion representation

We further rewrite the fermion representation by using Majorana fermion operators defined by

$$c_w = (a_w - a_w^\dagger)/i, \quad \bar{c}_w = (a_w + a_w^\dagger), \tag{2.13}$$

$$c_b = (a_b + a_b^\dagger), \quad \bar{c}_b = (a_b - a_b^\dagger)/i, \tag{2.14}$$

where $b(w)$ represents a site index for even(odd) number sites (see Figs. 1.1 and 2.1). By using these operators, the Hamiltonian is written in the form

$$\mathcal{H}_{\rm Kitaev} = i\frac{J_x}{4}\sum_{(j,j')_x} c_j c_{j'} - i\frac{J_y}{4}\sum_{(j,j')_y} c_j c_{j'} - i\frac{J_z}{4}\sum_{(j,j')_z} \eta_r c_j c_{j'}, \tag{2.15}$$

where the sum over $(j,j')_\gamma$ is taken for the NN sites on a γ bond with $j < j'$; $\eta_r = i\bar{c}_j\bar{c}_{j'}$ is defined on each z bond connecting $j \in b$ and $j' \in w$ sites. Since η_r commutes with the Hamiltonian as well as other $\eta_{r'}$ and since $\eta_r^2 = 1$, $\{\eta_r\}$ are conserved quantities whose eigenvalues take ± 1. Thus, the model in Eq. (2.15) describes the itinerant Majorana fermions $\{c_j\}$ coupled to the Z_2 variables $\eta_r = \pm 1$. Note that $\{\eta_r\}$ are related with the conserved quantities $\{W_p\}$ in Eq. (1.2) as $W_p = \prod_r \eta_r$, where r are the z bonds included in the plaquette p.

We note that the transformation from Eq. (2.1) to Eq. (2.15) is performed by introducing the Majorana operators that do not extend the original Hilbert space. This is in contrast to the Majorana fermion representation used in Sec. 1.2.1. Hence, in the present formalism via the Jordan-Wigner transformation, we do not need a projection for calculating physical quantities.

For a given $\{\eta_r\}$ configuration, the Hamiltonian in Eq. (2.15) is written in the matrix form

$$\mathcal{H}_{\rm Kitaev}(\{\eta_r\}) = H^{\{\eta_r\}}_{j,j'} c_j c_{j'}, \tag{2.16}$$

with a pure-imaginary Hermitian matrix $H^{\{\eta_r\}}$. For a nonzero eigenvalue and the corresponding eigenvector of $H^{\{\eta_r\}}$, from the eigenvalue equation $H^{\{\eta_r\}}\mathbf{t}_\lambda = \epsilon_\lambda \mathbf{t}_\lambda$, we obtain $H^{\{\eta_r\}}\mathbf{t}^*_\lambda = -\epsilon_\lambda \mathbf{t}^*_\lambda$ by taking the complex conjugate. This means that $\mathbf{t}^*_\lambda$ is another eigenvector of $H^{\{\eta_r\}}$ with eigenvalue $-\epsilon_\lambda$. Thus, nonzero eigenvalues appear in pair as $\pm\epsilon_\lambda$. On the other hand, when the eigenvalue is zero, namely $H^{\{\eta_r\}}\tilde{\mathbf{t}}_{\lambda'} = 0$, we can take the corresponding eigenvector as real, since $H^{\{\eta_r\}}$ is pure imaginary. Then, we can set the eigenvectors $\mathbf{t}_{\lambda'} = \frac{1}{\sqrt{2}}(\tilde{\mathbf{t}}_{\lambda'} + i\tilde{\mathbf{t}}_{\lambda''})$ by using two real eigenvectors for the zero energy, $\tilde{\mathbf{t}}_{\lambda'}$ and $\tilde{\mathbf{t}}_{\lambda''}$, so that $\mathbf{t}_{\lambda'}$ and $\mathbf{t}^*_{\lambda'}$ are orthogonal. Thus, we can diagonalize $H^{\{\eta_r\}}$ by a unitary matrix U as

$$U^\dagger H^{\{\eta_r\}} U = \mathrm{diag}(\epsilon_0, -\epsilon_0, \epsilon_1, -\epsilon_1, ...), \tag{2.17}$$

where U has the form of $U = [\mathbf{t}_0, \mathbf{t}^*_0, \mathbf{t}_1, \mathbf{t}^*_1, ...]$. Note that in Eq. (2.17) some of ϵ_λ can be zero. On the other hand, when we define the operators $\tilde{f}$ as

$$\tilde{f}_j = 2\sum_j (U^\dagger)_{j,k} c_k, \tag{2.18}$$

they satisfy the relations:

$$\tilde{f}_{2j+1} = \tilde{f}^\dagger_{2j}, \tag{2.19}$$

$$\{\tilde{f}_{2j}, \tilde{f}_{2j'+1}\} = \delta_{j,j'}, \quad \{\tilde{f}_{2j}, \tilde{f}_{2j'}\} = 0, \quad \{\tilde{f}_{2j+1}, \tilde{f}_{2j'+1}\} = 0. \tag{2.20}$$

As $\tilde{f}_{2j}$ and $\tilde{f}_{2j'+1}$ satisfy the fermionic anticommutation relations, we can regard them as the fermion operators:

$$f_\lambda = \tilde{f}_{2\lambda}, \quad f^\dagger_\lambda = \tilde{f}_{2\lambda+1}. \tag{2.21}$$

By substituting these relations to Eq. (2.16), we finally obtain the diagonal form of the Hamiltonian for a given $\{\eta_r\}$ as

$$\begin{aligned}\mathcal{H}_{\rm Kitaev}(\{\eta_r\}) &= \sum_\lambda \epsilon_\lambda (\tilde{f}_{2\lambda+1}\tilde{f}_{2\lambda} - \tilde{f}_{2\lambda}\tilde{f}_{2\lambda+1}) \\ &= \sum_\lambda \epsilon_\lambda \left(f^\dagger_\lambda f_\lambda - \frac{1}{2} \right).\end{aligned} \tag{2.22}$$

Thus, the Hamiltonian is diagonalized in the subspace for a given $\{\eta_r\}$. It is straightforward to calculate physical quantities, such as the internal energy and spin correlations, by using U and $\{\epsilon_\lambda\}$, as will be illustrated in Chap. 3.

3
Method

In this chapter, we describe the details of the methods used in this thesis, the Majorana QMC, CDMFT and CTQMC methods. The latter two, CDMFT and CTQMC, were newly developed by the author and coworkers. By using the Majorana fermion representation of the Kitaev model introduced in Sec. 2.2, we describe the framework of the Majorana QMC in Sec. 3.1 and the Majorana CDMFT in Sec. 3.2. In the Majorana CDMFT, the impurity problem is solved exactly by enumerating all the configurations of the Z_2 variables $\{\eta_r\}$. In the two methods, all $\{\eta_r\}$ are treated as classical variables. Hence, these enable us to compute the quantities which preserve $\{\eta_r\}$ in the imaginary-time evolution. In Sec. 3.3, we introduce the CTQMC method which is applied to Monte Carlo samples of $\{\eta_r\}$ obtained by the Majorana QMC method or to all $\{\eta_r\}$ configurations which appear in impurity problem in the Majorana CDMFT method. In the CTQMC method, the imaginary-time evolution of η_r is treated by a Monte Carlo technique developed for interacting fermion systems. Hence, by the combined methods, CDMFT+CTQMC or QMC+CTQMC, we can compute dynamical spin correlations as functions of the imaginary time. In Sec. 3.4, we also introduce the maximum entropy method (MEM) used for obtaining the dynamical spin correlations as functions of the real frequency. In Sec. 3.5, we present the definitions of the physical quantities that we measure by the numerical methods in the following chapters.

3.1 Quantum Monte Carlo method

As explained in Secs. 2.2, the Kitaev model in Eq. (1.1) is mapped to a model with free Majorana fermions coupled to Z_2 variables $\{\eta_r\}$ as shown in Eq. (2.15). In the ground state, particular configurations of $\{\eta_r\}$ which minimize the energy are selected (there are many configurations of $\{\eta_r\}$ because of the gauge redundancy depending on the boundary conditions). On the other hand, to obtain thermodynamical properties of the model at finite T, we need to consider thermal fluctuations of the Z_2 variables. This has been achieved by using Monte Carlo sampling of the configurations of $\{\eta_r\}$ [90, 91]. Since a part of the calculations in this thesis relies on the results obtained by the QMC method, we briefly review the framework.

The partition function of the model is given by

$$Z = \mathrm{Tr} e^{-\beta \mathcal{H}} = \sum_{\{\eta_r\}} \mathrm{Tr}_c e^{-\beta \mathcal{H}^{\{\eta_r\}}} = \sum_{\{\eta_r\}} Z^{\{\eta_r\}}, \tag{3.1}$$

where

$$Z^{\{\eta_r\}} = \mathrm{Tr}_c e^{-\beta \mathcal{H}^{\{\eta_r\}}}. \tag{3.2}$$

Here, Tr_c represents the trace for the c operators in a sector specified by $\{\eta_r\}$. By using the expression of the Hamiltonian in Eq. (2.22), $Z^{\{\eta_r\}}$ is given as

$$Z^{\{\eta_r\}} = \sum_{\lambda} e^{-\beta\epsilon_\lambda^{\{\eta_r\}}}. \tag{3.3}$$

The thermal average of an operator A is computed by

$$\langle A\rangle = \frac{1}{Z}\mathrm{Tr}[Ae^{-\beta\mathcal{H}}] \tag{3.4}$$

$$= \frac{1}{Z}\sum_{\{\eta_r\}} \mathrm{Tr}_c[A^{\{\eta_r\}}e^{-\beta\mathcal{H}^{\{\eta_r\}}}] \tag{3.5}$$

$$= \frac{1}{Z}\sum_{\{\eta_r\}} \langle A\rangle^{\{\eta_r\}} Z^{\{\eta_r\}}, \tag{3.6}$$

where $A^{\{\eta_r\}} = \mathcal{P}^{\{\eta_r\}}A\mathcal{P}^{\{\eta_r\}}$ [$\mathcal{P}^{\{\eta_r\}}$ is the projection operator to a sector specified by $\{\eta_r\}$, and $\langle A\rangle^{\{\eta_r\}} = \mathrm{Tr}_c[A^{\{\eta_r\}}e^{-\beta\mathcal{H}^{\{\eta_r\}}}]/Z^{\{\eta_r\}}$ is the average of the operator A in the sector of $\{\eta_r\}$. If $A^{\{\eta_r\}}$ is given in the form of $A^{\{\eta_r\}} = \sum_{j,j'} A_{j,j'}^{\{\eta_r\}} c_j c_{j'}$, it can be rewritten by using Eq. (2.18) as

$$\sum_{j,j'} A_{j,j'}^{\{\eta_r\}} c_j c_{j'} = \sum_{j,j'} \tilde{A}_{j,j'}^{\{\eta_r\}} \tilde{f}_j \tilde{f}_{j'}, \tag{3.7}$$

where

$$\tilde{A}_{j,j'}^{\{\eta_r\}} = \frac{1}{4}\sum_{k,k'} U_{j,k}^{\dagger} A_{k,k'}^{\{\eta_r\}} U_{k',j'}. \tag{3.8}$$

Then $\mathrm{Tr}_c[A^{\{\eta_r\}}e^{-\beta\mathcal{H}^{\{\eta_r\}}}]$ is given as

$$\mathrm{Tr}_c[A^{\{\eta_r\}}e^{-\beta\mathcal{H}^{\{\eta_r\}}}] = \sum_{\lambda} \frac{\tilde{A}_{2\lambda,2\lambda}^{\{\eta_r\}} + e^{-\beta\epsilon_\lambda^{\{\eta r\}}}\tilde{A}_{2\lambda+1,2\lambda+1}^{\{\eta_r\}}}{1+e^{-\beta\epsilon_\lambda^{\{\eta_r\}}}}. \tag{3.9}$$

Thus, to calculate $\langle A\rangle$, we first solve the free Majorana fermion problem with the Hamiltonian $\mathcal{H}^{\{\eta_r\}}$ to obtain $Z^{\{\eta_r\}}$ and $\langle A\rangle^{\{\eta_r\}}$, and then calculate the average of $\langle A\rangle^{\{\eta_r\}}$ with respect to $\{\eta_r\}$ with the weight given by $Z^{\{\eta_r\}}$.

The number of configurations of $\{\eta_r\}$ grows exponentially with respect to the system size. In the QMC method, the summations in Eqs. (3.1) and (3.6) are computed by the Monte Carlo sampling technique, as

$$Z_{\mathrm{MC}} = \frac{2^{N/2}}{N_{\mathrm{MC}}} \sum_{\{\eta_r\}\in\text{MC samples}} Z^{\{\eta_r\}} \tag{3.10}$$

and

$$\langle A\rangle_{\mathrm{MC}} = \frac{\sum_{\{\eta_r\}\in\text{MC samples}} A^{\{\eta_r\}}Z^{\{\eta_r\}}}{\sum_{\{\eta_r\}\in\text{MC samples}} Z^{\{\eta_r\}}}, \tag{3.11}$$

respectively. Here, $Z^{\{\eta_r\}}$ is the Monte Carlo weight of a state specified by $\{\eta_r\}$; N is the system size (the number of sites), and N_{MC} is the number of Monte Carlo samples generated with the weight $Z^{\{\eta_r\}}$. This Majorana QMC method is free from minus sign problem as $Z^{\{\eta_r\}}$ is positive definite.

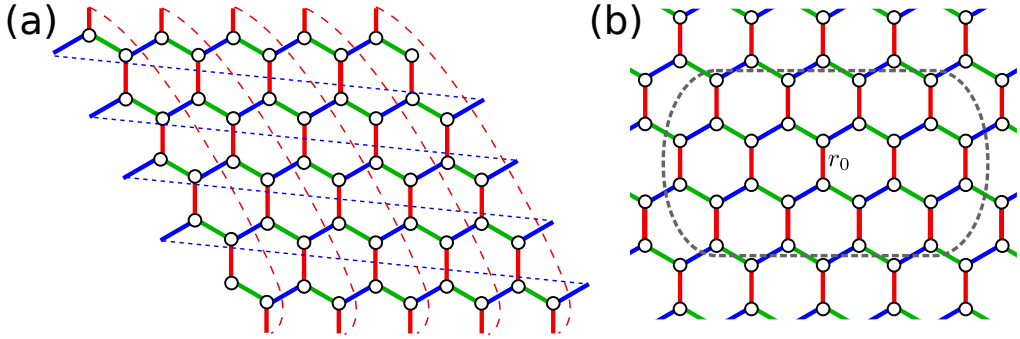

Figure 3.1: (a) Schematic picture of the honeycomb structure with shifted periodic boundary condition used in the QMC+CTQMC calculations. $L = 5$ (50 sites) in this example. Note that the interaction on x bond connected to the lower-left and the upper-right sites are omitted to avoid the nonlocal term in Eq. 2.12. (b) Schematic picture of the 26-site cluster mainly used in the CDMFT calculations (dashed oval). r_0 represents the z bond on which dynamical spin correlations are calculated in the CDMFT+CTQMC calculations.

3.2 Cluster dynamical mean-field theory

In this section, we introduce another way to handle the summation over $\{\eta_r\}$ in Eqs. (3.1) and (3.6). As the Majorana Hamiltonian in Eq. (2.15) is formally similar to the Falicov-Kimball model or the double-exchange model with Ising localized moments, we can apply the DMFT framework for the double-exchange model to the Kitaev model [105]. As shown in the previous study by the real-space QMC simulation [91] and introduced in Sec. 1.4.1, spatial correlations between η_r (or W_p) develop at low T. To take into account such spatial correlations, we adopt a cluster extension of DMFT, called the cluster dynamical mean-field theory (CDMFT) [106].

In the CDMFT, the summation with respect to $\{\eta_r\}$ is taken only within a cluster of the lattice sites, and the configurations of $\{\eta_r\}$ outside the cluster are taken into account at the mean-field level, as described in details below. In other words, the CDMFT method replaces the lattice problem by an impurity problem for the cluster with a small number of sites. This reduces the computational cost. Moreover, this method can possibly be applied to extended Kitaev models with other interaction terms and a magnetic field, which are difficult to handle by the QMC method in the previous section because they violate the conservation of $\{\eta_r\}$.

In the CDMFT, we regard the whole lattice as a periodic array of clusters. The Hamiltonian in Eq. (2.15) is rewritten into the matrix form of

$$\mathcal{H} = \sum_{\zeta,\zeta',j,j'} \frac{1}{2} \mathcal{H}^0_{\zeta,j;\zeta',j'} c_{\zeta,j} c_{\zeta',j'} + \sum_{\zeta,j,j'} \frac{1}{2} \mathcal{H}^{\{\eta_r\}}_{j,j'} c_{\zeta,j} c_{\zeta,j'}, \tag{3.12}$$

where ζ and ζ' are the indices for the clusters, and j and j' denote the sites in each N_c-site cluster. The coefficient $1/2$ in Eq. (3.12) is introduced to follow the notation

in Ref. [107]. In Eq. (3.12), the first term corresponds to the first and second terms in Eq. (2.15), while the second term is for the third term. We here take the shape of the cluster so that both two sites on a z bond belong to the same cluster, as exemplified in Fig. 3.1(b). Then, the two-body interactions in the second terms in Eq. (3.12) do not bestride between different clusters. Green's function for Eq. (3.12) is formally written as

$$G(\mathbf{k}, i\omega_n) = (i\omega_n - 2\mathcal{H}^0(\mathbf{k}) - \Sigma(\mathbf{k}, i\omega_n))^{-1}, \tag{3.13}$$

where $\omega_n = (2n+1)\pi T$ is the Matsubara frequency (n is an integer, and the Boltzmann constant $k_{\rm B}$ and the reduced Planck constant $\hbar$ are set to unity), $\Sigma(\mathbf{k}, i\omega_n)$ is the self-energy, and $\mathcal{H}^0(\mathbf{k})$ is the Fourier transform of $\mathcal{H}^0_{\zeta,j;\zeta',j'}$ in Eq. (3.12) given by the matrix:

$$\mathcal{H}^0_{j,j'}(\mathbf{k}) = \sum_{\zeta} \mathcal{H}^0_{\zeta,j;0,j'} e^{-i\mathbf{k}\cdot\mathbf{r}_\zeta}, \tag{3.14}$$

where $\mathbf{r}_\zeta$ is the coordinate of the cluster ζ. Note that the wave number $\mathbf{k}$ is defined for the superlattice composed of a periodic array of the clusters.

Following the spirit of the DMFT [108, 109], we omit the $\mathbf{k}$ dependence of the self-energy: $\Sigma(\mathbf{k}, i\omega_n) = \Sigma(i\omega_n)$. In this approximation, local Green's function is defined within a cluster as

$$G_{j,j'}(i\omega_n) = \frac{1}{N'} \sum_{\mathbf{k}} \left[(i\omega_n - 2\mathcal{H}^0(\mathbf{k}) - \Sigma(i\omega_n))^{-1} \right]_{j,j'}, \tag{3.15}$$

where N' is the number of clusters in the whole lattice ($N = N_c N'$), and j and j' denotes the sites in the cluster. The Weiss function is introduced to take into account the correlation effects in other clusters as

$$\mathcal{G}^0_{j,j'}(i\omega_n)^{-1} = G_{j,j'}(i\omega_n)^{-1} + \Sigma_{j,j'}(i\omega_n). \tag{3.16}$$

In order to take into account the interaction $\mathcal{H}^{\{\eta_r\}}$ in Eq. (3.12) within the cluster that we focus on, we consider the impurity problem for the cluster described by the effective action in the path-integral representation for Majorana fermions [107]. The partition function is given by

$$Z = \sum_{\{\eta_r\}} Z^{\{\eta_r\}}, \tag{3.17}$$

where

$$Z^{\{\eta_r\}} = \int \mathcal{D}\chi \exp(-\mathcal{S}^{\{\eta_r\}}_{\rm eff}). \tag{3.18}$$

Here, the sum of $\{\eta_r\}$ in Eq. (3.17) runs over all possible configurations of $\{\eta_r\}$ within the cluster, and $\mathcal{D}\chi = \prod_{j,n} d\chi_{j,\omega_n}$ in Eq. (3.18); χ_{j,ω_n} is the Grassmann

number corresponding to the Majorana operator c_j (more precisely, $c_j/\sqrt{2}$ following the notation in Ref. [107]). The effective action is given by

$$\mathcal{S}_{\rm eff}^{\{\eta_r\}} = -T\sum_{j,j',n\geq 0}\chi_{j,-\omega_n}(\mathcal{G}^0(i\omega_n))^{-1}_{j,j'}\chi_{j',\omega_n} + 2T\sum_{j,j',n\geq 0}\chi_{j,-\omega_n}\mathcal{H}^{\{\eta_r\}}_{j,j'}\chi_{j',\omega_n}. \tag{3.19}$$

For a given configuration of $\{\eta_r\}$, the impurity problem defined by Eq. (3.18) is exactly solvable because it is nothing but a free fermion problem. Green's function is obtained as

$$\left[(G^{\{\eta_r\}}(i\omega_n))^{-1}\right]_{j,j'} = \left[(\mathcal{G}^0(i\omega_n))^{-1}\right]_{j,j'} - 2\mathcal{H}^{\{\eta_r\}}_{j,j'}. \tag{3.20}$$

Then, local Green's function for the impurity problem is calculated by

$$G^{\rm imp}_{j,j'}(i\omega_n) = \sum_{\{\eta_r\}} P(\{\eta_r\})G^{\{\eta_r\}}_{j,j'}(i\omega_n), \tag{3.21}$$

where $P(\{\eta_r\})$ is the statistical weight for the configuration $\{\eta_r\}$ given by

$$P(\{\eta_r\}) = Z^{\{\eta_r\}}/\sum_{\{\eta_r\}} Z^{\{\eta_r\}}. \tag{3.22}$$

$Z^{\{\eta_r\}}$ is obtained from Green's functions as

$$Z^{\{\eta_r\}} = \prod_{n\geq 0}\det[-G^{\{\eta_r\}}(i\omega_n)]. \tag{3.23}$$

We note that $G^{\rm imp}(i\omega_n)$ in Eq. (3.21) is obtained exactly by computing $G^{\{\eta_r\}}(i\omega_n)$ and $P(\{\eta_r\})$ for all $2^{N_c/2}$ configurations of $\{\eta_r\}$ in the N_c-site cluster [110]. The self-energy for the impurity problem is obtained as

$$\Sigma_{j,j'}(i\omega_n) = \left[(\mathcal{G}^0(i\omega_n))^{-1}\right]_{j,j'} - \left[(G^{\rm imp}(i\omega_n))^{-1}\right]_{j,j'}. \tag{3.24}$$

In the CDMFT, the above equations, Eqs. (3.15), (3.16), (3.21), and (3.24), are solved in a self-consistent way. The self-consistent condition is given by

$$G(i\omega_n) = G^{\rm imp}(i\omega_n), \tag{3.25}$$

namely, the calculation is repeated until local Green's function in Eq. (3.15) agrees with Green's function calculated for the impurity problem in Eq. (3.21).

The Majorana CDMFT framework provides a concise calculation method for T dependences of static quantities of the Kitaev model, such as the specific heat and the equal-time spin correlations $\langle S^\gamma_j S^\gamma_{j'}\rangle$. It is worth noting that the CDMFT calculations can be performed without any biased approximation except for the cluster approximation: the exact enumeration for all the $2^{N_c/2}$ configurations in Eq. (3.21) enables the exact calculations for the given cluster. Furthermore, the cluster-size dependence is sufficiently small at all the T range above the critical temperature for the artificial phase transition due to the mean-field nature of the CDMFT, as demonstrated in Chap. 4. On the other hand, for obtaining dynamical quantities, such as the dynamical spin correlations $\langle S^\gamma_j(\tau)S^\gamma_{j'}\rangle$ (τ is the imaginary time), we need to make an additional effort beyond the exact enumeration in the CDMFT, as discussed in the next section. In the CDMFT+CTQMC calculations in Chap. 4, we mainly present the results for the 26-site cluster shown in Fig. 3.1(b). We also examine the dependence on the cluster size as well as shape in Chap. 4.

3.3 Continuous-time quantum Monte Carlo method

In order to calculate the dynamical spin correlations $\langle S_j^\gamma(\tau)S_{j'}^\gamma\rangle$, we need to take into account the imaginary-time evolution of the operators $\{\bar{c}\}$ that compose the conserved quantities $\{\eta_r\}$. This is because the spin operators include $\{\bar{c}\}$, e.g., $S_j^z(\tau) = \pm i\chi_j(\tau)\bar{c}_j(\tau)/\sqrt{2}$; the sign depends on the sublattice of site j, b or w in Eqs. (2.13) and (2.14). We need to calculate $\langle S_j^\gamma(\tau)S_{j'}^\gamma\rangle$ only with j and j' on a same γ bond, since other components are zero as introduced in Sec. 1.2.1. For this purpose, we combine the CTQMC method based on the strong coupling expansion [111] with Majorana QMC (QMC+CTQMC) and Majorana CDMFT (CDMFT+CTQMC). In the CDMFT+CTQMC, $\langle S_j^z(\tau)S_{j'}^z\rangle$ on a z bond r_0 is calculated as

$$\langle S_j^z(\tau)S_{j'}^z\rangle = \sum_{\{\eta_r\}',\eta_{r_0}=\pm 1} P(\{\eta_r\}',\eta_{r_0})\langle S_j^z(\tau)S_{j'}^z\rangle^{\{\eta_r\}'}, \tag{3.26}$$

where $\{\eta_r\}'$ represents the configurations of η_r except for η_{r_0} on the bond r_0. $P(\{\eta_r\}',\eta_{r_0})$ is obtained from the converged solution of the Majorana CDMFT in Sec. 3.2. $\langle S_j^z(\tau)S_{j'}^z\rangle^{\{\eta_r\}'}$ is the dynamical spin correlation on the bond r_0 calculated by the CTQMC method for each configuration $\{\eta_r\}'$. The sum of $\{\eta_r\}'$ runs over all possible configurations of $\{\eta_r\}'$ within the cluster. Note that Eq. (3.26) is derived from the fact that S_j^z commutes with η_r in $\{\eta_r\}'$, whereas it does not commute with η_{r_0}. Similarly, in the QMC+CTQMC, $\langle S_j^z(\tau)S_{j'}^z\rangle$ on a bond r_0 is calculated as

$$\langle S_j^z(\tau)S_{j'}^z\rangle = \frac{1}{N_{\rm MC}} \sum_{\{\eta_r\}'\in \text{MC samples}} \langle S_j^z(\tau)S_{j'}^z\rangle^{\{\eta_r\}'}, \tag{3.27}$$

by using the $\{\eta_r\}'$ configurations obtained in the Majorana QMC calculations.

Thus, for a given $\{\eta_r\}'$, the interaction lies only on the bond r_0, and hence, it is sufficient to solve the two-site impurity problem in the CTQMC calculations. The two-site impurity problem is defined by the integration in Eq. (3.18) on χ_{j,ω_n} whose j does not belong to the bond r_0. Then, we obtain

$$\mathcal{S}_{\rm eff}^{\{\eta_r\}'} = \mathcal{S}_{\rm local} + \mathcal{S}_{\rm hyb}^{\{\eta_r\}'}, \tag{3.28}$$

where

$$\mathcal{S}_{\rm local} = \sum_{j,j'}\int_0^\beta d\tau\chi_j(\tau)\left(\frac{\delta_{j,j'}}{2}\frac{\partial}{\partial\tau} + \mathcal{H}_{j,j'}^{\{\eta_r\}}\right)\chi_{j'}(\tau), \tag{3.29}$$

$$\mathcal{S}_{\rm hyb}^{\{\eta_r\}'} = -\sum_{j,j'}\int_0^\beta d\tau\int_0^\beta d\tau'\chi_j(\tau)\Delta_{j,j'}^{\{\eta_r\}'}(\tau-\tau')\chi_{j'}(\tau'), \tag{3.30}$$

and j, j' in Eqs. (3.29) and (3.30) are the sites on the bond r_0; $\beta = 1/T$ is the inverse temperature. In Eq. (3.30), the hybridization function $\Delta_{j,j'}^{\{\eta_r\}'}(\tau)$ is calculated from

$G^{\{\eta_r\}}_{j,j'}(i\omega_n)$ in the converged solution of CDMFT as follows. Let us define the matrix $\tilde{G}^{\{\eta_r\}}(i\omega_n)$ as a 2×2 submatrix of $G^{\{\eta_r\}}(i\omega_n)$, as

$$\tilde{G}^{\{\eta_r\}}_{j,j'}(i\omega_n) = G^{\{\eta_r\}}_{j,j'}(i\omega_n). \tag{3.31}$$

Then, the hybridization function is given as a function of the Matsubara frequency in the form

$$\Delta^{\{\eta_r\}'}_{j,j'}(i\omega_n) = [\tilde{G}^{\{\eta_r\}}(i\omega_n)]^{-1}_{j,j'} - (i\omega_n - 2\mathcal{H}^{\{\eta_r\}}_{j,j'}). \tag{3.32}$$

Note that $\Delta^{\{\eta_r\}'}_{j,j'}(i\omega_n)$ does not depend on η_{r_0} , which is straightforwardly shown by the matrix operations in the right hand side. Converting Eq. (3.32) to the imaginary-time representation, we obtain

$$\Delta^{\{\eta_r\}'}_{j,j'}(\tau) = \frac{T}{2}\sum_n e^{-i\omega_n\tau}\Delta^{\{\eta_r\}'}_{j,j'}(i\omega_n). \tag{3.33}$$

Given Eqs. (3.28)-(3.29), the partition function of the system is expanded in terms of $\mathcal{S}^{\{\eta_r\}'}_{\rm hyb}$ as

$$\begin{aligned}\frac{Z}{Z_{\rm local}} &= \frac{\int \mathcal{D}\chi e^{-\mathcal{S}^{\{\eta_r\}'}_{\rm hyb}} e^{-\mathcal{S}_{\rm local}}}{\int \mathcal{D}\chi e^{-\mathcal{S}_{\rm local}}} = \langle e^{-\mathcal{S}^{\{\eta_r\}'}_{\rm hyb}}\rangle_{\rm local} \\ &= \sum_{d,i_0,\ldots,i_{2d-1}} \int_0^\beta d\tau_0 \ldots \int_0^\beta d\tau_{2d-1} \frac{2^d}{(2d)!}\langle \chi_{i_0}(\tau_0)\ldots\chi_{i_{2d-1}}(\tau_{2d-1})\rangle_{\rm local} \\ &\qquad \times {\rm Pf}(\hat{\Delta}^{\{\eta_r\}'}(d,i_0,\tau_0,\ldots,i_{2d-1},\tau_{2d-1})),\end{aligned} \tag{3.34}$$

where $Z_{\rm local} = \int \mathcal{D}\chi e^{-\mathcal{S}_{\rm local}}$ is the partition function for the two sites described by $\mathcal{S}_{\rm local}$, and $\langle\mathcal{A}\rangle_{\rm local}$ represents the expectation value in the two-site problem as

$$\langle\mathcal{A}\rangle_{\rm local} = \frac{\int \mathcal{D}\chi \mathcal{A} e^{-\mathcal{S}_{\rm local}}}{\int \mathcal{D}\chi e^{-\mathcal{S}_{\rm local}}}. \tag{3.35}$$

In the second line of Eq. (3.34), d is the order of $\mathcal{S}^{\{\eta_r\}'}_{\rm hyb}$ in the expansion of $e^{-\mathcal{S}^{\{\eta_r\}'}_{\rm hyb}}$, ${\rm Pf}(M)$ is the Pfaffian of skew-symmetric matrix M, and $\hat{\Delta}^{\{\eta_r\}'}(d,i_0,\tau_0,\ldots,i_{2d-1},\tau_{2d-1})$ is a $2d\times 2d$ matrix, whose (m,n) element is given by

$$\hat{\Delta}^{\{\eta_r\}'}(d,i_0,\tau_0\ldots,i_{2d-1},\tau_{2d-1})_{m,n} = \Delta^{\{\eta_r\}'}_{i_m,i_n}(\tau_m-\tau_n). \tag{3.36}$$

We note that this is the first formulation of the CTQMC method with using the Pfaffian in the weight function to our knowledge, whereas a QMC simulation in the Majorana representation has been introduced for itinerant fermion models [112].

In the CTQMC calculation, we perform MC sampling over the configurations $(d,i_0,\tau_0,\ldots,i_{2d-1},\tau_{2d-1})$ by using the integrand in Eq. (3.34) as the statistical weight for each configuration. In each MC step, we perform an update from one configuration to another; for instance, an increase of the order of expansion d as

$(d, i_0, \tau_0, ..., i_{2d-1}, \tau_{2d-1})$ to $(d+1, i_0, \tau_0, ..., i_{2d-1}, \tau_{2d-1}, i_{2d}, \tau_{2d}, i_{2d+1}, \tau_{2d+1})$ by adding $(i_{2d}, \tau_{2d}), (i_{2d+1}, \tau_{2d+1})$. To judge the acceptance of such an update, we need to calculate the ratio of the Pfaffian. This is efficiently done by using the fast update algorithm, as in the hybridization expansion scheme for usual fermion problems (for example, see Ref. [113]). For the above example of increasing d, the ratio is calculated by adding two rows and columns in the matrix $\hat{\Delta}^{\{\eta\}'}$ as

$$\frac{\mathrm{Pf}(\hat{\Delta}^{\{\eta_r\}'}(d, i_0, \tau_0, ..., i_{2d-1}, \tau_{2d-1}))}{\mathrm{Pf}(\hat{\Delta}^{\{\eta_r\}'}(d+1, i_0, \tau_0, ..., i_{2d+1}, \tau_{2d+1}))}, \tag{3.37}$$

whose calculation cost is in the order of d^2 by using the fast update algorithm. On the other hand, in Eq. (3.34), $\langle T_\tau \chi_{i_0}(\tau_0) ... \chi_{i_{2d-1}}(\tau_{2d-1}) \rangle_{\mathrm{local}}$ is obtained as the average in the two-site problem, which can be calculated by considering the imaginary-time evolution of all the four states in the two-site problem. Then, the dynamical spin correlation for the configuration $\{\eta_r\}'$, $\langle S^z_j(\tau) S^z_{j'} \rangle^{\{\eta_r\}'}$ in Eqs. (3.26) and (3.27), is calculated as

$$\begin{aligned}\langle S^z_j(\tau) S^z_{j'} \rangle^{\{\eta_r\}'} = \frac{Z_{\mathrm{local}}}{Z} \sum_{d, i_0, ..., i_{2d-1}} \int_0^\beta d\tau_0 ... \int_0^\beta d\tau_{2d-1} \\ \times \frac{2^d}{(2d)!} \langle \chi_{i_0}(\tau_0) ... \chi_{i_{2d-1}}(\tau_{2d-1}) S^z_j(\tau) S^z_{j'} \rangle_{\mathrm{local}} \\ \times \mathrm{Pf}(\hat{\Delta}^{\{\eta_r\}'}(d, i_0, ..., i_{2d-1}, \tau_0, ..., \tau_{2d-1})).\end{aligned} \tag{3.38}$$

For the MC sampling, we need to evaluate

$$\frac{\langle T_\tau \chi_{i_0}(\tau_0) ... \chi_{i_{2d-1}}(\tau_{2d-1}) S^z_j(\tau) S^z_{j'} \rangle_{\mathrm{local}}}{\langle T_\tau \chi_{i_0}(\tau_0) ... \chi_{i_{2d-1}}(\tau_{2d-1}) \rangle_{\mathrm{local}}}. \tag{3.39}$$

This is again calculated by considering the imaginary-time evolution of all the four states in the two-site problem. In the isotropic case with $J_x = J_y = J_z$, $\langle S^\gamma_j(\tau) S^\gamma_{j'} \rangle$ for $\gamma = x(y)$ on a $x(y)$ bond is equivalent to $\langle S^z_{j''}(\tau) S^z_{j'''} \rangle$ on a z bond. Meanwhile, for the anisotropic case, we compute $\langle S^\gamma_j(\tau) S^\gamma_{j'} \rangle$ for $\gamma = x, y$ by the same technique described above with using the spin rotations $\{S^x, S^y, S^z\} \to \{S^y, S^z, S^x\}$ or $\{S^x, S^y, S^z\} \to \{S^z, S^x, S^y\}$.

In the CTQMC part of the CDMFT+CTQMC calculations in Chap. 4, for each configuration $\{\eta_r\}'$, we typically perform 5×10^5 measurements at every 20 MC steps, after 10^5 MC steps for the initial relaxation. We compute the dynamical spin correlations on the bond in the center of the cluster, as exemplified by r_0 in Fig. 3.1(b) for the case of 26-site cluster.

Meanwhile, in the CTQMC part of the QMC+CTQMC calculations in Chap. 5, for each configuration $\{\eta_r\}'$, we typically perform 5×10^3 measurements at every 20 MC steps, after 10^5 MC steps for initial relaxation. The number of $\{\eta_r\}'$ configurations, N_{MC}, is typically the order of 10^4. The CTQMC calculations are performed for the z bonds, sufficiently far from the open boundaries. Typically, we select 60 (16-18) bonds in the 2D (3D) case near the central region of the lattice (in order of

larger Manhattan distances from the open boundary), and average the results over the selected bonds. In the 2D case, the results for different system sizes well agree with each other, suggesting that the finite-size effect is negligible. In the 3D case, the results for χ and $1/T_1$ show small system size dependence at low T, in addition to those in the T derivatives of χ and $1/T_1$ reflecting the phase transition at T_c [90].

3.4 Maximum entropy method

By using the CDMFT+CTQMC or QMC+CTQMC method, we can numerically estimate the dynamical spin correlations as a function of the imaginary time, $\langle S_j^\gamma(\tau) S_{j'}^\gamma \rangle$. To obtain the physical observables, such as the dynamical spin structure factor and the NMR relaxation rate, which are given by the dynamical spin correlations as functions of real frequency ω, we need to inversely solve the equation given by the generic form $g(\tau) = \int d\omega \rho(\omega) e^{-\omega\tau}$. In our problem, $g(\tau)$ and $\rho(\omega)$ correspond to the dynamical spin correlations as functions of imaginary time τ and real frequency ω: $g(\tau) = \langle S_j^\gamma(\tau) S_{j'}^\gamma \rangle$ and $\rho(\omega) = S_{j,j'}^\gamma(\omega)$. In the following calculations, we utilize the Legendre polynomial expansion following Refs. [114, 115]:

$$g_m = \sqrt{2m+1} \int_0^\beta d\tau P_m(x(\tau)) g(\tau), \tag{3.40}$$

where $P_m(x)$ is the mth Legendre polynomials and $x(\tau) = 2\tau/\beta - 1$. Then, the inverse problem is given by

$$g_m = \int d\omega \rho(\omega) K_m(\omega), \tag{3.41}$$

where

$$K_m(\omega) = \sqrt{2m+1} \int_0^\beta d\tau P_m(x(\tau)) e^{-\omega\tau}. \tag{3.42}$$

In the present CDMFT+CTQMC and QMC+CTQMC calculations, we obtain $\langle S_j^\gamma(\tau) S_{j'}^\gamma \rangle$ at a discrete set of the imaginary time τ distributing with an equal interval. The number of the discrete points of τ is taken as 4192 at high T and as larger than 75β at low T, by which we confirm that the discretization error in the integration is negligible compared with the Monte Carlo error for the range of m used in the following calculations. We compute the Legendre coefficient, g_m in Eq. (3.40), by using the Romberg integration method (for example, see [116]) .

For solving the inverse problem, we adopt the maximum entropy method (MEM) [117]. The following procedure is the standard one, but we briefly introduce it to make the thesis self-contained. In the MEM, we discretize $\rho(\omega)$ to $\rho_l = \rho(\omega_l)$, and determine ρ_l to minimize the function

$$\mathcal{F} = \frac{1}{2} \sum_{m,n} (g_m - \tilde{g}_m) \zeta^{-1} C_{m,n}^{-1} (g_n - \tilde{g}_n) - \delta \sum_l \left[\rho_l - \rho_l^{(0)} - \rho_l \ln \left(\frac{\rho_l}{\rho_l^{(0)}} \right) \right], \tag{3.43}$$

where ζ and δ are the coefficients described below, and C is a variance-covariance matrix of g_m; $\tilde{g}_m = \sum_l \Delta\omega\rho_l K_m(\omega_l)$. We use the Legendre polynomial up to 100th order for $T \leq 0.006$ in 3D case, while we expand up to 50th order for higher T as well as for the 2D case. In Eq. (3.43), $\rho_l^{(0)}$ is the advance estimate of ρ_l, which we set to be a constant in this study.

Once neglecting the second term in the right hand side of Eq. (3.43), the minimization of $\mathcal{F}$ is equivalent to the least squares method. The least squares method is unstable, as g_m is rather insensitive to a change of ρ_l. The second term, called the entropy term, stabilizes the minimization process. In the following calculations, we set $\zeta = 625$ to sufficiently take into account the effect of the entropy term, where the value of δ is determined self-consistently in each MEM calculation based on the maximum likelihood estimation, called the classical MEM [117] (typically, $\delta \simeq$ 1-10). We note that the deviations of $\tilde{g}_m$ from g_m are typically comparable to the statistical errors in the CTQMC calculations. In the following results, we estimate the errors of $\rho(\omega)$ by the standard deviation between the data for $\zeta = 100$, 625 and 10000 in the range where the MEM retains the precision.

In the MEM, $\rho(\omega)$ should be positive for all ω. In our problem, the onsite correlation $S^\gamma_{j,j}(\omega)$ satisfies this condition automatically, whereas $S^\gamma_{j,j'}(\omega)$ for the NN sites j, j' on a γ bond, which is denoted by $S^\gamma_{\rm NN}(\omega)$ hereafter, can be negative. (Note that all the further-neighbor correlations beyond the NN sites vanish in the Kitaev model [29].) To obtain $S^\gamma_{\rm NN}(\omega)$ properly, we calculate $S^\gamma_{j,j}(\omega) + 2S^\gamma_{j,j'}(\omega) + S^\gamma_{j',j'}(\omega)$, which is positive definite for all ω, and subtract the onsite contributions [118]. The accuracy of $S^\gamma_{j,j'}(\omega)$ obtained by the MEM are examined in Appendix C in the one-dimensional limit with $J_z = 0$, where $S^\gamma_{j,j'}(\omega)$ can be calculated without using the MEM.

3.5 Physical quantities

In the following chapters, we calculate the dynamical quantities by the CDMFT+CTQMC and QMC+CTQMC methods for the Kitaev models on the 2D honeycomb (Fig. 1.1) and 3D hyperhoneycomb structures (Fig. 3.2). We calculate the dynamical spin structure factor $S(\mathbf{q}, \omega)$ by

$$S(\mathbf{q}, \omega) = \sum_\gamma S^\gamma(\mathbf{q}, \omega), \tag{3.44}$$

$$S^\gamma(\mathbf{q}, \omega) = \frac{1}{3N} \sum_{j,j'} e^{i\mathbf{q}\cdot(\mathbf{r}_j - \mathbf{r}_{j'})} S^\gamma_{j,j'}(\omega), \tag{3.45}$$

where $S^\gamma_{j,j'}(\omega)$ is obtained by the MEM described in Sec. 3.4 from the imaginary-time correlations $\langle S^\gamma_j(\tau) S^\gamma_{j'} \rangle$ by CDMFT+CTQMC or QMC+CTQMC. We present the results of $S(\mathbf{q}, \omega)$ on the symmetric lines shown in Fig. 3.3.

We also compute the NMR relaxation rate $1/T_1$. $1/T_1$ in the magnetic field

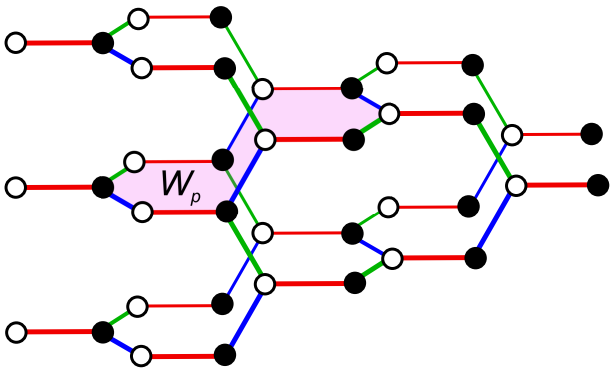

Figure 3.2: Schematic picture of the Kitaev model on the 3D hyperhoneycomb structure. The blue, green, and red bonds represent the x, y, and z bonds in Eq. (1.1), respectively. The magenta plaquette represents a conserved quantity W_p defined by a product of spin operators on the vertices of the plaquette; see Eq. (1.2). The black and white circles denote the sites j and j' in Eq. (1.10), respectively. They also correspond to b and w in Eq. (2.13).

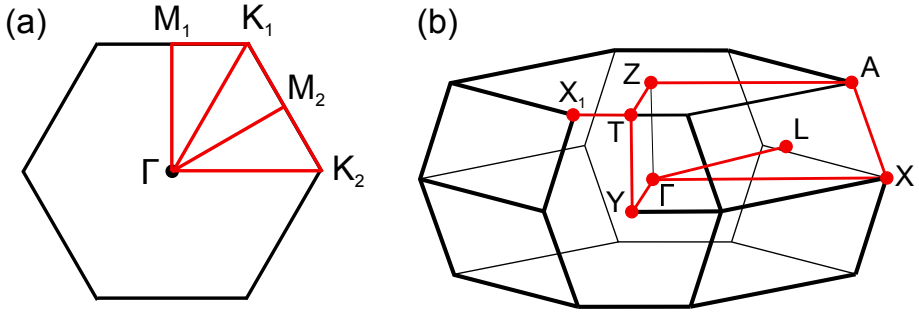

Figure 3.3: The first Brillouin zones for (a) the 2D honeycomb and (b) 3D hyperhoneycomb lattices. The red lines represent the symmetric lines used for plotting the dynamical structure factors $S(\mathbf{q},\omega)$ in Chaps. 4 and 5.

applied to the z direction, which is denoted by $1/T_1^z$, is given by

$$1/T_1^z \propto T \sum_{\mathbf{q}} |A_{\mathbf{q}}|^2 \frac{\mathrm{Im}\chi^{\perp}(\mathbf{q},\omega_0)}{\omega_0}. \tag{3.46}$$

Here, $A_{\mathbf{q}}$ is the hyperfine coupling constant, $\chi^{\perp}(\mathbf{q},\omega)$ is the dynamical susceptibility for the spin component perpendicular to the magnetic field direction, and ω_0 is the resonance frequency in the NMR measurement. The dynamical susceptibility $\chi(\mathbf{q},\omega)$ is related with the dynamical spin structure factor through the fluctuation-dissipation theorem, as

$$S(\mathbf{q},\omega) = \frac{1}{\pi(1-e^{-\beta\omega})}\mathrm{Im}\chi(\mathbf{q},\omega). \tag{3.47}$$

In the NMR experiments, ω_0 is in general negligibly small compared to the typical energy scale of the system, J. Thus, by taking the limit of $\omega_0 \to 0$ in Eq. (3.46) and using Eq. (3.47), we obtain

$$1/T_1^z = a_0 S^x_{j,j}(\omega = 0) + a_1 S^y_{j,j}(\omega = 0) + a_2 S^x_{\rm NN}(\omega = 0) + a_3 S^y_{\rm NN}(\omega = 0), \quad (3.48)$$

where the coefficients a_0, a_1, a_2, and a_3 are determined by $A_{\mathbf{q}}$. Similar equations are obtained for $1/T_1^x$ and $1/T_1^y$ by the cyclic permutation of x, y, z ($1/T_1^x = 1/T_1^y$ for the present cases from the symmetry). Because $A_{\mathbf{q}}$ depends on the details of the system, we here compute the onsite and NN-site components of $1/T_1$ separately with omitting the coefficients: the onsite components are calculated as

$$1/T_1^z = S^x_{j,j}(\omega = 0) + S^y_{j,j}(\omega = 0), \quad (3.49)$$
$$1/T_1^x = S^y_{j,j}(\omega = 0) + S^z_{j,j}(\omega = 0), \quad (3.50)$$

while the NN-site ones are

$$1/T_1^z = \pm(S^x_{\rm NN}(\omega = 0) + S^y_{\rm NN}(\omega = 0)), \quad (3.51)$$
$$1/T_1^x = \pm(S^y_{\rm NN}(\omega = 0) + S^z_{\rm NN}(\omega = 0)), \quad (3.52)$$

where the sign is $+(-)$ for the FM (AFM) case. Note that $1/T_1^x = 1/T_1^y$ in the following results where we take $J_x = J_y$. In the anisotropic cases $J_x = J_y \neq J_z$, the NN-site $1/T_1^x$ is not simply given by the sum in Eq. (3.52): it will be given by a linear combination of $S^y_{\rm NN}(\omega = 0)$ and $S^z_{\rm NN}(\omega = 0)$ with appropriate coefficients determined by $A_{\mathbf{q}}$. Such a linear combination, however, can be constructed from our data for Eqs. (3.51) and (3.52) by noting that $1/T_1^z = 2S^y_{\rm NN}(\omega = 0)$ for $J_x = J_y$. Hence, we present the results by Eqs. (3.51) and (3.52) for simplicity.

In addition, we calculate the magnetic susceptibility χ. χ for the magnetic field applied in the p direction, which we denote χ^γ, is obtained by

$$\chi^\gamma = \frac{1}{N} \sum_{j,j'} \int_0^\beta d\tau \langle S^\gamma_j(\tau) S^\gamma_{j'} \rangle. \quad (3.53)$$

Note that this is obtained directly from the dynamical spin correlations without the MEM.

4
Results by CDMFT + CTQMC method

In this chapter, we present the results obtained by the CDMFT+CTQMC methods. Before going into the main results, we present the benchmark of the CDMFT and CDMFT+CTQMC methods in Sec. 4.1. By comparing the results with those by the QMC method [91], we confirm that the CDMFT is valid in the T range above the artificial critical temperature close to the low-T crossover. Then, in Secs. 4.2, 4.3, 4.4, and 4.5, we present the CDMFT+CTQMC results for dynamical quantities, i.e., $S(\mathbf{q},\omega)$, $1/T_1$, χ, and the Korringa ratio $\mathcal{K}$, respectively, in the qualified T range. In Sec. 4.6, we examine how the dynamical properties are affected by the Z_2 variables $\{\eta_r\}$. Section 4.7 is devoted to the summary of this chapter.

For all quantities, we presents the results for the cases with both isotropic and anisotropic J_x, J_y, and J_z. In this chapter, we set the energy scale as $\sum_\gamma |J_\gamma| = 3$ (the average of J_γ is set to 1) in Eq. (2.1), and parametrize the anisotropy of the exchange coupling constants by using a parameter α as $J_x = J_y = \pm\alpha$ and $J_z = \pm(3-2\alpha)$, where + and − correspond to the ferromagnetic (FM) and antiferromagnetic (AFM) cases, respectively. The results are presented for $\alpha = 1.0$ ($J_x = J_y = J_z = \pm 1.0$), $\alpha = 0.8$ ($J_x = J_y = \pm 0.8$ and $J_z = \pm 1.4$) and $\alpha = 1.2$ ($J_x = J_y = \pm 1.2$ and $J_z = \pm 0.6$). We note that the FM and AFM cases are connected through unitary transformations [26].

4.1 Benchmark

4.1.1 CDMFT method

Figure 4.1 shows the benchmark of the Majorana CDMFT method. We compare the specific heat C_v and equal-time spin correlations for NN pairs on the γ bonds, $\langle S_j^\gamma S_{j'}^\gamma \rangle_{\rm NN}$, obtained by the Majorana CDMFT, with those by QMC in Ref. [91]. The data are calculated for the FM case. While the data of C_v are common to the FM and AFM cases, the sign of $\langle S_j^\gamma S_{j'}^\gamma \rangle_{\rm NN}$ is reversed for the AFM case. As indicated by two broad peaks in the specific heat in the QMC results, the system exhibits two crossovers owing to thermal fractionalization of quantum spins [91]; the crossover temperatures were estimated as $T_{\rm L} \simeq 0.012$ and $T_{\rm H} \simeq 0.375$ in the isotropic case. In the anisotropic cases, the low-T crossover takes place at a lower T, i.e., $T_{\rm L} \simeq 0.0052$ for $\alpha = 0.8$ and $T_{\rm L} \simeq 0.0075$ for $\alpha = 1.2$, while the high-T one is almost unchanged, i.e., $T_{\rm H} \simeq 0.375$. These behaviors are excellently reproduced by the Majorana CDMFT, except for the low-T peak; the CDMFT results show a sharp anomaly at $\tilde{T}_{\rm c} \simeq 0.015$ for $\alpha = 1.0$, $\tilde{T}_{\rm c} \simeq 0.0063$ for $\alpha = 0.8$ and $\tilde{T}_{\rm c} \simeq 0.013$ for

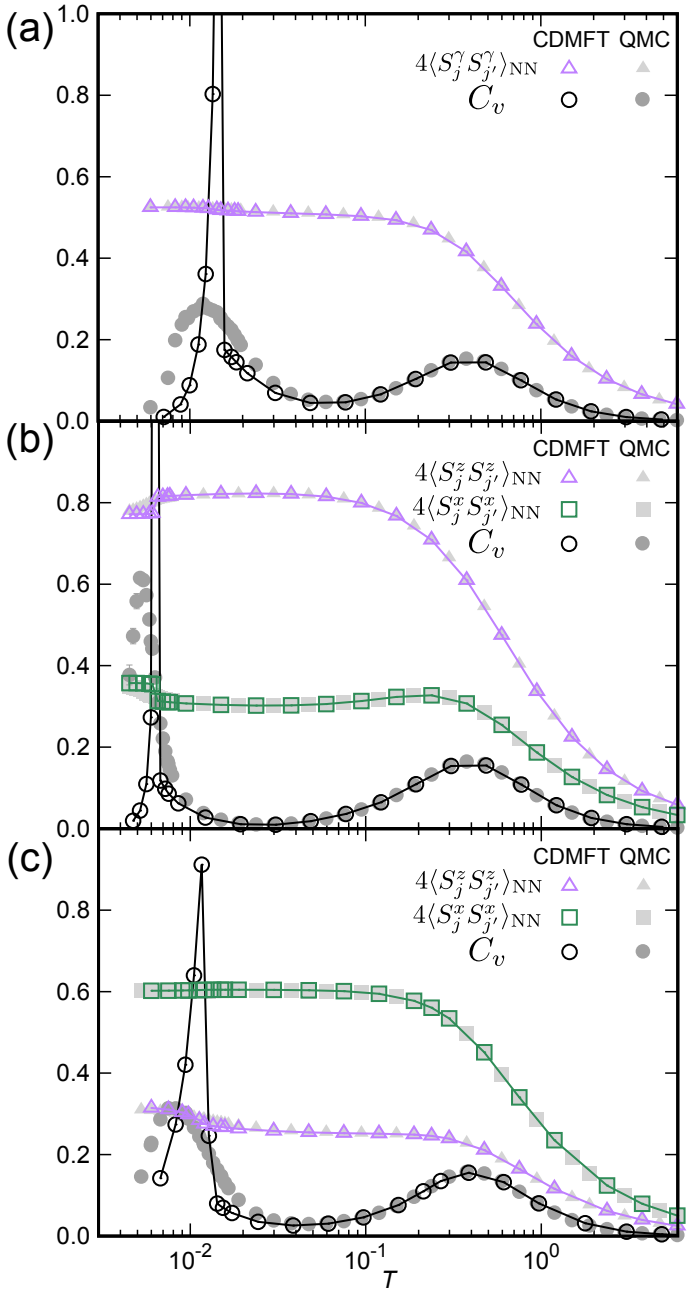

Figure 4.1: The specific heat C_v and equal-time spin correlations for the NN sites, $\langle S_j^z S_{j'}^z\rangle_{\rm NN}$ and $\langle S_j^x S_{j'}^x\rangle_{\rm NN}$, obtained by the Majorana CDMFT method for the FM case at (a) $\alpha = 1.0$, (b) $\alpha = 0.8$, and (c) $\alpha = 1.2$. Note that $\langle S_j^x S_{j'}^x\rangle_{\rm NN} = \langle S_j^y S_{j'}^y\rangle_{\rm NN} = \langle S_j^z S_{j'}^z\rangle_{\rm NN}$ for $\alpha = 1.0$ and $\langle S_j^x S_{j'}^x\rangle_{\rm NN} = \langle S_j^y S_{j'}^y\rangle_{\rm NN}$ for $\alpha = 0.8$ and 1.2, from the symmetry. QMC data in Ref. [91] are plotted by gray symbols for comparison.

$\alpha = 1.2$. This is due to a phase transition by ordering of η_r, which is an artifact of the mean-field nature of CDMFT. On the other hand, the QMC results for the NN spin correlations are also precisely reproduced by the Majorana CDMFT in the wide

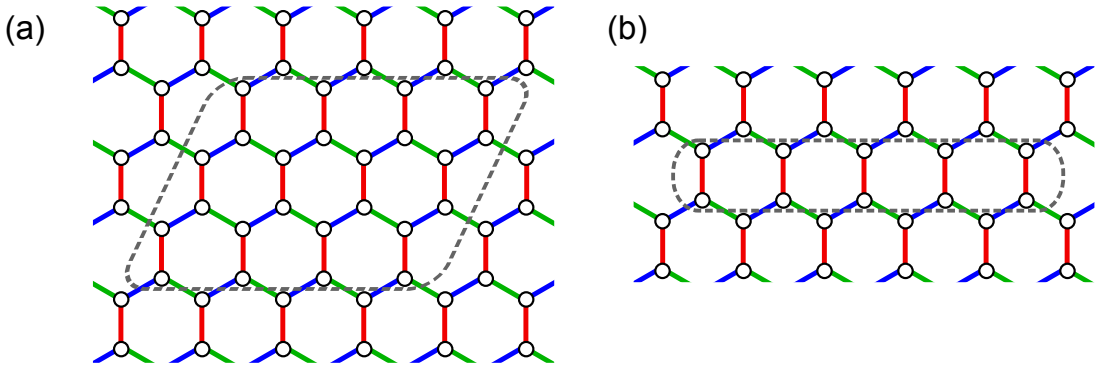

Figure 4.2: Schematic pictures of the different types of clusters used in the benchmark of CDMFT. The color of the bonds are common to Fig. 1.1.

T range above the artificial phase transition temperature $\tilde{T}_{\rm c}$. Although they appear to be reproduced even below $\tilde{T}_{\rm c}$, there is a small anomaly at $\tilde{T}_{\rm c}$ associated with the artificial transition, while the QMC data smoothly change around $T_{\rm L}$. (note that the appropriate sum of the NN spin correlations is nothing but the internal energy, and hence, the T derivative corresponds to the specific heat.) Thus, the comparison indicates that the Majorana CDMFT gives quantitatively precise results in the wide T range above the artificial transition temperature $\tilde{T}_{\rm c}$: in the present cases with $\alpha = 1.0$, 0.8 and 1.2, the CDMFT is reliable for $T \gtrsim 0.016$, $T \gtrsim 0.007$ and $T \gtrsim 0.014$, respectively. As discussed in the previous study [91], the thermal fractionalization of quantum spins sets in below $T \simeq T_{\rm H}$, which is well above $\tilde{T}_{\rm c}$. Thus, the T ranges qualified for the CDMFT include the peculiar paramagnetic state showing the thermal fractionalization.

4.1.2 CDMFT+CTQMC method

Figure 4.3 shows the cluster size dependence of χ^{γ} and $1/T_1^{\gamma}$ obtained by the CDMFT+CTQMC calculations for three different types of clusters shown in Figs. 3.1(b), 4.2(a), and 4.2(b). In each type, we change the cluster sizes in the width in the xy-chain direction while keeping that in the z-bond direction. This is because the width in the xy-chain direction is rather relevant compared to that in the z-bond direction in the present CDMFT, presumably due to the Majorana representation based on the Jordan-Wigner transformation along the xy chains. Hereafter, we define the size of the cluster by the average width in the xy-chain direction: for instance, 4.3 for the cluster in Fig. 3.1(b), while 4 and 5 for Figs. 4.2(a) and 4.2(b), respectively.

As shown in Figs. 4.3(a)-4.3(j), the CDMFT+CTQMC results for χ^{γ} show quick convergence with respect to the cluster width for all the cluster types. Even close to the artificial critical temperature $\tilde{T}_{\rm c}$, the results for the width larger than 4 are almost convergent to the large width limit for all types of the clusters: the remnant relative errors are $\lesssim 5\%$. Note that $\tilde{T}_{\rm c} \sim 0.014$ for $\alpha = 1.0$, $\tilde{T}_{\rm c} \sim 0.0063$ for $\alpha = 0.8$, and $\tilde{T}_{\rm c} \sim 0.013$ for $\alpha = 1.2$ (for the rotated lattice coordinate used to calculate

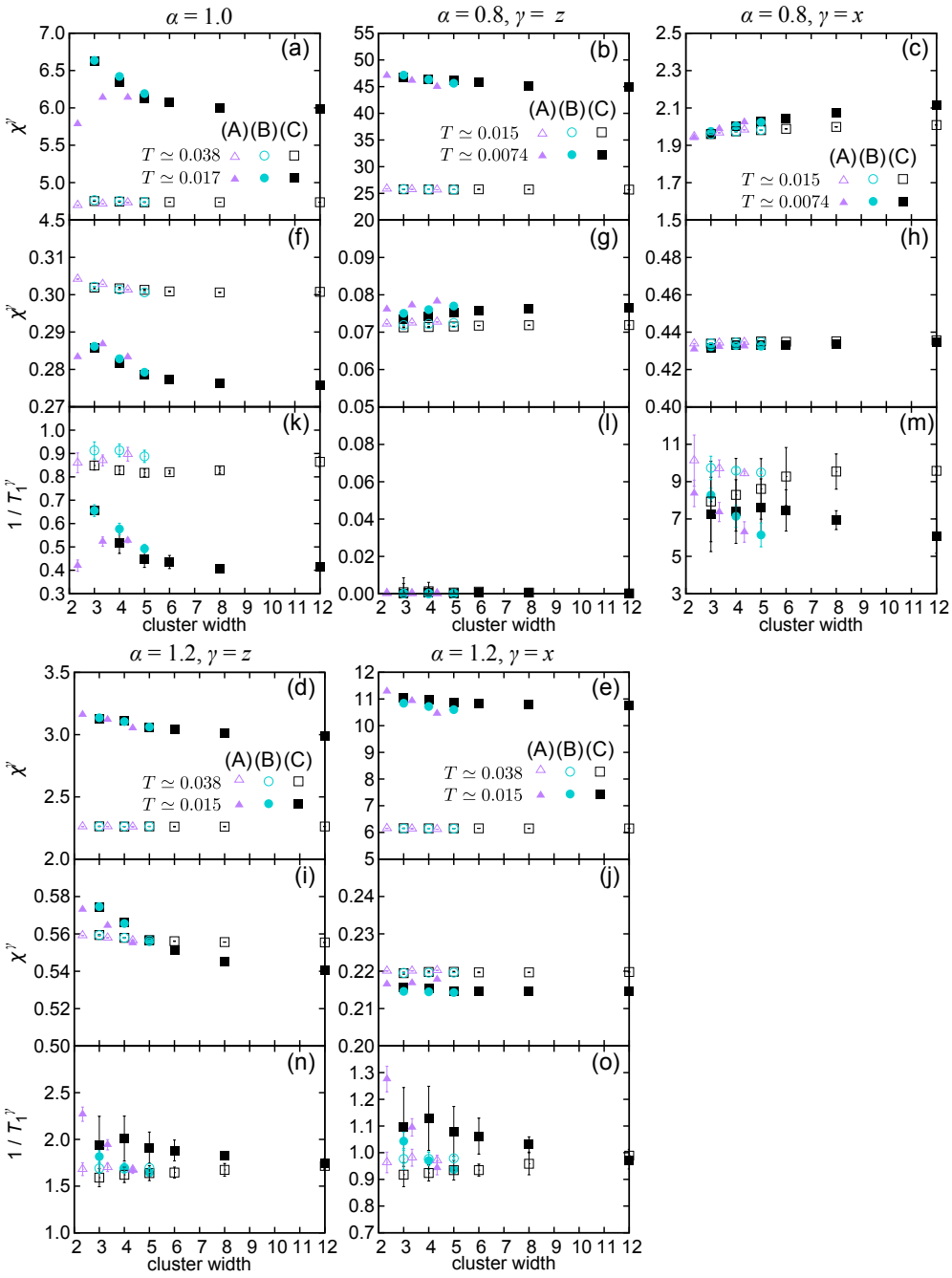

Figure 4.3: Cluster-size dependences of the magnetic susceptibility χ^γ for (a)-(e) the FM case and (f)-(j) the AFM case, and (k)-(o) the onsite component of the NMR relaxation rate $1/T_1^\gamma$: (a)(f)(k) $\alpha = 1.0$, (b)(c)(g)(h)(l)(m) $\alpha = 0.8$, and (d)(e)(i)(j)(n)(o) $\alpha = 1.2$. The data for two different T are plotted in each case. In (a)(f)(k), the data are common to $p = z$ and x. Calculations are performed for the cluster series denoted in (A) Fig. 3.1(b), (B) Fig. 4.2(a), and (C) Fig. 4.2(b). Symbols in (a)-(e) are common for the same parameters in (f)-(o).

$\langle S^p_j(\tau)S^p_{j'}\rangle$ for $p = x, y$, $\tilde{T}_c$ becomes slightly lower: $\tilde{T}_c \sim 0.0052$ for $\alpha = 0.8$ and $\tilde{T}_c \sim 0.0094$ for $\alpha = 1.2$).

On the other hand, as shown in Figs. 4.3(k)-4.3(o), the cluster-size dependences of $1/T_1$ remains up to relatively higher T than χ^γ. But the remnant relative errors are $\lesssim 10\%$ for the cluster width larger than 4, which are sufficiently small to observe the characteristic T dependences of $1/T_1$ as shown in Figs. 4.11.

In the following sections, we apply the CDMFT+CTQMC method in these qualified T ranges to the study of spin dynamics, which was not obtained by the previous QMC method [91]. Comparisons with the QMC+CTQMC results will be given in Sec. 5.1.

4.2 Dynamical spin structure factor

Figure 4.4 shows the dynamical spin structure factor $S(\mathbf{q},\omega)$ [Eq. (3.44)] at several T for the FM case with $\alpha = 1.0$, 0.8, and 1.2. The results are obtained by the CDMFT+CTQMC method supplemented by the MEM. The Brillouin zone and symmetric lines on which $S(\mathbf{q},\omega)$ is plotted are presented in Fig. 3.3(a). We show the data at four temperatures: $T \simeq 2T_L$, $\sqrt{T_L T_H}$, $0.64T_H$, and $6.4T_H$. note that $T_L \simeq 0.012$, 0.0052, and 0.0075 for $\alpha = 1.0$, 0.8, and 1.2, respectively, while $T_H \simeq 0.375$ for all the cases.

As shown in Fig. 4.4, at sufficiently high T than T_H, $S(\mathbf{q},\omega)$ does not show any significant $\mathbf{q}$ dependence for all α studied here; $S(\mathbf{q},\omega)$ shows only a diffusive response centered at $\omega \sim 0$, as shown in Figs. 4.4(j)-4.4(l). When lowering T below T_H, the diffusive weight is shifted to the positive ω region ranging up to above $\omega \sim J$ for all the cases, as shown in Figs. 4.4(g)-4.4(i). Simultaneously, a quasi-elastic component grows gradually at $\omega \sim 0$. Both the inelastic and the quasi-elastic components show a discernible $\mathbf{q}$ dependence; in particular, the latter increases the intensity around the Γ point reflecting the FM interactions. Overall T and ω dependences in the anisotropic cases are not much different from those in the isotropic case in the T range. Reflecting the anisotropy, we note slight modulation in the $\mathbf{q}$ dependences: while $S(K_1,\omega) = S(K_2,\omega)$ and $S(M_1,\omega) = S(M_2,\omega)$ for $\alpha = 1.0$ from the symmetry, the quasi-elastic response is small (large) around the M_1-K_1 line compared to that around the M_2-K_2 line for $\alpha = 0.8$ (1.2) because of the anisotropy.

When further lowering T and approaching T_L, the quasi-elastic component increases its intensity, while the inelastic response at $\omega \sim J$ does not change substantially, as shown in Figs. 4.4(a)-4.4(f). In this T region, we find distinct behavior between different α. In the case of $\alpha = 1.0$, as shown in Figs. 4.4(a) and 4.4(d), the quasi-elastic component of the $S(\mathbf{q},\omega)$ grows and sharpened but converges on the peak with finite width in the T = 0 solution [98]. The results for $\alpha = 1.2$ are qualitatively similar to those for $\alpha = 1.0$ in Figs. 4.4(a) and 4.4(d), except for different $\mathbf{q}$ dependence mentioned above.

On the other hand, in the case of $\alpha = 0.8$, as shown in Figs. 4.4(b) and 4.4(e), the quasi-elastic component is sharpened and develops to a δ-function like peak,

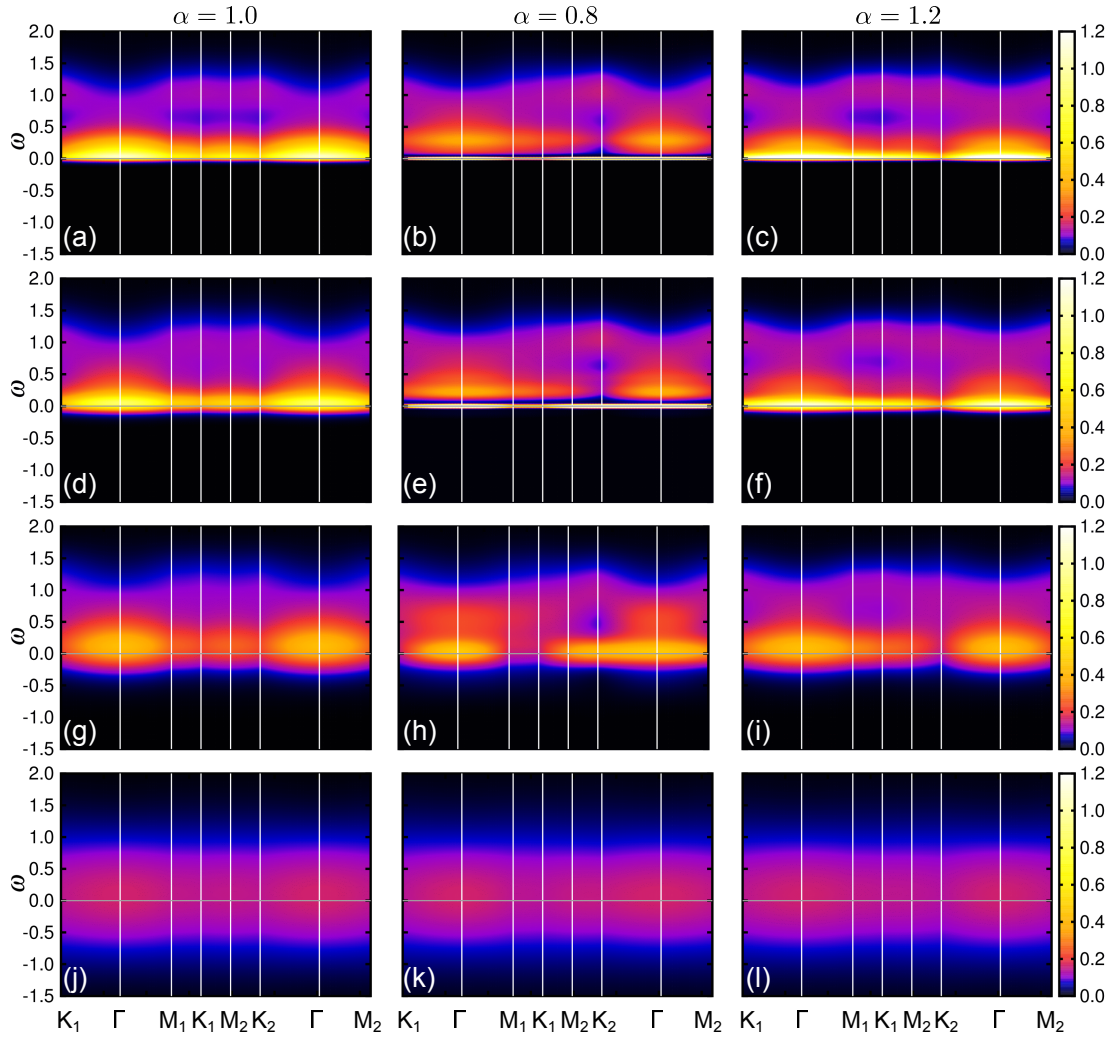

Figure 4.4: Dynamical spin structure factor $S(\mathbf{q},\omega)$ obtained by the Majorana CDMFT+CTQMC method for the FM case with (a)(d)(g)(j) $\alpha = 1.0$, (b)(e)(h)(k) $\alpha = 0.8$, and (c)(f)(i)(l) $\alpha = 1.2$: (a)(b)(c) $T \simeq 2T_{\rm L}$, (d)(e)(f) $T \simeq \sqrt{T_{\rm L}T_{\rm H}}$, (g)(h)(i) $T \simeq 0.64T_{\rm H}$, and (j)(k)(l) $T \simeq 6.4T_{\rm H}$. Here, $T_{\rm L} \simeq 0.012$, 0.0052, and 0.0075 for $\alpha = 1.0$, 0.8, and 1.2, respectively, while $T_{\rm H} \simeq 0.375$ for all the cases.

and in addition, the broad incoherent weight splits from the coherent peak. These behaviors are again consistent with the result at $T = 0$ [98]. Note that the δ-function peak at $T = 0$ appears due to the change of the parity between the ground state and the flux-excited state [98] (for the δ-function peak, see also Fig. C.2 in Appendix C).

Figure 4.5 shows the results for the AFM case. The overall ω dependence of $S(\mathbf{q},\omega)$ is similar to that for the FM case at all T: the diffusive response centered at $\omega \sim 0$ for $T \gtrsim T_{\rm H}$ [Figs. 4.5(j)-4.5(l)], the shift of the diffusive weight to the region of $\omega \sim J$ and the growth of a quasi-elastic component at $\omega \sim 0$ below $T_{\rm H}$ [Figs. 4.5(g)-4.5(i)], and the δ-function like peak for $\alpha = 0.8$ while approaching to $T_{\rm L}$ [Figs. 4.5(e) and 4.5(b)]. The similarity between FM and AFM cases is partly understood by the relation $2S(\mathrm{K}_1,\omega)_{\rm FM} + S(\mathrm{K}_2,\omega)_{\rm FM} = 2S(\mathrm{K}_1,\omega)_{\rm AFM} + S(\mathrm{K}_2,\omega)_{\rm AFM}$, which holds

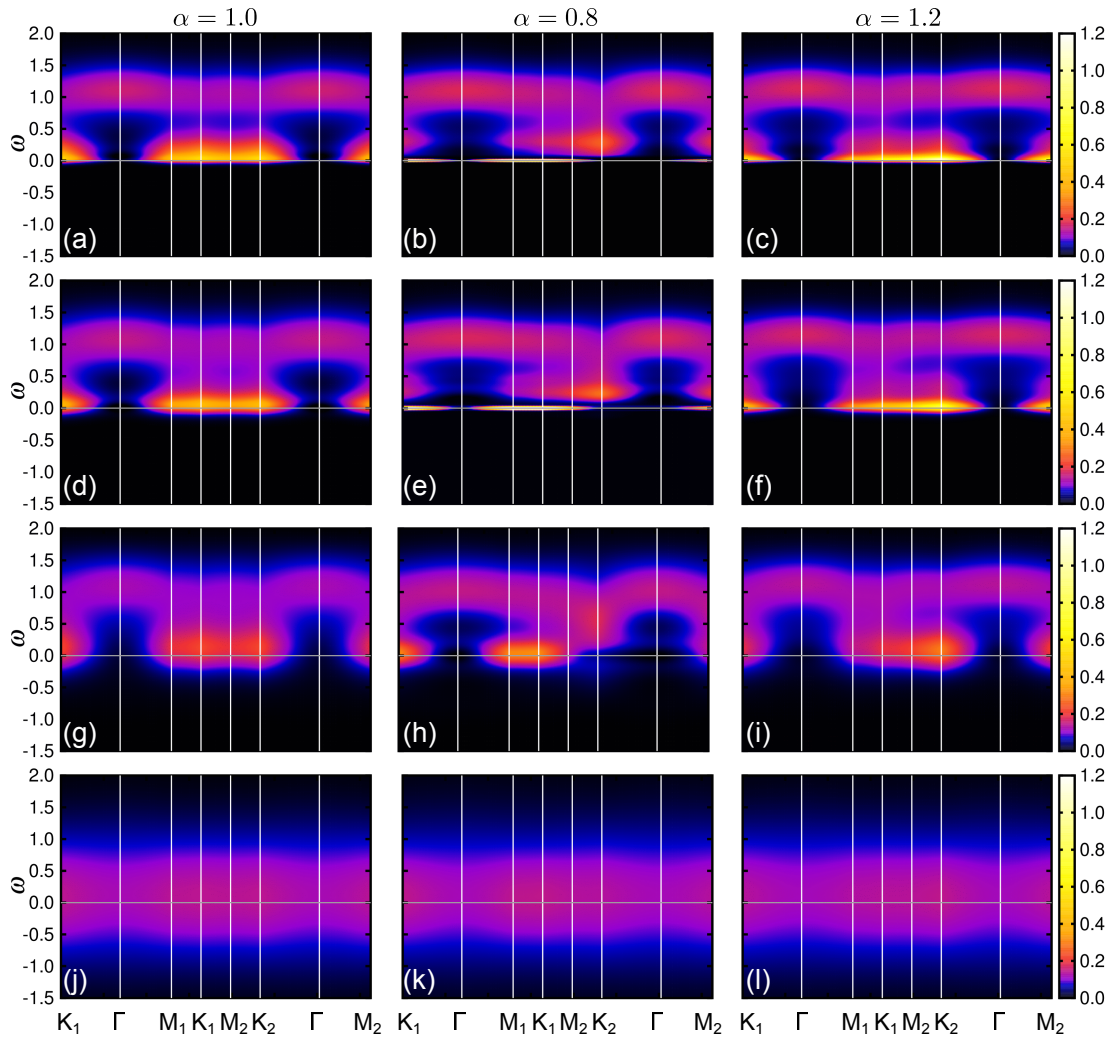

Figure 4.5: Dynamical spin structure factor $S(\mathbf{q},\omega)$ obtained by the Majorana CDMFT+CTQMC method for the AFM case. The values of α and T are common to Fig. 4.4.

for $J_x = J_y$ [$S(\mathbf{q},\omega)_{\rm FM}$ and $S(\mathbf{q},\omega)_{\rm AFM}$ are $S(\mathbf{q},\omega)$ for the FM and AFM cases, respectively]. On the other hand, the $\mathbf{q}$ dependence is in contrast to the FM case: while the weight of the quasi-elastic response almost vanishes around the Γ point, those on the zone boundary are enhanced in an almost opposite manner to the FM cases. In addition, the incoherent weight at $\omega \sim J$ also shows the opposite $\mathbf{q}$ dependence to the FM case: the weight is stronger around the Γ point than that on the zone boundary. The opposite $\mathbf{q}$ dependences between the FM and AFM cases directly follow from the relation $S(\mathbf{q},\omega)_{\rm AFM} = -S(\mathbf{q},\omega)_{\rm FM} + (2/3)\sum_\gamma S^\gamma_{j,j}(\omega)$.

In order to show the T dependences of $S(\mathbf{q},\omega)$ more explicitly, we present in Figs. 4.6-4.10 the T-ω plot of $S(\mathbf{q},\omega)$ at $\mathbf{q} = \Gamma$, K_1, and K_2 with the intensity profiles for the same set of T used in Figs. 4.4 and 4.5. Figure 4.6 shows the result for for both FM and AFM cases at $\alpha = 1.0$. Note that $S(\mathbf{q},\omega)$ at $\mathbf{q} = \mathrm{K}_1$ and $\mathbf{q} = K_2$ are equivalent at $\alpha = 1.0$, and $S(\mathrm{K},\omega)$ is same for the FM and AFM cases

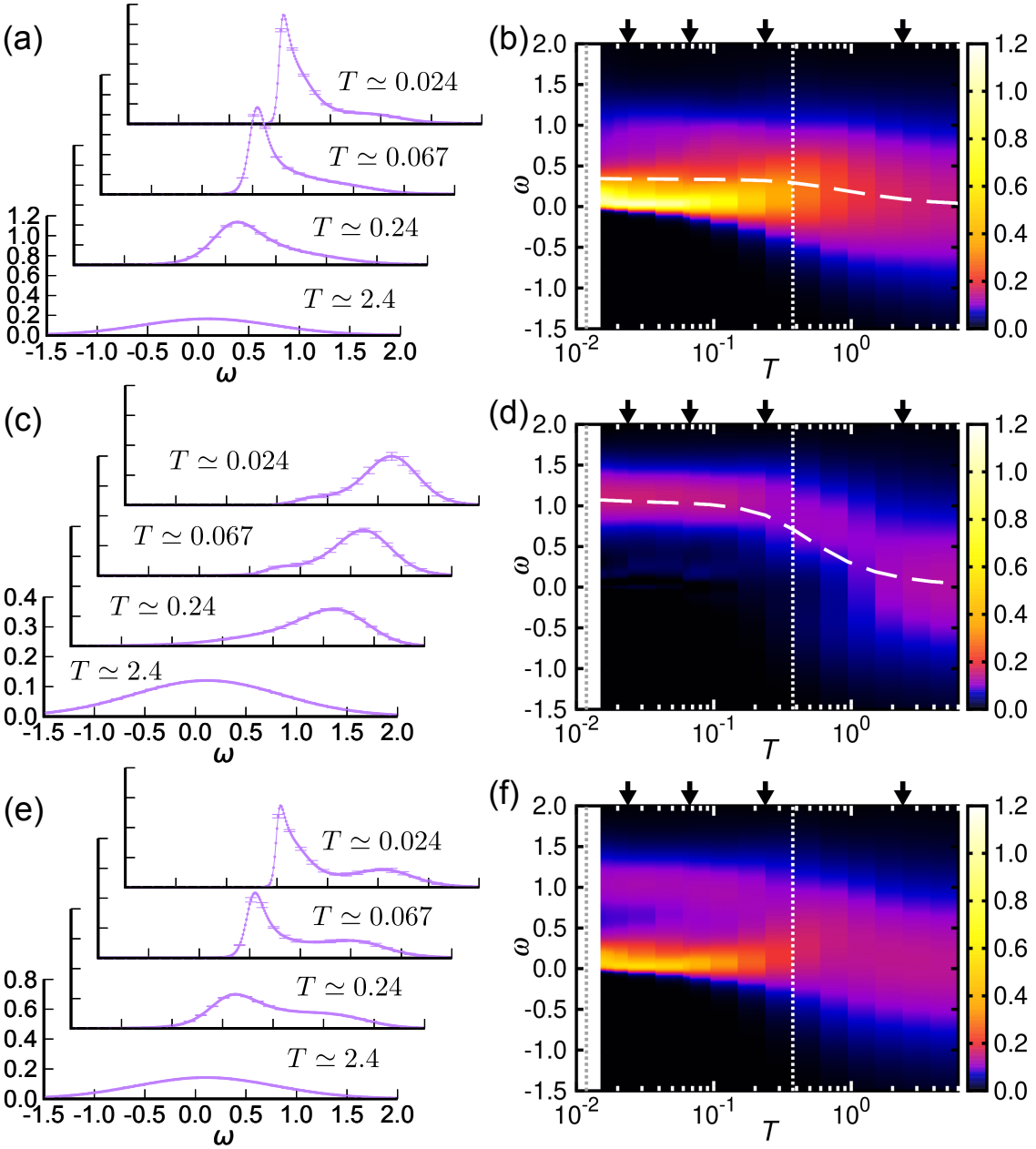

Figure 4.6: (a) $S(\Gamma, \omega)$ for the FM case, (c) $S(\Gamma, \omega)$ for the AFM case, and (e) $S(\mathrm{K}, \omega)$ for both the FM and AFM case with $\alpha = 1.0$ at several T. Note that $S(\mathrm{K}, \omega)$ is equivalent for the FM and AFM case. The corresponding contour plots in the T-ω plane are shown in (b)(d)(f). The arrows indicate the temperatures used for the data in (a)(c)(e), while the white and gray dotted lines indicate T_{H} and T_{L}, respectively. Note that the T set is common to that used in Figs. 4.4 and 4.5. The dashed curve in (b) represent the average frequency of $S(\Gamma, \omega)$ (see the text for details). In (a)(c)(e), the errorbars are shown for every ten data along the ω axis.

by symmetry. In the FM case, $S(\Gamma, \omega)$ and $S(\mathrm{K}, \omega)$ show qualitatively similar T-ω dependence, as shown in Figs. 4.6(a)(b) and 4.6(e)(f); the inelastic response at $\omega \sim J$

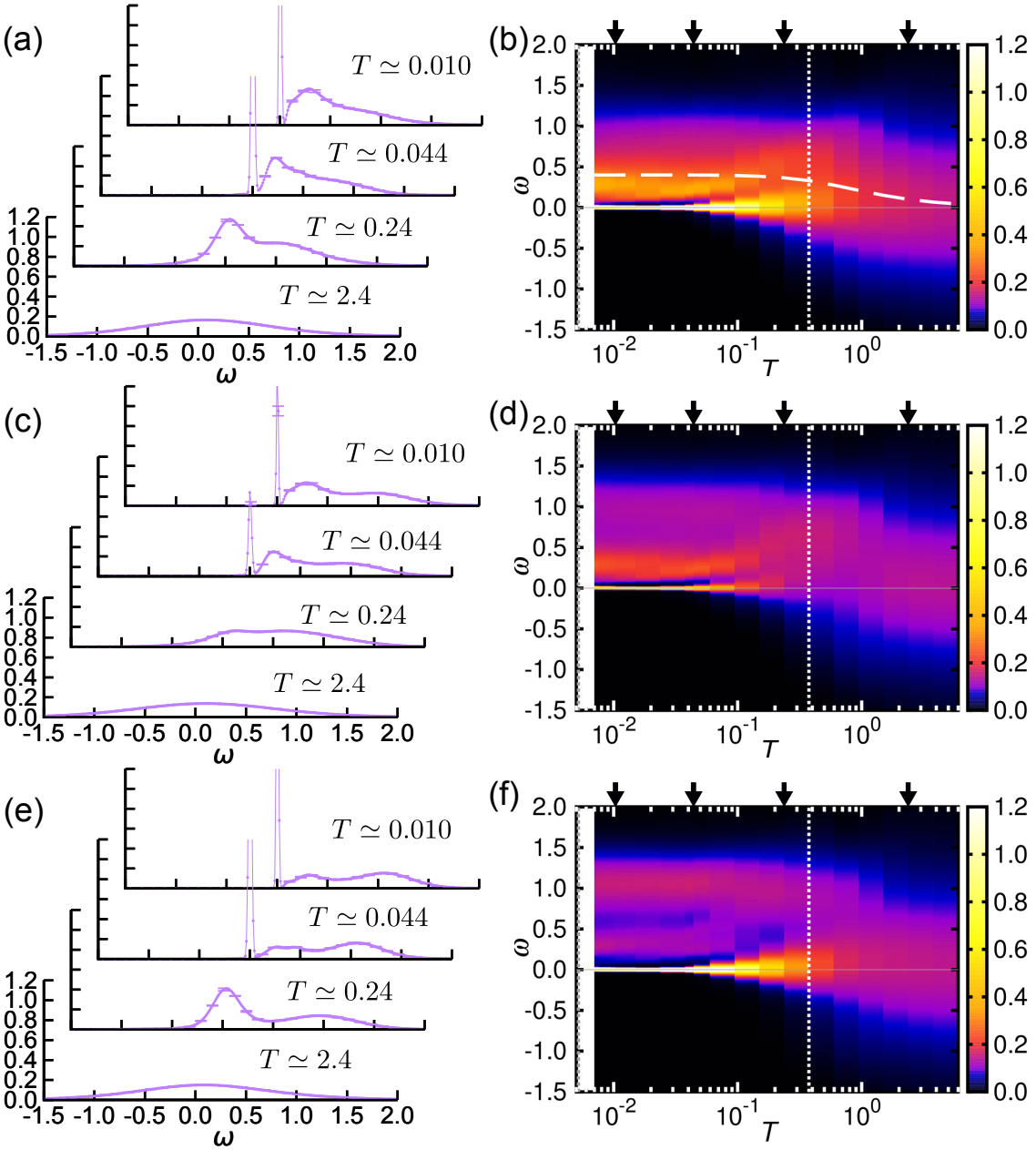

Figure 4.7: (a) $S(\Gamma, \omega)$, (c) $S(\mathrm{K}_1, \omega)$, and (e) $S(\mathrm{K}_2, \omega)$ for the FM case with $\alpha = 0.8$ at several T. The corresponding contour plots in the T-ω plane are shown in (b)(d)(f). The notations are common to those in Fig. 4.6.

appears below T_{H}, and the quasi-elastic one at $\omega \sim 0$ rapidly grows as approaching T_{L}. On the other hand, in the AFM case, the strong quasi-elastic intensity at low T is absent, while the inelastic response at $\omega \sim J$ arises below T_{H}, as in the FM case, as shown in Figs. 4.5(c)(d).

Figure 4.7 shows the result for the FM case at $\alpha = 0.8$. The overall weight of $S(\mathbf{q}, \omega)$ shifts from $\omega \sim 0$ to a large-ω region when the system is cooled down below $T \sim T_{\mathrm{H}}$. Below T_{H}, quasi-elastic response gradually grows and develops to

the δ-function like peak. The peak intensity in $S(\Gamma, \omega)$ and $S(\mathrm{K}_2, \omega)$ is larger than that for $S(\mathrm{K}_1, \omega)$, reflecting the anisotropy of the interaction.

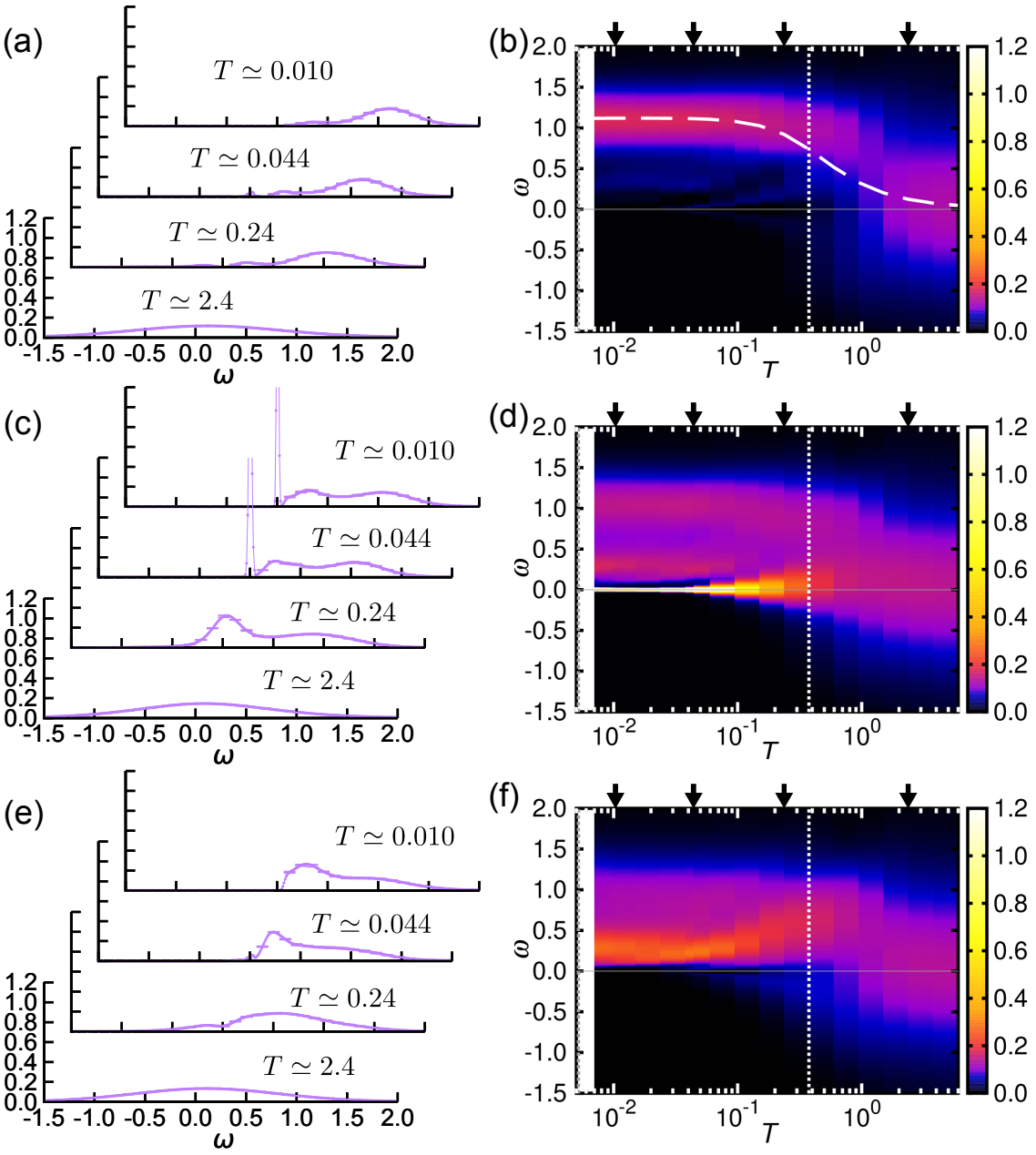

Figure 4.8: (a) $S(\Gamma, \omega)$, (c) $S(\mathrm{K}_1, \omega)$, and (e) $S(\mathrm{K}_2, \omega)$ for the AFM case with $\alpha = 0.8$ at several T. The corresponding contour plots in the T-ω plane are shown in (b)(d)(f). The notations are common to those in Fig. 4.7.

Figure 4.8 shows the corresponding plot for the AFM case at $\alpha = 0.8$. In contrast to the FM case, the strong quasi-elastic response is seen for $\mathbf{q} = \mathrm{K}_1$, which develops to the δ-function like peak at low T. We note that the dip and shoulder like structures around $\omega = 0$ in the intermediate T for the result at $\mathbf{q} = \mathrm{K}_2$ may be an

artifact originating from low precision in the MEM for this AFM case because of the following reason. As described in Sec. 3.4, we calculate $S^{\gamma}_{j,j'}(\omega)$ for the NN bonds by subtracting the onsite component $S^{\gamma}_{j,j}(\omega)$ from $S^{\gamma}_{j,j}(\omega) + S^{\gamma}_{j,j'}(\omega)$, both of which are obtained by the MEM. In the present case, as both of $S^{z}_{j,j}(\omega)$ and $S^{z}_{j,j}(\omega) + S^{z}_{j,j'}(\omega)$ become large around $\omega = 0$ due to the development of the δ-function like peak, the relative error becomes large for $S(\mathrm{K}_2, \omega \sim 0)$, which may lead to artificial structures.

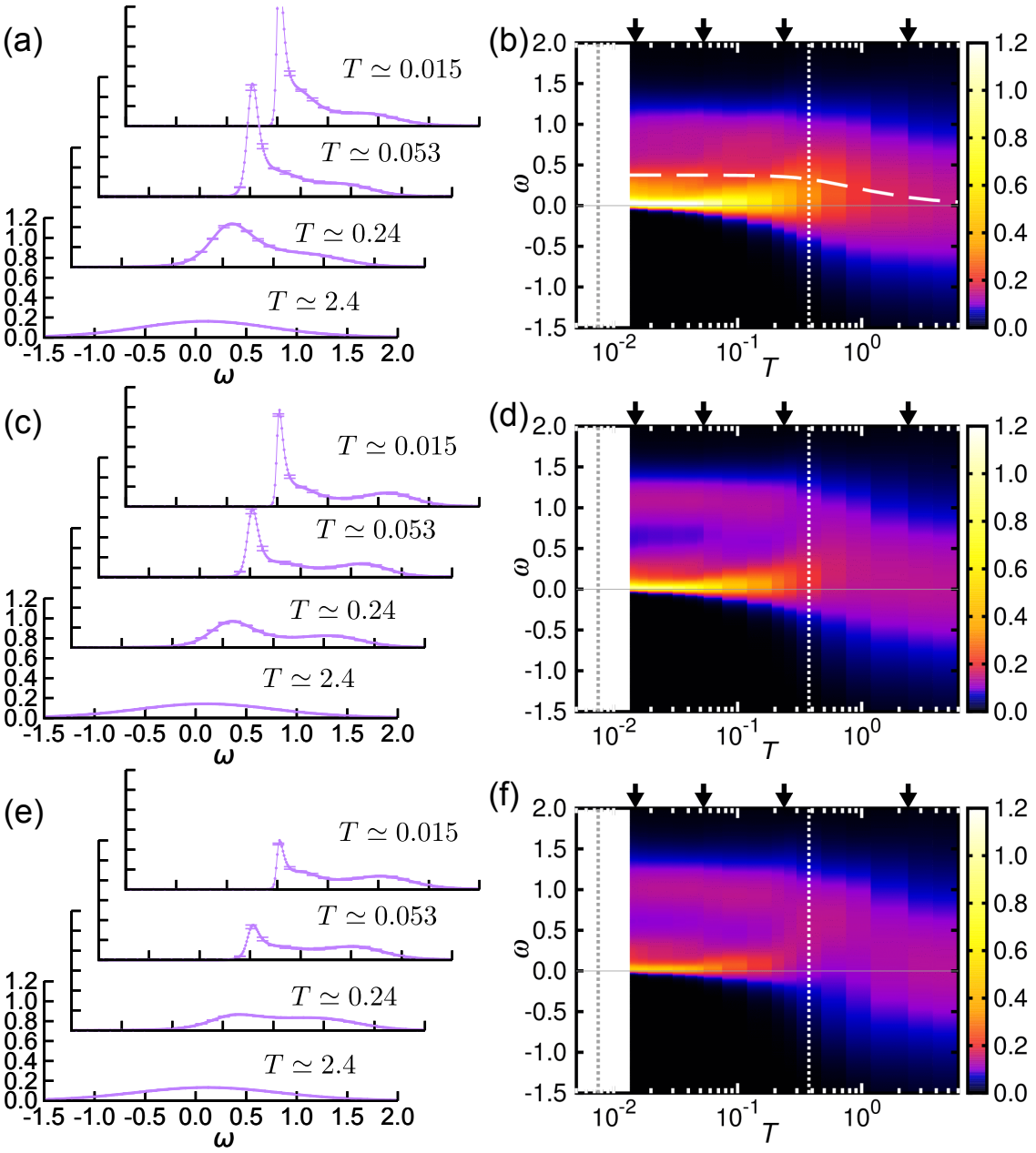

Figure 4.9: (a) $S(\Gamma, \omega)$, (c) $S(\mathrm{K}_1, \omega)$, and (e) $S(\mathrm{K}_2, \omega)$ for the FM case with $\alpha = 1.2$ at several T. The corresponding contour plots in the T-ω plane are shown in (b)(d)(f). The notations are common to those in Fig. 4.7.

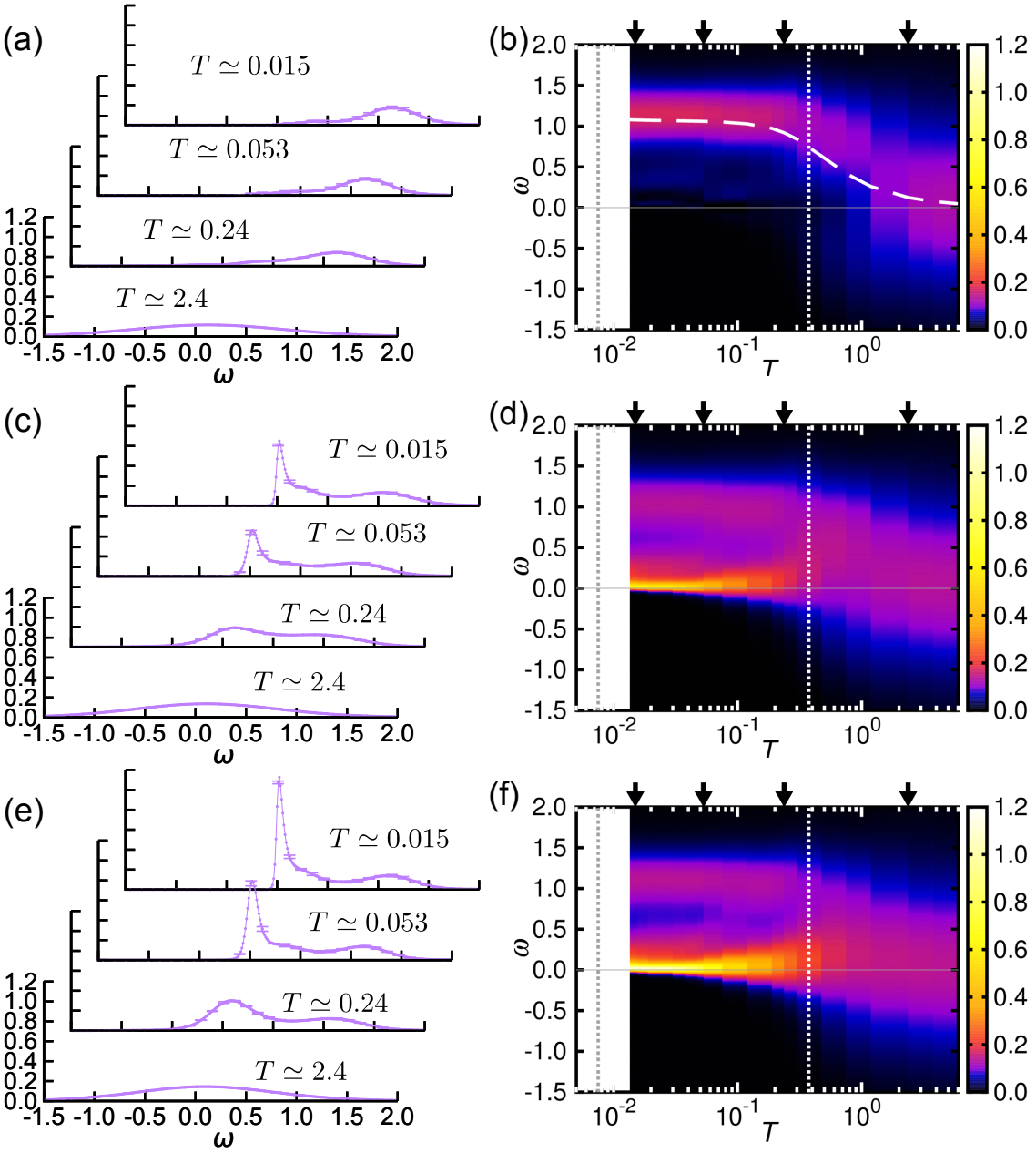

Figure 4.10: (a) $S(\Gamma, \omega)$, (c) $S(\mathrm{K}_1, \omega)$, and (e) $S(\mathrm{K}_2, \omega)$ for the AFM case with $\alpha = 1.2$ at several T. The corresponding contour plots in the T-ω plane are shown in (b)(d)(f). The notations are common to those in Fig. 4.7.

Figures 4.9 and 4.10 show the results at $\alpha = 1.2$. As observed in Figs. 4.4 and 4.5, $S(\mathbf{q}, \omega)$ for both the FM and AFM cases behave similarly to those at $\alpha = 1.0$. In the anisotropic cases, however, the difference between $S(\mathrm{K}_1, \omega)$ and $S(\mathrm{K}_2, \omega)$ is obvious: the quasi-elastic peak for $S(\mathrm{K}_1, \omega)$ is larger (smaller) than that for $S(\mathrm{K}_2, \omega)$ in the FM (AFM) case.

There is a relation between the static spin correlation and the average frequency of $S(\Gamma, \omega)$, $\bar{\omega} \equiv \int \omega S(\Gamma, \omega) d\omega / \int S(\Gamma, \omega) d\omega$, originating from the sum rule

for $S(\mathbf{q},\omega)$. T dependences of $\bar{\omega}$ are shown by white dashed curves in Figs. 4.6(a), 4.6(b), 4.7(b), 4.8(b), 4.9(b), and 4.10(b). In all cases, $\bar{\omega}$ is nearly zero for sufficiently high T, but it grows at $T \sim T_{\rm H}$ and becomes almost independent of T for $T \lesssim T_{\rm H}$. These T dependences are similar to those of the static spin correlation between the NN sites shown in Fig. 4.1.

4.3 NMR relaxation rate

Figure 4.11 shows the NMR relaxation rate $1/T_1$ obtained by the CDMFT+CTQMC method supplemented by the MEM [see Eqs. (3.49)-(3.52)]. As shown in Fig. 4.11, for all cases, the onsite component of $1/T_1^\gamma$ is nonzero and almost T independent above $T \sim T_{\rm H}$, as expected for the conventional paramagnets [119]. On the other hand, the NN-site component is zero in the high-T limit and increases as decreasing T. This behavior corresponds to the development of NN-site static spin correlations shown in Sec. 4.1.1, as they have a relation through the sum rule, $\int S^\gamma_{j,j'}(\omega)d\omega = \langle S^\gamma_j S^\gamma_{j'}\rangle$.

Below $T_{\rm H}$, however, $1/T_1^\gamma$ at $\alpha = 1.0$ for both onsite- and NN-components increase and show a peak at slightly above $T_{\rm L}$, despite the saturation of equal-time correlations. The pronounced peak is regarded as the consequence of thermally excited fluxes above $T_{\rm L}$, as the suppression of $1/T_1$ for $T \lesssim T_{\rm L}$ is due to the formation of the flux gap in the low-T limit [26].

In the case for $\alpha = 0.8$, the increase of $1/T_1^x$ below $T_{\rm H}$ is substantial, as shown in Fig. 4.11(b). The enhancement is much larger than the case of $\alpha = 1.0$ in Fig. 4.11(a). This is due to the evolution of the δ-function like peak in $S^z(\mathbf{q},\omega)$ discussed in Sec. 4.2. In contrast, $S^x(\mathbf{q},\omega)$ and $S^y(\mathbf{q},\omega)$ do not develop such δ-function like peaks, and hence, $1/T_1^z$ does not show enhancement unlike $1/T_1^x$. While further decreasing T, $1/T_1^x$ shows a peak slightly above $T_{\rm L}$. The decrease at low T reflects a spin gap originating from the nonzero flux gap in the ground state as in the case of $\alpha = 1.0$ [26]. On the other hand, the onsite and NN-site components of $1/T_1^z$ are both suppressed below $T \sim T_{\rm H}$, after showing a plateau and broad peak, respectively. The suppression of $1/T_1^z$ is due to an increase of energy cost for a spin flip on the strong z bond under the well-developed static spin correlations between NN sites in this T range. Actually, the energy cost is represented by the average frequency of $S^x_{j,j}(\omega)$ as there is a relation

$$\begin{aligned}\bar{\omega}^x_{\rm onsite} &= \frac{\int \omega S^x_{j,j}(\omega)d\omega}{\int S^x_{j,j}(\omega)d\omega} \\ &= \frac{\sum_{m,n} e^{-\beta E_n}(E_m - E_n)|\langle m|S^x_j|n\rangle|^2}{\frac{1}{4}\sum_n e^{-\beta E_n}}. \end{aligned} \tag{4.1}$$

On the other hand, $\bar{\omega}^x_{\rm onsite}$ is also written as $\bar{\omega}^x_{\rm onsite} = (J_y\langle S^y_j S^y_{j'}\rangle_{\rm NN} + J_z\langle S^z_j S^z_{j'}\rangle_{\rm NN})/2$ by the sum rule [120]. Thus, the energy cost becomes large below $T_{\rm H}$ according to the growth of $\langle S^z_j S^z_{j'}\rangle_{\rm NN}$.

In contrast, as shown in Fig. 4.11(c), T dependence of $1/T_1^\gamma$ at $\alpha = 1.2$ is similar

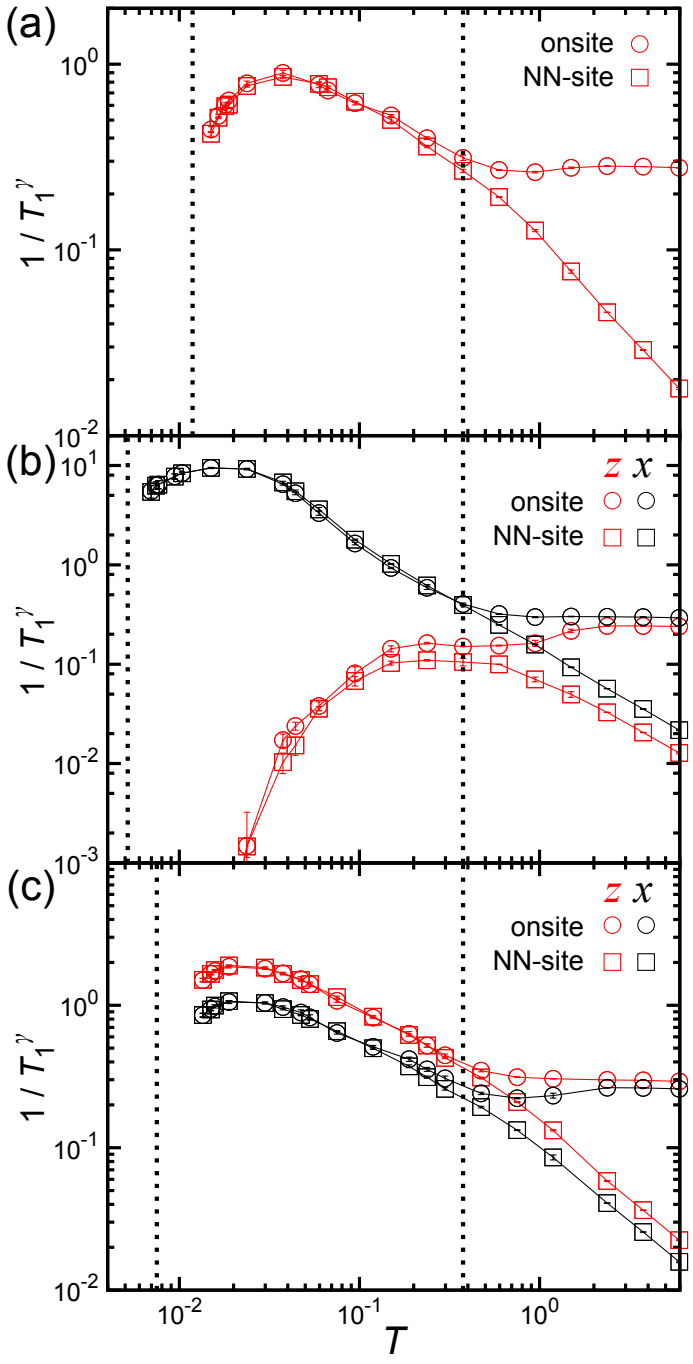

Figure 4.11: T dependences of the NMR relaxation rate $1/T_1^\gamma$ ($\gamma = z, x$) at (a) $\alpha = 1.0$, (b) $\alpha = 0.8$, and (c) $\alpha = 1.2$. note that $1/T_1^z = 1/T_1^x$ for $\alpha = 1.0$ and $1/T_1^x = 1/T_1^y$ for all the cases from the symmetry. The vertical dotted lines indicate $T_{\rm L}$ and $T_{\rm H}$ for each α.

to that at $\alpha = 1.0$ in Fig. 4.11(a). Reflecting the asymmetry, however, $1/T_1^z$ is larger than $1/T_1^x$.

Although the system is described by free Majorana fermions coupled to local-

ized Z_2 variables $\{\eta_r\}$, the NMR relaxation rate does not obey the Korringa law, $1/(T_1T) \sim$ constant, which is expected for free fermion systems. This is natural because the spin-flip excitation in the NMR process is a composite of both itinerant matter fermions and localized Z_2 variables $\{\eta_r\}$. Nonetheless, for comparison to forth-coming experiments, we plot the Korringa ratio as a function of T in Sec. 4.5.

4.4 Magnetic susceptibility

Figures 4.12 and 4.13 show the T dependences of the magnetic susceptibility χ^γ for the FM and AFM cases, respectively, calculated by Eq. (3.53). In all the cases, at sufficiently high T compared to the dominant J_γ, χ^γ obeys the Curie-Weiss law,

$$\chi^\gamma_{\rm CW} = \frac{1}{4T - J_\gamma}, \tag{4.2}$$

which is obtained by the standard mean-field approximation in the original spin representation. While decreasing T, χ^γ shows a suppression from $\chi^\gamma_{\rm CW}$ below $T \sim J_\gamma$, despite the enhancement of $1/T_1^\gamma$ except for the case of $\alpha = 0.8$ and $\gamma = z$.

Among the results, χ^x for the FM case and χ^z for the AFM case at $\alpha = 0.8$ show peculiar T dependences at low T. The former largely deviates from the Curie-Weiss behavior and saturates to a small nonzero value, as shown in Fig. 4.12(b) [121]. Meanwhile, the latter shows a broad hump at $T \sim T_{\rm H}$ and decreases as lowering T, as shown in Fig. 4.13(b). These T dependences are qualitatively understood by considering a two-site dimer model on the z bond obtained by setting $J_x = J_y = 0$. The dimer model gives the analytical forms for the magnetic susceptibility as

$$\chi^z_{\rm dimer} = \frac{\beta}{2}\frac{\exp(\beta J_z/4)}{\exp(\beta J_z/4) + \exp(-\beta J_z/4)}, \tag{4.3}$$

$$\chi^x_{\rm dimer} = \frac{1}{J_z}\tanh\left(\beta\frac{J_z}{4}\right). \tag{4.4}$$

The results are plotted by the dashed-dotted curves in Figs. 4.12(b) and 4.13(b). $\chi^x_{\rm dimer}$ for the FM case almost saturates around $T \sim J_z/4$, as the dominant J_z interaction suppresses the magnetization in the x direction. This accounts for the behavior of χ^x in Fig. 4.12(b) qualitatively. Meanwhile, $\chi^z_{\rm dimer}$ also well reproduces a hump at $T \sim 0.5$ in χ^z for the AFM case in Fig. 4.13(b); χ^z remains nonzero down to low T as nonzero J_x and J_y smear out the dimer gap.

In the case of $\alpha = 1.2$, T dependences of χ^γ shown in Figs. 4.12(c) and 4.13(c) are similar to those for $\alpha = 1.0$ shown in Figs. 4.12(a) and 4.13(a), respectively; The effect of anisotropic J_γ, however, is clearly observed: the stronger interactions on the x, y bonds than the z bond result in larger (smaller) χ^x than χ^z in the FM (AFM) case. In addition, the temperature of the broad peak of χ^z (χ^x) in the AFM case shifts to a lower (higher) T than that for $\alpha = 1.0$.

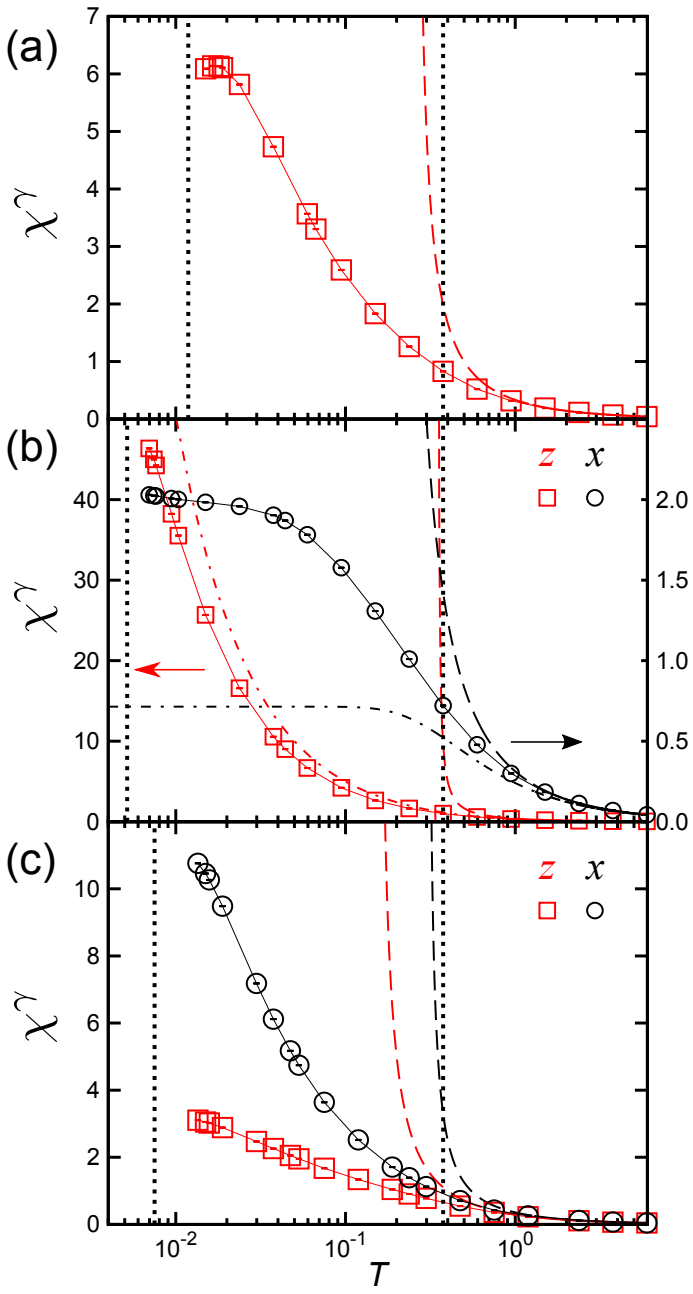

Figure 4.12: T dependences of the magnetic susceptibility χ^γ ($\gamma = z, x$) at (a) $\alpha = 1.0$, (b) $\alpha = 0.8$, and (c) $\alpha = 1.2$ for the FM case. The dashed curves represent $\chi^\gamma_{\rm CW}$ in Eq. (4.2). The red and black dashed-dotted curves in (b) represent $\chi^\gamma_{\rm dimer}$ for $\gamma = z$ [Eq. (4.3)] and $\gamma = x$ [Eq. (4.4)], respectively. Note that $\chi^z = \chi^x$ for $\alpha = 1.0$ and $\chi^x = \chi^y$ for all the cases from the symmetry. The vertical dotted lines indicate $T_{\rm L}$ and $T_{\rm H}$ for each α.

4.5 Korringa ratio

Figures 4.14 and 4.15 display the T dependences of the Korringa ratio defined as

$$\mathcal{K}^\gamma = \frac{1}{T_1^\gamma T (\chi^\gamma)^2}, \tag{4.5}$$

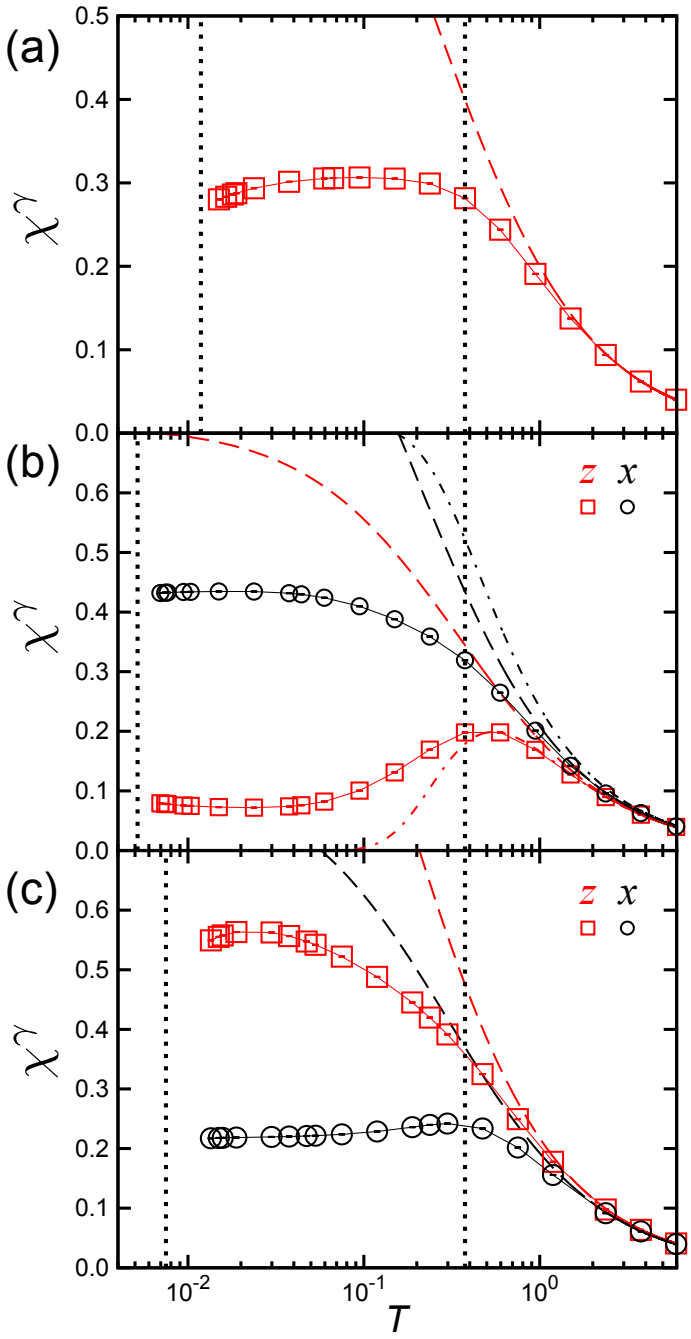

Figure 4.13: T dependences of the magnetic susceptibility χ^γ ($\gamma = z, x$) at (a) $\alpha = 1.0$, (b) $\alpha = 0.8$, and (c) $\alpha = 1.2$ for the AFM case. The notations are common to those in Fig. 4.12.

which is computed by using the NMR relaxation rate $1/T_1^\gamma$ and the magnetic susceptibility χ^γ obtained in Sec. 4.3 and 4.4. Interestingly, as shown in Fig. 4.14(a), $\mathcal{K}^\gamma$ for the isotropic FM case is almost constant close to 1 for $T_{\rm L} \lesssim T \lesssim T_{\rm H}$, which is apparently consistent with the behavior expected for free electron systems. This

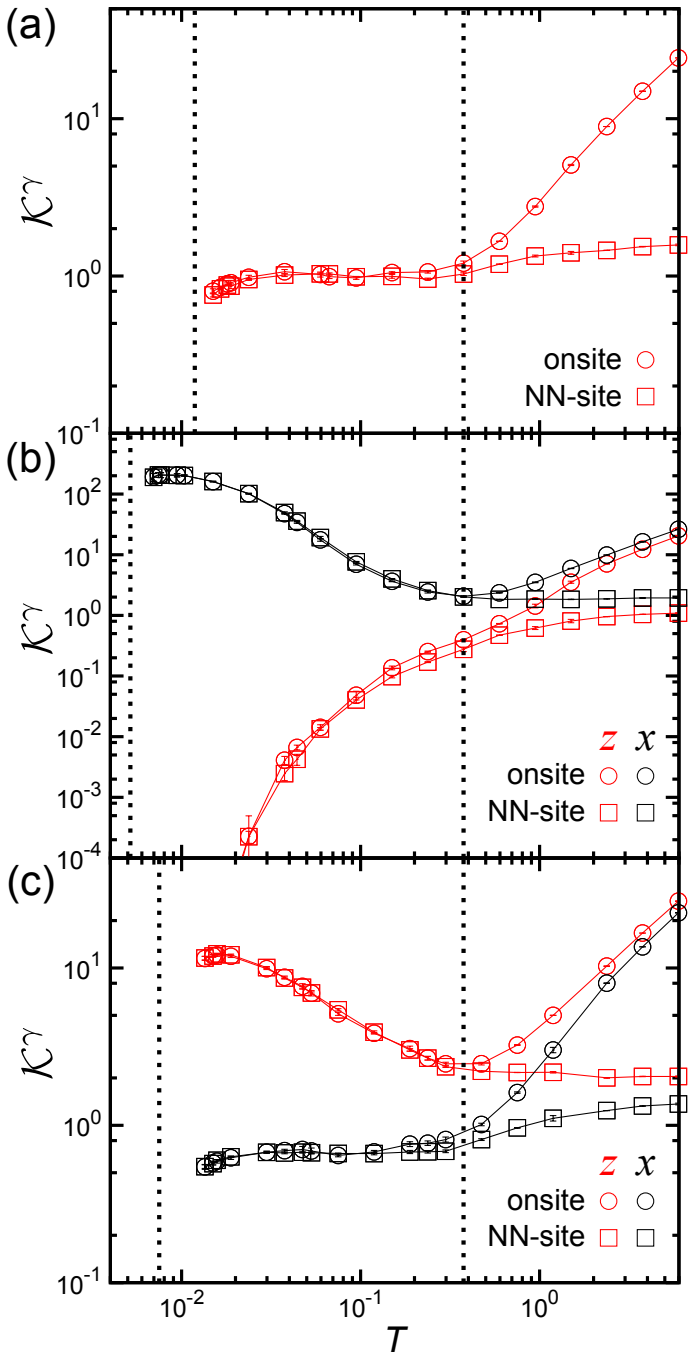

Figure 4.14: T dependences of the Korringa ratio $\mathcal{K}^\gamma = 1/(T_1^\gamma T(\chi^\gamma)^2)$ for the FM case at (a) $\alpha = 1.0$, (b) $\alpha = 0.8$, and (c) $\alpha = 1.2$ ($\gamma = z, x$). Note that $\mathcal{K}^z = \mathcal{K}^x$ for $\alpha = 1.0$ and $\mathcal{K}^x = \mathcal{K}^y$ for all the cases from the symmetry. The vertical dotted lines indicates T_L and T_H for each α.

is also the case for the x component for the FM case with $\alpha = 1.2$, as shown in Fig. 4.14(c). However, the suggestive behavior is presumably superficial, as the results for the AFM cases as well as for $\alpha = 0.8$ behave differently with substantial T

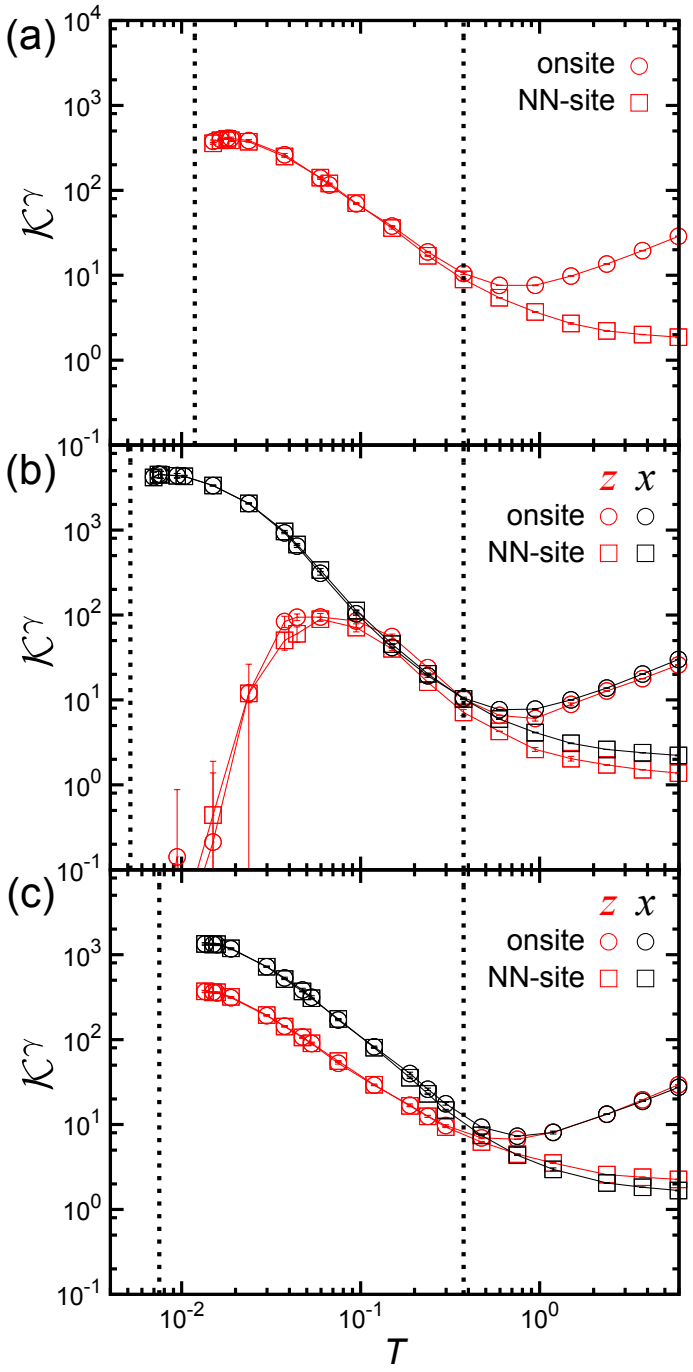

Figure 4.15: T dependences of the Korringa ratio $\mathcal{K}^\gamma = 1/(T_1^\gamma T(\chi^\gamma)^2)$ for the AFM case at (a) $\alpha = 1.0$, (b) $\alpha = 0.8$, and (c) $\alpha = 1.2$ ($\gamma = z, x$). The notations are common to those in Fig. 4.14.

dependence.

4.6 Effect of the Z_2 variables $\{\eta_r\}$ on the dynamical properties

As pointed out in the previous section, a remarkable feature in the Kitaev model is the dichotomy between the dynamical and static spin correlations; namely, the NMR relaxation rate $1/T_1^\gamma$ and the magnetic susceptibility χ^γ, both of which reflect the dynamical spin correlations, show substantial T dependences below $T_{\rm H}$ (Figs. 4.11-4.13), even though the static spin correlations $\langle S_j^\gamma S_{j'}^\gamma \rangle_{\rm NN}$ almost saturate to the $T = 0$ values (Fig. 4.1). The dichotomy is unconventional behavior hardly seen in conventional insulating magnets. This might be a signature of the fractionalization of quantum spins, as $T_{\rm H}$ is the temperature where the fractionalization sets in as indicated in the specific heat and entropy [91].

To examine the dichotomy in more detail, we calculate the T dependences of $\langle S_j^\gamma S_{j'}^\gamma \rangle_{\rm NN}$, $1/T_1^\gamma$, and χ^γ for two extreme cases by assuming the configuration of $\{\eta_r\}$ by hand. One is the flux-free state with all $\eta_r = +1$, which is realized in the ground state. The other is the state with completely random $\{\eta_r\}$, corresponding to the high-T limit. For this purpose, we regard a single z bond r_0 as the cluster in CDMFT, and take $P(\eta_{r_0} = 1) = 1$ and $P(\eta_{r_0} = -1) = 0$ for the former uniform state, while $P(\eta_{r_0} = 1) = P(\eta_{r_0} = -1) = 1/2$ for the latter random state, in Eq. (3.21) of the self-consistent equation of CDMFT [122].

Figure 4.16 shows the results. In all cases for $\alpha = 1.0$, 0.8, and 1.2, $\langle S_j^\gamma S_{j'}^\gamma \rangle_{\rm NN}$ for both uniform and random $\{\eta_r\}$ shows almost similar T dependence to the CDMFT results, as shown in Figs. 4.16(a)-4.16(c). However, $1/T_1^\gamma$ and χ^γ exhibit considerably different T dependence. For instance, in the isotropic case with $\alpha = 1.0$, although $1/T_1$ is almost T independent for $T > T_{\rm H}$ for both uniform and random $\{\eta_r\}$ similar to the result by the CDMFT+CTQMC method shown in Fig. 4.11(a), it shows different behavior below $T_{\rm H}$ between the two cases, as shown in Fig. 4.16(d). For the case with uniform $\{\eta_r\}$, $1/T_1$ decreases to zero after showing a small hump. The suppression at low T reflects the flux gap $\Delta \simeq 0.065J$ in the flux-free state [26, 98] in the ground state. On the other hand, for the case with random $\{\eta_r\}$, $1/T_1$ monotonically increases while decreasing T in the calculated T range. Similar T dependences of $1/T_1^\gamma$ are obtained for $1/T_1^x$ at $\alpha = 0.8$ and $1/T_1^{x,z}$ at $\alpha = 1.2$, as shown in Figs. 4.16(e) and 4.16(f), respectively. We note that $1/T^z$ for $\alpha = 0.8$ behaves differently; we will comment on this point in the end of this section.

Similar behavior is observed in the magnetic susceptibility χ, as shown in Figs. 4.16(g)-4.16(l). In this case, we note that, even for the uniform $\{\eta_r\}$, χ is not strongly suppressed by the spin gap at low T, as the present system does not conserve the z component of total spin. Nonetheless, similar crossover from the random $\{\eta_r\}$ to the uniform $\{\eta_r\}$ is observed while approaching $T_{\rm L}$.

The results clearly indicate that the peculiar T dependences of $1/T_1$ and χ found in the CDMFT+CTQMC results are closely related with fluctuations of the Z_2 variables $\{\eta_r\}$ composed of localized Majorana fermions $\{\bar{c}\}$ emergent from the spin fractionalization. As seen in the equal-time spin correlations shown in Figs. 4.16(a)-4.16(c), itinerant matter fermions develop their kinetic energy to the saturation at

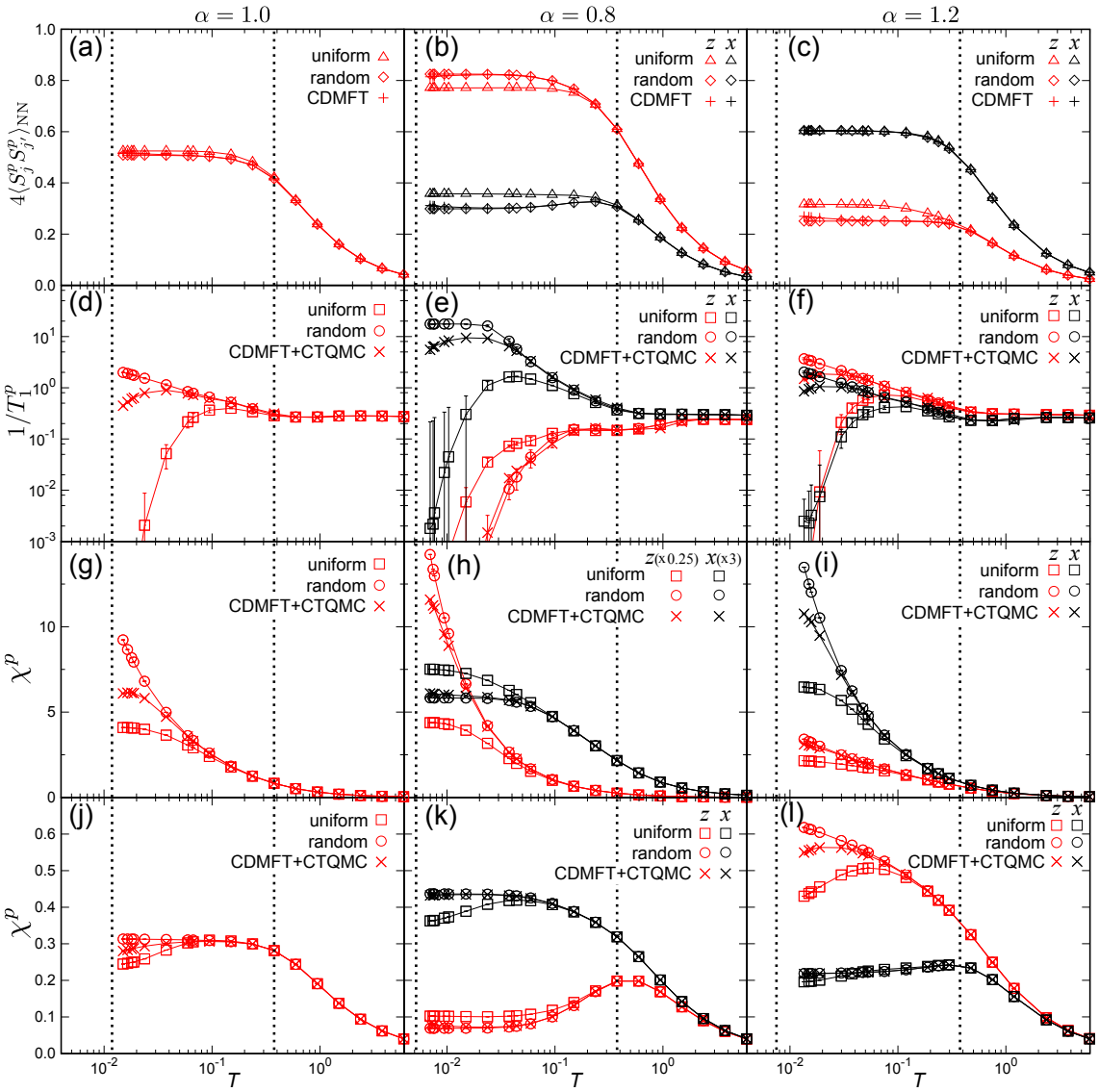

Figure 4.16: (a)(b)(c) $4\langle S_j^\gamma S_{j'}^\gamma\rangle_{\rm NN}$ for the FM case, (d)(e)(f) the onsite components of $1/T_1^\gamma$, and χ^γ for the (g)(h)(i) FM and (j)(k)(l) AFM cases ($\gamma = z, x$) calculated by setting all $\eta_r = 1$ (uniform) and all η_r being random (random) in the CDMFT calculations: (a)(d)(g)(h) $\alpha = 1.0$, (b)(e)(h)(k) $\alpha = 0.8$, and (c)(f)(i)(l) $\alpha = 1.2$. The data in (h) are multiplied by 0.25 and 3 for $\gamma = z$ and x, respectively. For $\alpha = 1.0$, the results are equivalent for $\gamma = x, z$. For comparison, we plot the data in Figs. 4.1 (CDMFT), 4.11 , 4.12, and 4.13 (CDMFT+CTQMC). The vertical dotted lines represent $T_{\rm L}$ and $T_{\rm H}$ for each α.

$T \sim T_{\rm H}$ (the equal-time spin correlations correspond to the kinetic energy of matter fermions). Due to the fractionalization, however, the localized Z_2 variables $\{\eta_r\}$ are still disordered even below $T_{\rm H}$ [91], which results in the similar T dependences of $1/T_1$ and χ to those for the random $\{\eta_r\}$, as indicated in Figs. 4.16(d)-4.16(l). When approaching $T_{\rm L}$, $\{\eta_r\}$ are aligned in a coherent manner [91], and hence, both quan-

tities rapidly crossover to the behavior for the uniform $\{\eta_r\}$. Thus, The crossover occurs well below $T_{\rm H}$ and close to $T_{\rm L}$. Of course, as the original quantum spin is a composite of itinerant matter fermions and localized Majorana fermions, the spin excitation is a composite excitation of the fractional degrees of freedom. Nevertheless, our results indicate that the peculiar T dependences of dynamical quantities, such as $1/T_1$ and χ, are dominated by the emergent Z_2 variables $\{\eta_r\}$ from the fractionalization.

As noted above, $1/T_1^z$ for $\alpha = 0.8$ behaves differently from others: $1/T_1^z$ for the random $\{\eta_r\}$ is smaller than that for the uniform $\{\eta_r\}$ at low T, as shown in Fig. 4.16(e). This is presumably because of the peculiar T dependence of the density of states (DOS) for the itinerant matter fermions at $\alpha = 0.8$. In the gapless QSL region for $0.75 \leq \alpha \leq 1.5$ but close to the gapless-gapful boundary at $\alpha = 0.75$, the DOS opens a gap as $\{\eta_r\}$ are thermally disordered by raising T [91]. Thus, the DOS for matter fermions is gapless for the uniform $\{\eta_r\}$, while gapped for the random $\{\eta_r\}$. As spin excitations by S_j^x and S_j^y are composite excitations of both itinerant matter fermions and localized Z_2 variables $\{\eta_r\}$, the gap in the DOS for matter fermions suppresses $1/T_1^z$ for the random case compared to the uniform one. Since $\{\eta_r\}$ are aligned uniformly below $T_{\rm L}$, we expect that $1/T_1^z$ shows an abrupt increase while decreasing T through $T_{\rm L}$. This indicates that while a rapid change of $1/T_1$ when approaching $T_{\rm L}$ is yielded by the coherent alignment of $\{\eta_r\}$, either increase or decrease of $1/T_1$ at $T_{\rm L}$ may be affected by the itinerant matter fermions. We note that χ^z for $\alpha = 0.8$ in the AFM case also behaves differently, which is presumably by the same mechanism although it is less clear since χ does not reflect the spin gap directly as mentioned above.

Finally, let us discuss the crossover behavior from the viewpoint of spatial correlations for the Z_2 variables $\{\eta_r\}$. Figure 4.17 shows the T dependences of the correlation functions $\langle \eta_r \eta_{r'} \rangle$. We plot the data for different distances $|r - r'|$ in the horizontal direction [see the inset of Fig. 4.17(a)]. Note that all $\langle \eta_r \eta_{r'} \rangle$ vanish for different rows above the artificial phase transition temperature $\tilde{T}_{\rm c}$. We find that the lateral correlations develop below $T_{\rm H}$, which accounts for the deviations of $1/T_1$ and χ from those calculated for the random $\{\eta_r\}$. In particular, we observe that the development of the correlations for $|r - r'| = 2$ appears to well coincide with the deviations. The reason is as follows. When S_j^z is operated at a site j on a z bond r_0, two Z_2 fluxes W_h and $W_{h'}$ are flipped on the hexagons sharing η_{r_0}. Hence, such an operation affects two η_r defined on the other side z bonds of W_h and $W_{h'}$ [see the inset of Fig. 4.17(a)]. Thus, the correlations $\langle \eta_r \eta_{r'} \rangle$ with $|r - r'| = 2$ are likely to play a dominant role in the spin dynamics.

We note that the spatial correlations of $\{\eta_r\}$ decays quickly as a function of the distance in the T range discussed in the present calculations, as shown in Fig. 4.17. This supports the validity of the cluster approximation in the CDMFT. Indeed, the convergence with respect to the cluster size (width) is sufficiently quick: the clusters with the width of 4 are enough to guarantee the precisions that we need as shown in Sec. 4.1.2.

4.7 Summary of this chapter

In this chapter, we have presented numerical results for spin dynamics of the Kitaev model with and without the anisotropy in the bond-dependent coupling constants. We calculated the experimentally-measurable quantities, the dynamical spin structure factor $S(\mathbf{q},\omega)$, the NMR relaxation rate $1/T_1$, and the magnetic susceptibility χ, in the wide T range including the peculiar paramagnetic region where quantum spins are fractionalized. We also confirmed the Majorana CDMFT is precise enough in the range of T and anisotropy that we investigated in the present study.

We found that the Kitaev model exhibits unconventional behaviors in spin dynamics in the finite-T paramagnetic state in proximity to the QSL ground state. The prominent feature is the dichotomy between static and dynamical spin correlations as a consequence of the spin fractionalization. The dichotomy appears clearly in the increase of $1/T_1$ below $T_{\rm H}$ where the fractionalization sets in, despite the saturation of static correlations. Our results suggest that the dichotomy is found universally in the fractionalized paramagnetic region irrespective of the anisotropy in the system.

On the other hand, we also clarified interesting behaviors that depend on the anisotropy at low T. When one of the three bond-dependent interactions is stronger than the other two, the spin dynamics shows peculiar T and energy dependences distinct from those in the isotropic coupling case as follows. As lowering T, $S(\mathbf{q},\omega)$ develops a δ-function like peak, which is well separated from the incoherent continuum. $1/T_1$ monotonically decreases in the spin component for the stronger bond. χ increases and saturates to a nonzero value for the spin component for the weaker bonds, while it shows hump and then decreases for the stronger-bond component in the antiferromagnetic case. We also showed that the peculiar T dependences of χ are qualitatively explained by the two-site dimer model. In contrast, when the anisotropy is opposite, i.e., when the two types of bonds become stronger, the results are qualitatively unchanged from those for the isotropic case, while the effect of anisotropy is obvious in the $\mathbf{q}$ dependence in $S(\mathbf{q},\omega)$ and the different components in $1/T_1$ and χ.

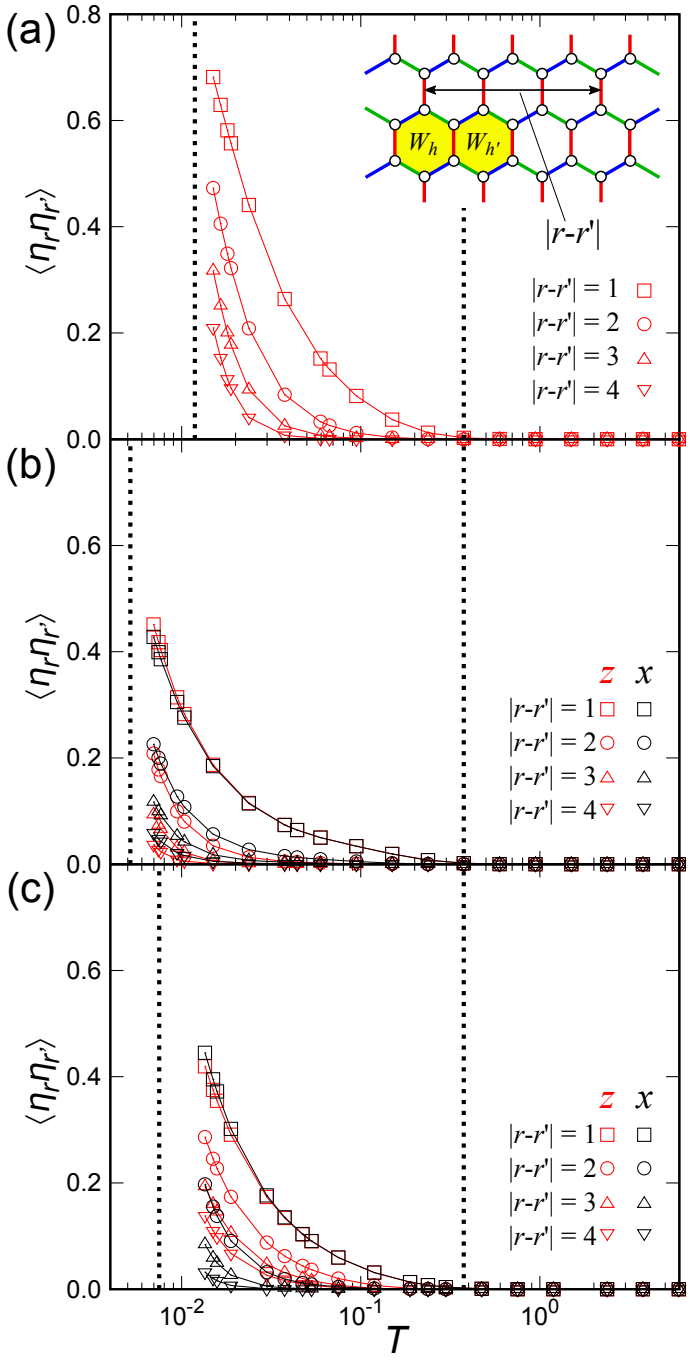

Figure 4.17: Correlation functions between the Z_2 variables η_r on different z bonds: (a) $\alpha = 1.0$, (b) 0.8, and (c) 1.2. The correlations are measured for η_r and $\eta_{r'}$ which are sandwiched by the common two xy chains; $|r - r'|$ is the distance in the unit of the width of the hexagon [see the inset in (a) for the example of $|r - r'| = 3$]. The yellow hexagons represent two neighboring fluxes which are flipped by an operation of S^z_j on the sharing z bond; see the text for the details. The vertical dotted lines represent $T_{\rm L}$ and $T_{\rm H}$ for each α.

5
Results by QMC + CTQMC method

In Chap. 4, we have investigated the behavior of the dynamical properties for the Kitaev model on 2D honeycomb structure. Despite the successful calculations of dynamical quantities, the applicable T range of the CDMFT+CTQMC method is limited. This is due to the occurrence of phase transition at $T \sim T_{\mathrm{L}}$ as an artifact of the mean-field approximation in the CDMFT. Moreover, the CDMFT+CTQMC method is not suitable for the Kitaev model on 3D lattice structures by the following reasons. One is that a larger cluster is necessary in the CDMFT, as the unit cell, or more strictly speaking, the smallest loop of lattice sites, for which the conserved Z_2 flux is defined, becomes larger for 3D than 2D in general. Another reason is that the 3D extensions of the Kitaev model may cause a phase transition, which might be hard to capture by the CDMFT. For instance, the Kitaev model on a 3D hyperhoneycomb structure exhibits an unconventional phase transition triggered by proliferation of loops composed of thermally excited Z_2 fluxes [31, 90]. The cluster approximation in the CDMFT is not suitable to describe such a topological transition characterized by global quantities beyond the cluster. An alternative method is desired to study the spin dynamics, including the low-T behavior.

Besides such a theoretical demand, it is crucial to clarify the spin dynamics of the Kitaev model in the whole T range also from the experimental point of view. As introduced in Chap. 1, many candidates have been explored recently in both quasi-2D and 3D materials [55,56,67,86,87]. Some indications of the fractionalization were observed, for instance, in the specific heat [92], magnetic Raman scattering [95,104], inelastic neutron scattering [74, 96, 99], and thermal transport [78, 123]. However, such indications are for rather high-T features, corresponding to the theoretical predictions around and below T_{H} associated with itinerant matter fermions [91, 97, 120, 124, 125]. It is highly desired to experimentally capture another indications dominated by thermally excited Z_2 fluxes at lower T. Although all the candidate materials exhibit a magnetic order at low T, several efforts have been made for suppressing the order, e.g., by external pressure [86,126], magnetic field [79,82,127], and chemical substitution [128]. Given such an upsurge of interest, it is highly important to clarify the dynamical behavior of the 2D and 3D Kitaev models down to the lowest T.

In this chapter, we present the results obtained by the QMC+CTQMC method, in order to fulfill such a requirement. This QMC+CTQMC method is fully unbiased and enables us to investigate the low-temperature spin dynamics dominated by thermally excited Z_2 fluxes, including the unconventional phase transition caused by Z_2 flux loops in three dimensions, which was unreachable by the CDMFT+CTQMC methods. We apply this technique to the Kitaev model in both two and three

dimensions. We presents the results for the isotropic case with $J_x = J_y = J_z = J = \pm 1.0$; $J = +1$ corresponds to the FM case, while $J = -1$ corresponds to the AFM case.

In Sec. 5.1, we present the results for the 2D honeycomb case. By comparing the data of χ, $1/T_1$, and $S(\mathbf{q}, \omega)$ by the CDMFT+CTQMC and QMC+CTQMC methods, we show that although the former works quite well above the fictitious critical temperature, only the latter can give reasonable results at lower T. In Sec. 5.2, we present the results for 3D hyperhoneycomb case. We present the QMC+CTQMC results for χ and $1/T_1$ in Sec. 5.2.1, and $S(\mathbf{q}, \omega)$ in Sec. 5.2.2. From the comparison between the 2D and 3D results, we clarify the signatures arising from the difference of the system dimension. While everything changes smoothly through the crossover at $T = T_{\mathrm{L}}$ in the 2D honeycomb case, the dynamical quantities exhibit singular behaviors in the 3D hyperhoneycomb case at the phase transition caused by the topological nature of excited Z_2 flux loops. Thus, the QMC+CTQMC is applicable to the unconventional phase transition in 3D, which is not accessible by the CDMFT+CTQMC method. Our results show that the dynamical properties at low T depend substantially on the system dimension, despite almost dimension-independent behavior of the static spin correlations. This is the low-T aspect of the dichotomy between static and dynamical spin correlations, which was found in the intermediate T region presented in Chap. 4. Section 5.4 is devoted to the summary of this chapter.

5.1 Results for 2D honeycomb structure

5.1.1 Magnetic susceptibility and NMR relaxation rate

Figure 5.1 displays the QMC+CTQMC results for the magnetic susceptibility χ and the NMR relaxation rate $1/T_1$. χ is calculated from the imaginary-time spin correlations as shown in Eq. (3.53).

As shown in Figs. 5.1(a) and 5.1(b), the results for different system sizes $L = 12$ and 20 agree with each other ($N = 2L^2$), indicating that the QMC+CTQMC results well converge with respect to the system size. In the figures, the CDMFT+CTQMC results in Figs. 4.11(a), 4.12(a), and 4.13(a) are also plotted by gray symbols for comparison. In the CDMFT+CTQMC method, as mentioned above, the cluster mean-field approximation leads to a fictitious phase transition at $\tilde{T}_{\mathrm{c}} \simeq 0.014$, and hence, we plot the data above $\tilde{T}_{\mathrm{c}}$. We find that the QMC+CTQMC results well agree with the CDMFT+CTQMC ones for $T \gtrsim \tilde{T}_{\mathrm{c}}$, which supports the validity of the latter for $T \gtrsim \tilde{T}_{\mathrm{c}}$. While such validity was shown for the static quantities in Sec. 4.1.1, the present results demonstrate it explicitly for the dynamical quantities. The present QMC+CTQMC method enables us to study the low-T region around and below the low-T crossover temperature $T_{\mathrm{L}} \simeq 0.012$, beyond $\tilde{T}_{\mathrm{c}}$ in the CDMFT+CTQMC result. T_{L} is the temperature where the localized Z_2 fluxes W_p begin to be frozen into the flux-free state while decreasing T [91]. Thus, our results show how the dynamical properties are affected by thermally excited Z_2 fluxes. Figure 5.1(a) indicates that, while decreasing T around T_{L}, χ decreases slightly and

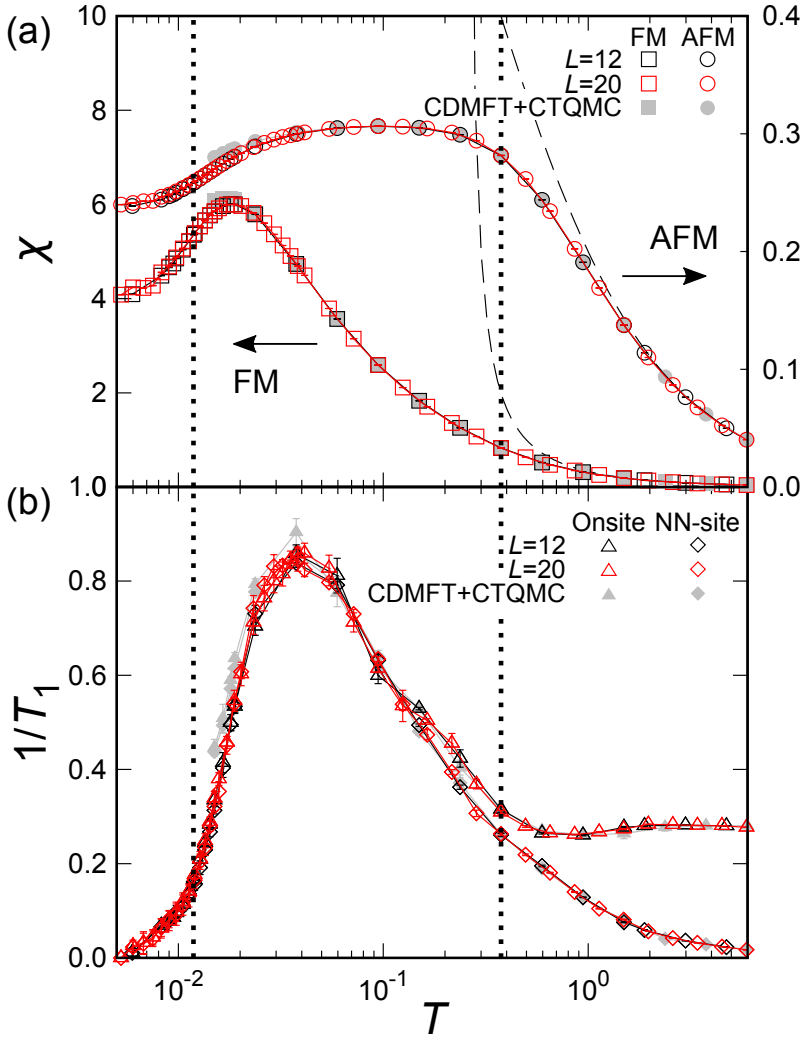

Figure 5.1: QMC+CTQMC results for the 2D honeycomb Kitaev model with isotropic J_γ: (a) the magnetic susceptibility χ and (b) the NMR relaxation rate $1/T_1$. In (a), FM and AFM denote the ferromagnetic case with $J_\gamma = J = 1$ and the antiferromagnetic case with $J_\gamma = J = -1$, respectively. While the onsite component of $1/T_1$ is common to the FM and AFM cases, the NN-site component for the AFM case is obtained by changing the sign of the FM data plotted in (b). For comparison, we plot the CDMFT+CTQMC results in Figs. 4.11(a), 4.12(a), and 4.13(a) by gray symbols. The vertical dotted lines indicate $T_{\rm L} \simeq 0.012$ and $T_{\rm H} \simeq 0.375$ (see Ref. [91]). In (a), the dashed curves represent the Curie-Weiss behaviors, $\chi_{\rm CW} = 1/(4T - J)$.

changes the curvature from upward to downward convex, for both the FM and AFM cases. While further decreasing T, χ appears to converge to a nonzero value, as expected for the system which does not conserve the z component of total spin. The asymptotic value is almost one order of magnitude larger for the FM case than the AFM case. On the other hand, as shown in Fig. 5.1(b), $1/T_1$ decreases below the peak slightly above $T_{\rm L}$ as partly seen in the CDMFT+CTQMC results [120], and continues to decrease around $T_{\rm L}$ reaching to almost zero below $T \sim 0.005$. The low-T suppression is due to a nonzero flux gap required to excite the Z_2 fluxes from the flux-free ground state [26], and the decay is expected to be exponential.

We also compute the T derivatives of χ and $1/T_1$, as shown in Figs. 5.2(a) and 5.2(b), respectively. Both derivatives show a peak around $T_{\rm L}$, but change smoothly without showing any singularity. For comparison, we also compute the thermal fluctuation of Z_2 fluxes W_p by the QMC method, defined by

$$\Delta W_p = \frac{1}{N_p T^2}\Big(\langle (\sum_p W_p)^2\rangle - \langle \sum_p W_p\rangle^2\Big), \tag{5.1}$$

where N_p is the number of plaquettes in the system. Note that ΔW_p corresponds to the specific heat in the anisotropic limit (toric code), where the effective Hamiltonian is given in the form $\mathcal{H} \propto \sum_p W_p$ [26]; hence, ΔW_p measures the energy fluctuation related to the Z_2 fluxes. As shown in Fig. 5.2(c), ΔW_p also shows a broad peak around $T_{\rm L}$, similar to the T derivatives of χ and $1/T_1$. All these smooth changes with broad peaks are consistent with the fact that $T_{\rm L}$ is not a phase transition but just a crossover in the 2D case [91]. Furthermore, the similar behavior between three quantities in Fig. 5.2 suggests that the T derivatives of χ and $1/T_1$ provide good probes for the fluctuations of Z_2 fluxes. Interestingly, $d\chi/dT$ behaves differently between the FM and AFM cases, as shown in Fig. 5.2(a): it is negative for $T_{\rm L} \lesssim T \lesssim T_{\rm H}$ and changes the sign to positive just above $T_{\rm L}$ for the FM case, while mostly positive in the same T range for the AFM case. The qualitative difference will be useful for identifying the sign of the dominant Kitaev interactions in candidate materials.

5.1.2 Dynamical spin structure factor

The dynamical spin structure factor $S(\mathbf{q},\omega)$ defined by Eq. (3.44) obtained by the QMC+CTQMC method for the 2D case are shown in Figs. 5.3(a), 5.3(c), 5.3(e), 5.3(g), and 5.3(i) for the FM case and in Figs. 5.3(b), 5.3(d), 5.3(f), 5.3(h), and 5.3(j) for FM case. The corresponding results by the CDMFT+CTQMC method above $T_{\rm H}$ are shown in Figs. 4.4(a), 4.4(d), 4.4(g), and 4.4(j) for the FM case and Figs. 4.5(a), 4.5(d), 4.5(g), and 4.5(j) for the AFM case, for the slightly different T set. As confirmed for χ and $1/T_1$ in Sec. 5.1.1, the CDMFT+CTQMC results of $S(\mathbf{q},\omega)$ above $T_{\rm L}$ also agrees well with QMC+CTQMC results (see Fig. 5.4). $S(\mathbf{q},\omega)$ below $T_{\rm L}$, shown in Figs. 5.3(a) and 5.3(b), does not change much at large ω region ($\omega \gtrsim 0.5$) compared with $S(\mathbf{q},\omega)$ just above $T_{\rm L}$, shown in Figs. 5.3(c) and 5.3(d). On the other hand the peak around $\omega \simeq 0$ becomes shaper and gap opens as shown in Figs. 5.1(a) and 5.1(b), corresponding to the decay of $1/T_1$ below $T_{\rm L}$.

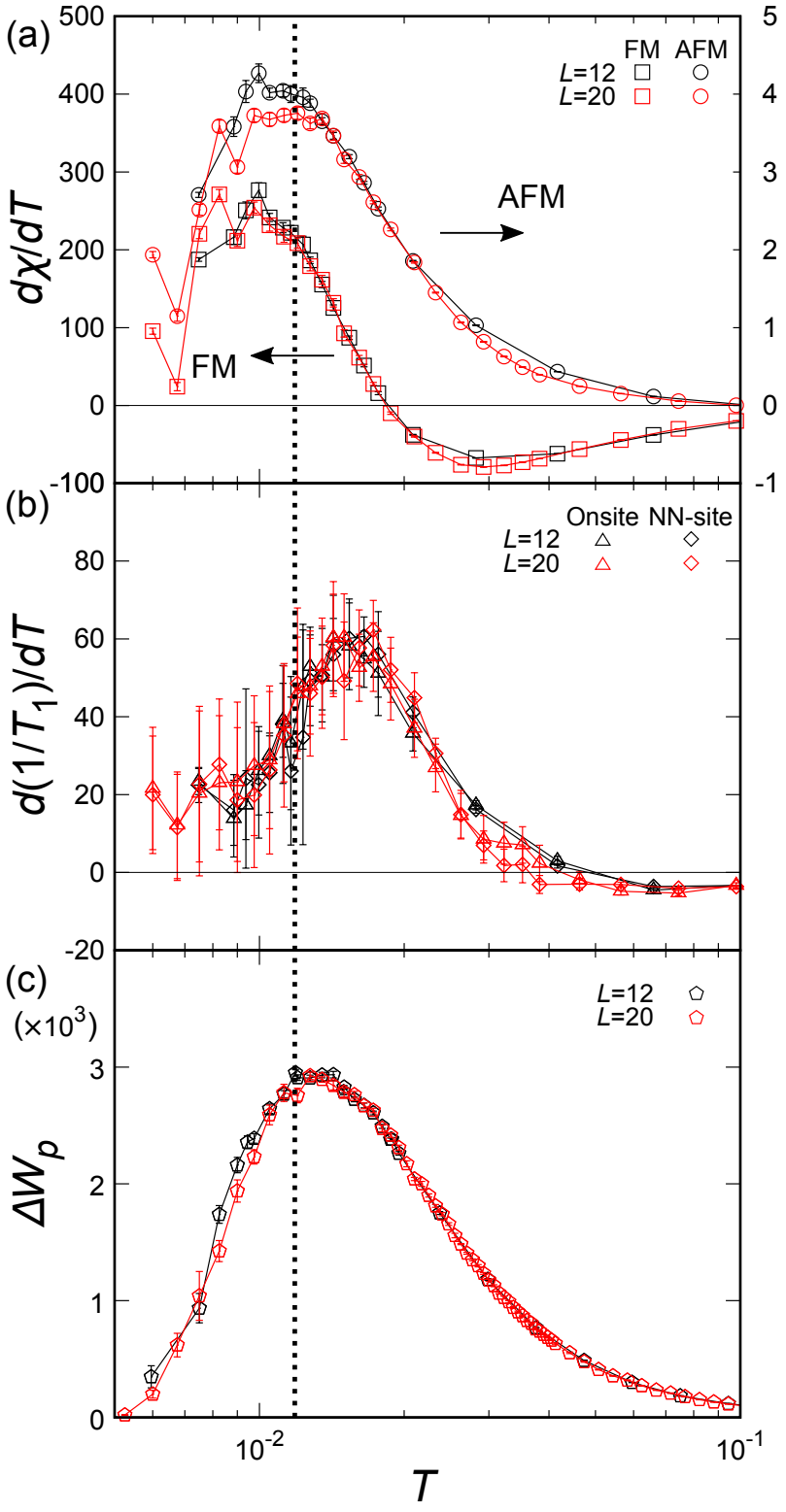

Figure 5.2: (a) and (b) T derivatives of the data in Fig. 5.1. (c) plots the thermal fluctuation of Z_2 fluxes W_p, ΔW_p in Eq. (5.1). The vertical dotted line indicates $T_{\rm L}$.

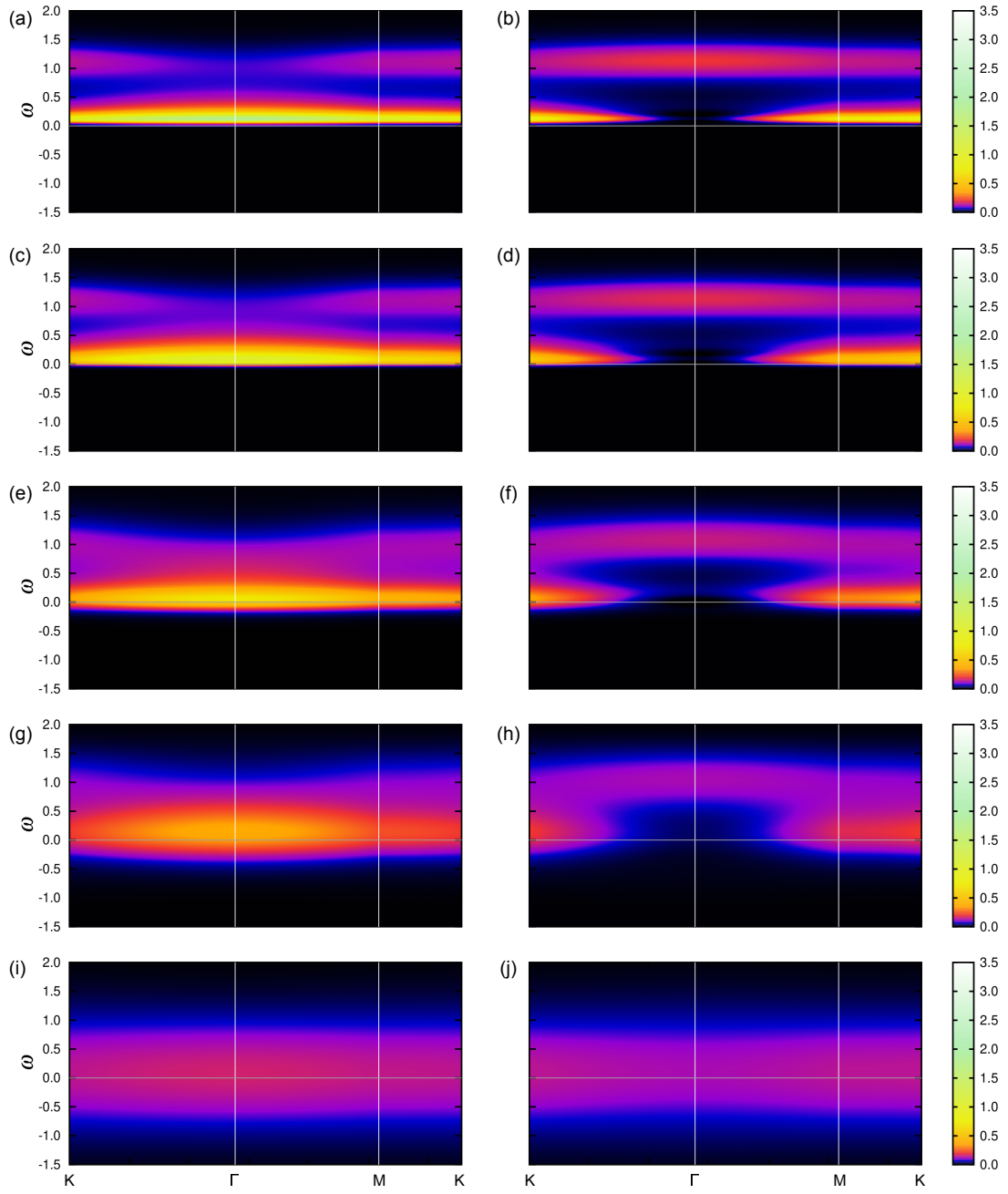

Figure 5.3: QMC+CTQMC results of the dynamical spin structure factor for the 2D honeycomb Kitaev model with isotropic J_γ. The data are calculated for $L = 20$ (800 sites) and plotted along the symmetric lines indicated in Fig. 3.3(a). (a)(c)(e)(g)(i) are for the FM case and (b)(d)(f)(h)(j) are for the AFM case: (a)(b) $T = 0.009$, (c)(d) $T = 0.01725$, (e)(f) $T = 0.09441$, (g)(h) $T = 0.28476$, and (i)(j) $T = 2.590575$. Note that $T_{\mathrm{L}} \simeq 0.012$ and $T_{\mathrm{H}} \simeq 0.375$ [91].

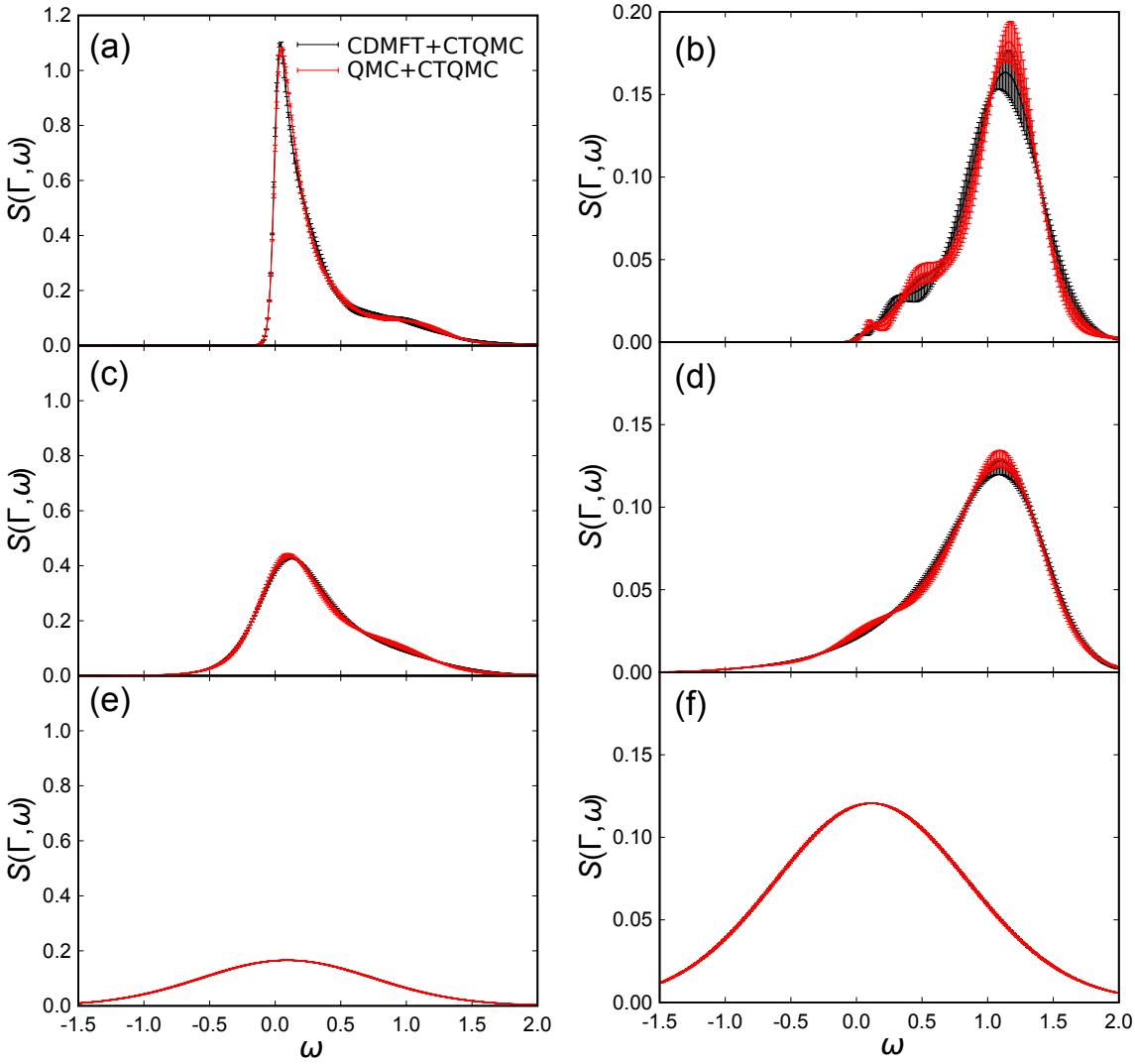

Figure 5.4: Comparison between CDMFT+CTQMC and QMC+CTQMC results of the dynamical spin structure factor at Γ point $S(\mathbf{q}, \Gamma)$ for the 2D honeycomb Kitaev model with isotropic J_γ. The data are calculated for $L = 12$ (288 sites) for QMC+CTQMC results. (a)(c)(e) are for the FM case and (b)(d)(f) are for the AFM case: (a)(b) $T \simeq 0.0237$, (c)(d) $T \simeq 0.237$, (e)(f) $T \simeq 2.37$.

5.2 Results for 3D hyperhoneycomb structure

5.2.1 Magnetic susceptibility and NMR relaxation rate

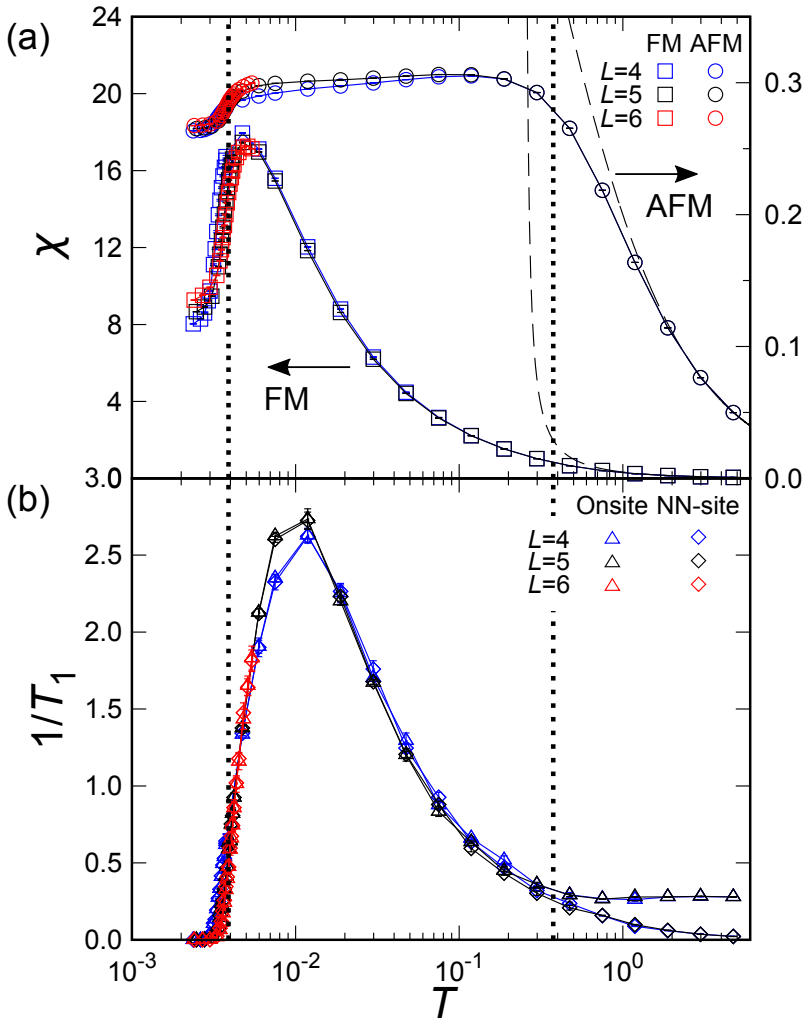

Figure 5.5: QMC+CTQMC results for the 3D hyperhoneycomb Kitaev model with isotropic J_γ: (a) the magnetic susceptibility χ and (b) the NMR relaxation rate $1/T_1$. The vertical dotted lines indicate $T_c \simeq 0.014$ and $T_H \simeq 0.375$ [90]. Other notations are the same as those in Fig. 5.1.

Figure 5.5 shows the QMC+CTQMC results of χ and $1/T_1$ obtained for the Kitaev model on the 3D hyperhoneycomb structure, shown in Fig. 3.2. The system size is given by $N = 4L^3$: 256, 500, and 864 sites for $L = 4$, 5, and 6, respectively. Note that in the hyperhoneycomb structure the z bond is not equivalent to the x and y bonds from the lattice structure symmetry; we compute χ by Eq. (3.53) and $1/T_1$ by Eqs. (3.49)-(3.52) with replacing $\langle S_j^\gamma(\tau) S_{j'}^\gamma \rangle$ ($\gamma = x, y$) by $\langle S_j^z(\tau) S_{j'}^z \rangle$ for simplicity. The overall T dependence is similar to the 2D results as follows. The high-T behaviors above T_H are almost unchanged from the 2D cases, presumably

because the bandwidth of matter fermions is independent of the dimensionality. With a decrease of T, χ begins to deviate from the Curie-Weiss behavior below $T \sim T_{\rm H}$ and converges to a nonzero value after showing a peak, while $1/T_1$ increases below $T_{\rm H}$ and strongly suppressed due to the flux gap after showing a peak at a low T. Nonetheless, there are quantitative differences. For instance, the peak of χ for the FM case is more than twice larger that that for the 2D case. Simultaneously, the change at low T is much steeper in 3D than 2D. Similar behaviors are also seen in $1/T_1$. We will briefly comment on the quantitative differences in Sec. 5.3

However, we also find a qualitative difference between 3D and 2D in the low-T behavior. The 3D hyperhoneycomb model exhibits a phase transition at $T_{\rm c} \simeq 0.0039$ [90]. The phase transition takes place between the high-T paramagnet and the low-T QSL, driven by the proliferation of loops composed of the localized Z_2 fluxes W_p. Thus, the transition is of topological nature, not characterized by local spin operators contrary to conventional magnetic ordering [90]. Nevertheless, we find singular behaviors in both χ and $1/T_1$, as more clearly seen in the T derivatives shown in Figs. 5.6(a) and 5.6(b). Both T derivatives show a sharp peak at $T \simeq T_{\rm c}$, which becomes sharper for larger system sizes. We also plot the thermal fluctuation of Z_2 fluxes ΔW_p in Eq. (5.1) in Fig. 5.6(c). In this 3D case, ΔW_p shows a similar sharp peak to $d\chi/dT$ and $d(1/T_1)/dT$. All these behaviors are in stark contrast to the 2D case, where the crossover at $T_{\rm L}$ leads to smooth T dependence as shown in Fig. 5.2. The low-T behaviors of the dynamical quantities are substantially different from those in 2D, not only in the critical behavior associated with the phase transition but also the larger T dependence. This clear difference depending on the spatial dimension is rather surprising when considering that the static spin correlations are not much different between 2D and 3D in the whole T range [90, 91]. In Chap. 4, we have unveiled a prominent feature of the Kitaev QSL, the dichotomy between static and dynamical spin correlations, from the T dependence of the static spin correlations for NN sites and $1/T_1$. The significant dimensional dependence at low T found here is another aspect of the dichotomy. We note that the difference of the sign of $d\chi/dT$ between the FM and AFM cases for $T_{\rm c} \lesssim T \lesssim T_{\rm H}$ is also seen in the 3D case, as shown in Fig. 5.2(c). We also note that the behavior of $d\chi/dT$ is similar to that found in the effective model in the anisotropic limit $J_z \gg J_x, J_y$ [90].

5.2.2 Dynamical spin structure factor

The QMC+CTQMC results for the dynamical spin structure factor $S(\mathbf{q}, \omega)$ for the 3D case are shown in Fig. 5.7. $S(\mathbf{q}, \omega)$ is defined as

$$S(\mathbf{q}, \omega) = \frac{1}{N} \sum_{j,j'} e^{i\mathbf{q}\cdot(\mathbf{r}_j - \mathbf{r}_{j'})} S^z_{j,j'}(\omega), \tag{5.2}$$

where $\mathbf{r}_j$ represents the position vector for site j. As noted above, we set $S^\gamma_{j,j'}(\omega) = S^z_{j,j'}(\omega)$ for $\gamma = x, y$. The results are plotted along the symmetric lines in the first Brillouin zone shown in Fig. 3.3(b). The overall T and ω dependence is similar to the 2D case presented in Secs. 4.2 and 5.1.2: almost $\mathbf{q}$-independent incoherent

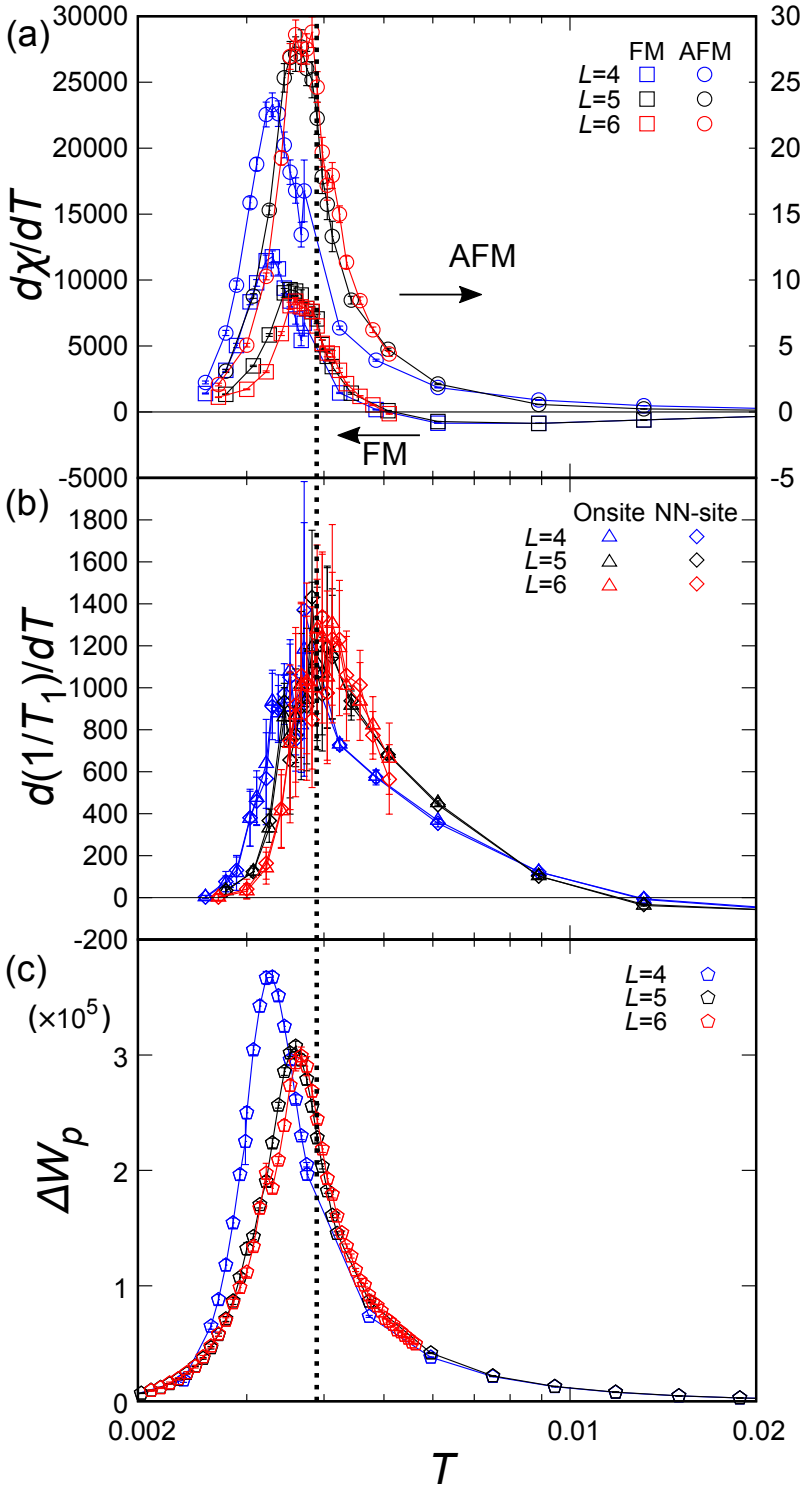

Figure 5.6: (a) and (b) T derivatives of the data in Fig. 5.5. (c) plots the thermal fluctuation of Z_2 fluxes W_p, ΔW_p in Eq. (5.1). The vertical dotted line indicates T_c.

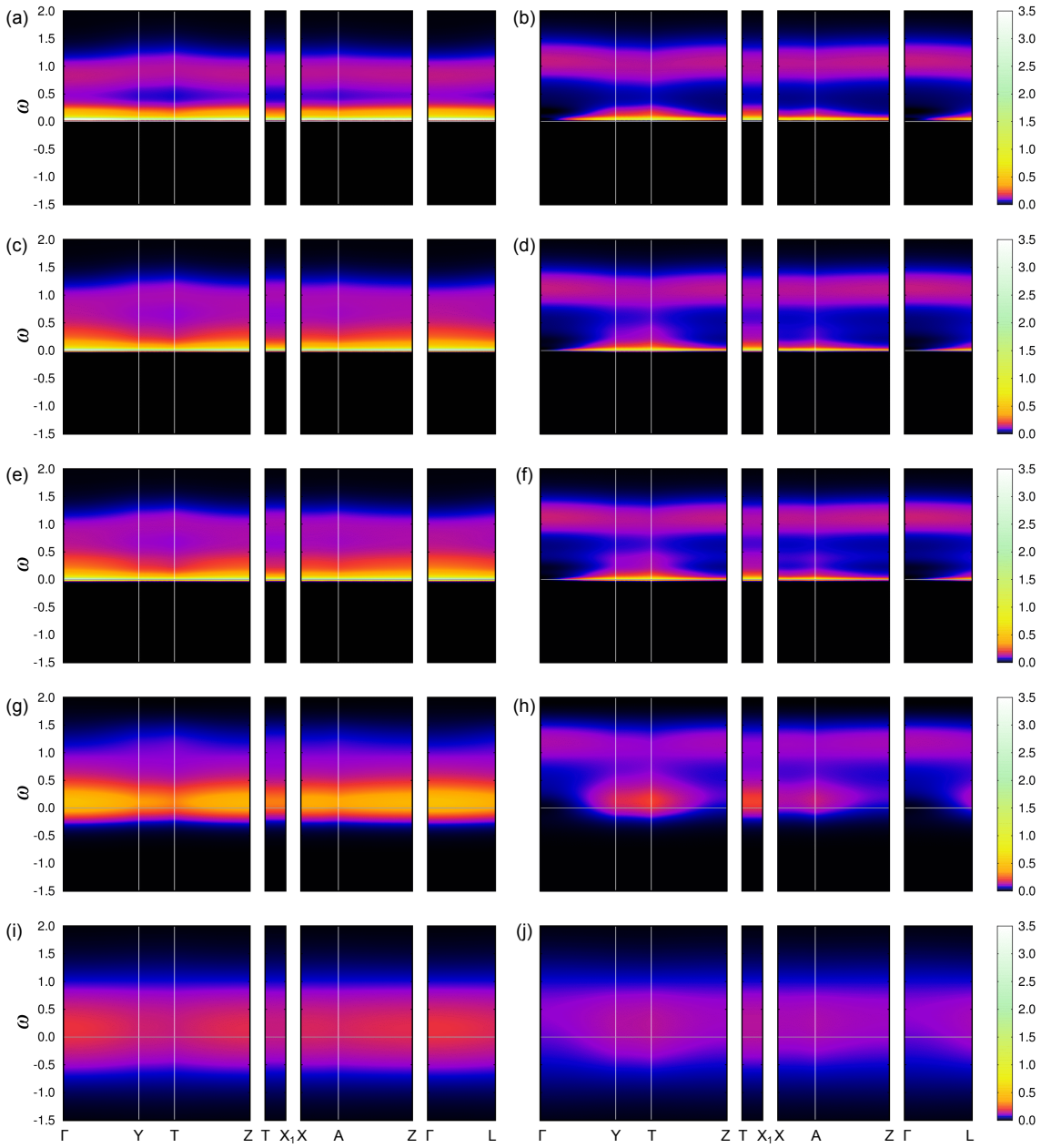

Figure 5.7: QMC+CTQMC results of the dynamical spin structure factor for the 3D hyperhoneycomb Kitaev model with isotropic J_γ. The data are calculated for $L = 5$ (500 sites) and plotted along the symmetric lines indicated in Fig. 3.3(b). (a)(c)(e)(g)(i) are for the FM case and (b)(d)(f)(h)(j) are for the AFM case: (a)(b) $T = 0.002475$, (c)(d) $T = 0.005955$, (e)(f) $T = 0.01185$, (g)(h) $T = 0.18825$, and (i)(j) $T = 1.185$. Note that $T_c \simeq 0.0039$ and $T_H \simeq 0.375$ [90].

response around $\omega = 0$ for $T \gtrsim T_{\rm H}$, growth of the incoherent spectra around $\omega = |J|$ below $T_{\rm H}$, and a rapid increase of the quasi-elastic response while approaching $T_{\rm c}$. Also, as in the 2D case, the difference in the sign of J appears in the $\mathbf{q}$ dependence of the spectral intensity. We note that the lowest-T data below $T_{\rm c}$ in Fig. 5.5(a) agree well with the previous $T = 0$ result [129].

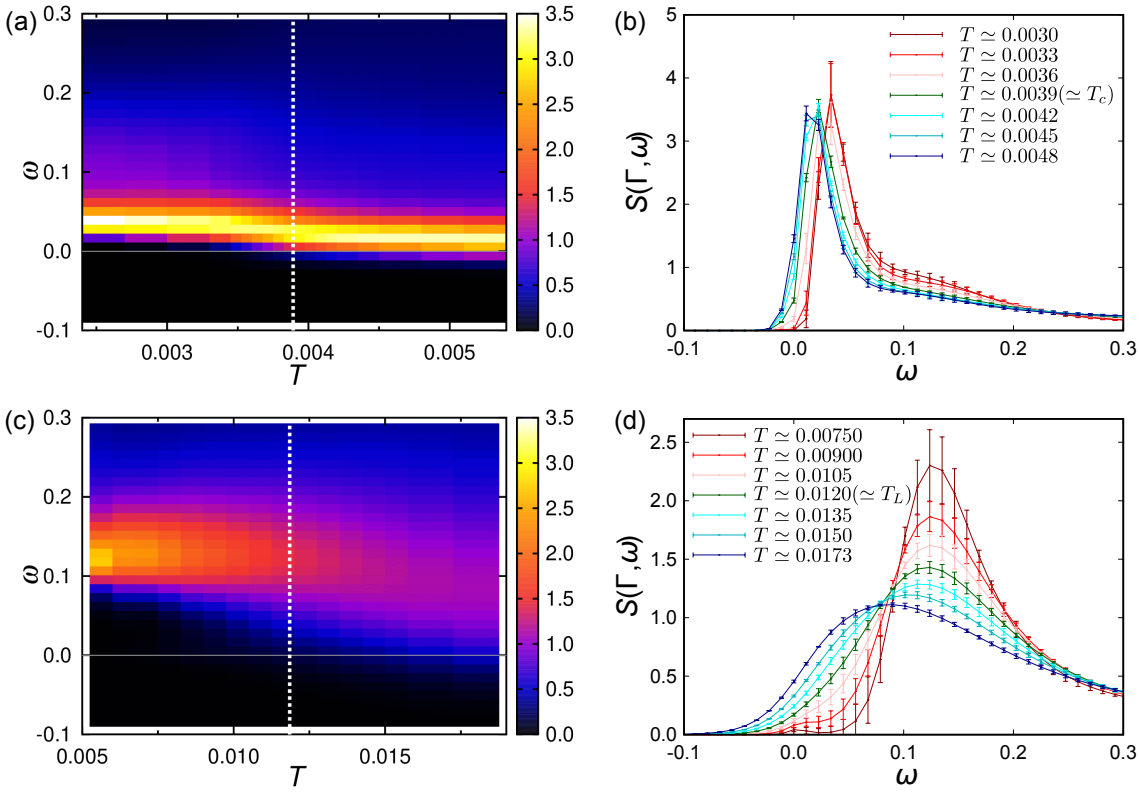

Figure 5.8: Comparison of the low-ω behaviors of $S(\Gamma, \omega) = S(\mathbf{q} = 0, \omega)$ between the 3D and 2D cases at low T. (a) Contour plot of $S(\Gamma, \omega)$ around $T_{\rm c}$ for the 3D case and (b) the ω profiles. (c) and (d) display the corresponding 2D results around $T_{\rm L}$. The data for the 3D and 2D cases are calculated for $L = 6$ (864 sites) and $L = 20$ (800 sites), respectively. The white dotted lines in (a) and (c) indicate $T_{\rm c}$ and $T_{\rm L}$, respectively.

5.3 Comparison between 2D and 3D results

In this section, we compare the results in 2D and 3D case with attention to behavior of dynamical quantities, $S(\mathbf{q}, \omega)$ and $1/T_1$, around $T_{\rm L}$ in 2D case and $T_{\rm c}$ in 3D case.

Figures 5.8(a) and 5.8(b) display the low-ω part of $S(\Gamma, \omega) = S(\mathbf{q} = 0, \omega)$ around $T_{\rm c}$ for the FM case on the 3D hyperhoneycomb structure. Qualitatively similar behaviors are also seen for $S(\mathbf{q}, \omega)$ near the zone boundary for the AFM case. With

a decrease of T across T_c, the quasi-elastic peak near $\omega = 0$ shifts to a slightly higher ω, leading to the opening of the flux gap below T_c. The peak height is almost unchanged across T_c. The corresponding data for the 2D honeycomb case around T_L are shown in Figs. 5.8(c) and 5.8(d). In the 2D case, the peak above T_L is much broader with a lower peak height compared to the 3D case. When lowering T across T_L, the peak becomes sharper with a shift of the peak position to a higher ω. These differences between 2D and 3D are closely related with the quantitatively different behaviors of χ and $1/T_1$ observed in Figs. 5.1 and 5.5 as follows. The sharper peak of $S(\Gamma, \omega)$ near $\omega = 0$ already existing above T_c in 3D corresponds to much larger values of χ and $1/T_1$ just above T_c compared to the 2D results above T_L. Furthermore, the shift of the peak across T_c in Fig. 5.8(b) is related with the steep changes of χ and $1/T_1$ around T_c.

5.4 Summary of this chapter

In this chapter, we have studied the spin dynamics of the Kitaev models by combining the QMC and CTQMC methods. The QMC+CTQMC method overcomes the shortcoming in the CDMFT+CTQMC method, and enables us to investigate the very low-T region where the Z_2 fluxes play a role. The experimental observation of the Z_2 fluxes is one of the open issues in the Kitaev-type QSLs, and hence, the theoretical results obtained by the QMC+CTQMC method provide the references for the experiments in candidate materials.

We have applied the QMC+CTQMC method to the 2D and 3D Kitaev models. Calculating the magnetic susceptibility, the NMR relaxation rate, and the dynamical spin structure factor, we discussed the influences of thermally fluctuating Z_2 fluxes, with focusing on the differences arising from the spatial dimensions. In the 2D honeycomb case, everything changes smoothly while lowering T, reflecting the crossover associated with particlelike Z_2 flux excitations. In contrast, in the 3D hyperhoneycomb case, the system exhibits a phase transition by the proliferation of looplike Z_2 flux excitations, which leads to singular behaviors in the dynamical properties. We found that the dichotomy between static and dynamical spin correlations, which begins below the high-T crossover associated with itinerant matter fermions, persists down to the low-T region, in a more peculiar form reflecting thermally excited Z_2 fluxes; while the dichotomy in the higher-T region is rather universal independent of the spatial dimension, the low-T one appears differently between 2D and 3D, reflecting the different nature of the localized Z_2 flux excitations. We showed that the T derivatives of the magnetic susceptibility and the NMR relaxation rate provide good probes for fluctuating Z_2 fluxes in both 2D and 3D.

6
Discussion

In this chapter, we discuss our theoretical results obtained in the previous chapters in comparison with other theoretical results for the Kitaev model in Sec. 6.1 and with experimental results for the Kitaev candidate materials in Sec. 6.2. In Sec. 6.1.1, we compare our results with those for the classical version of the Kitaev model, and discuss the common and distinct dynamical features between the quantum and classical cases. In Sec. 6.1.2, we compare our results with those for the quantum version obtained by other methods. In Sec. 6.2, we show that our theoretical results well explain the data obtained in recent experiments for $S(\mathbf{q},\omega)$ (Sec. 6.2.1), $1/T_1$ (Sec. 6.2.2), and χ (Sec. 6.2.3).

6.1 Comparison with theoretical results

6.1.1 Classical Kitaev model

A classical version of the Kitaev model, in which the spin 1/2 operators in Eq. (1.1) are replaced by classical vectors, were studied theoretically [130–132]. The ground state of the classical Kitaev model has massive degeneracy. A part of the degenerate states are dubbed the Cartesian (CN) ground states. They are composed of different dimer coverings of the honeycomb structure, whose number grows exponentially with the system size. Different CN ground states are continuously connected with each other by appropriate spin rotations, which form the degenerate manifold. The classical Kitaev model has symmetry corresponding to the conserved quantities $\{W_p\}$ in the quantum case; for instance, π rotations of spins at 0, 1, 2, 3, 4, and 5 in Fig. 1.1 around the x, y, z, x, y, and z axis, respectively, do not change the energy. This means that spin correlations in the classical Kitaev model are also short-ranged, similar to the quantum case; $\langle S_j^\gamma S_{j'}^\gamma \rangle$ becomes nonzero only for NN γ bonds as well as the same site.

The dynamical spin structure factor $S(\mathbf{q},\omega)$ was computed for the classical Kitaev model by using the Landau-Lifshitz dynamics method for the samples generated by a classical Monte Carlo simulation. The results at $T = 0$ are shown in Figs. 6.1 in comparison with the results for the quantum case [132]. $S(\mathbf{q},\omega)$ for the classical case shares several features with the quantum case: a broad incoherent response extending to the high-ω region and a strong intensity in the low-ω region. The high energy response has a large weight around the Y (Γ) point for the FM (AFM) case, whereas the low energy one becomes large around the Γ (Y) point. On the other hand, in contrast to the quantum case in which $S(\mathbf{q},\omega)$ shows a flux gap, $S(\mathbf{q},\omega)$ in the classical case does not show any gap, but instead has a singularity at

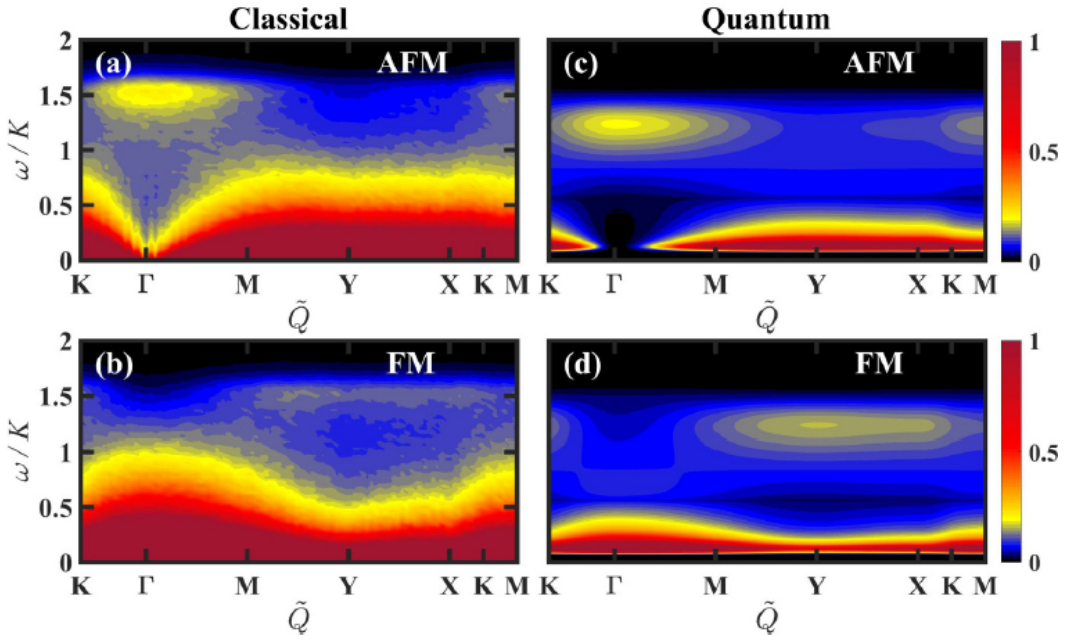

Figure 6.1: $S(\mathbf{q},\omega)$ for $T=0$ for the (a)(b) classical and (c)(d) quantum Kitaev models for the (a)(c) AFM and (b)(d) FM cases. The figures are taken from Ref. [132].

$\omega = 0$ [132]. This singularity is a consequence of the continuous degeneracy of the ground states [132].

Further analyses were performed from the viewpoint of magnon excitations from the CN ground states. For the CN ground states, within the linear spin-wave theory, the spin wave can propagate only along one-dimensional path which is composed of unsatisfactory bonds of dimer covering [130]. The density of states of the one-dimensional magnon band has a broad spectrum, which is reflected in the broad continuum of $S(\mathbf{q},\omega)$. Furthermore, the one-dimensional magnon band has a van-Hove singularity at the upper edge of the band, which results in the peak around the Y (Γ) point for the FM (AFM) case. As the one-dimensional magnon decomposes into a pair of spinons on including quantum fluctuations, it was discussed that the peculiar magnon excitations can be considered as a precursor of the Majorana excitations found in the quantum case [132].

T evolution of $S(\mathbf{q},\omega)$ for the classical Kitaev model is shown in Fig. 6.2. The corresponding results obtained by our numerical calculations for the quantum case are shown in Figs. 4.4(a)(d)(g)(j), 4.5(a)(d)(g)(j), and 5.4. For $T > T_{\rm H}$, $S(\mathbf{q},\omega)$ shows almost featureless response independent of $\mathbf{q}$ around $\omega = 0$, as shown in Figs. 6.2(d) and 6.2(h). On decreasing T below $T_{\rm H}$, $S(\mathbf{q},\omega)$ gradually acquires $\mathbf{q}$ dependence, and develops a weight in the high-ω region and a peak around $\omega = 0$. This T dependence is more clearly seen in the T-ω plot of $S(\mathbf{q},\Gamma)$ shown in Figs. 6.2(i) and 6.2(j). The broad weight around $\omega \simeq 0$ at high T is shifted to $\omega \simeq 1.5$ below $T_{\rm H}$ for the AFM case, whereas the strong peak appears around $\omega \simeq 0$ below $T_{\rm H}$ for the FM case. As in the $T = 0$ case, $S(\mathbf{q},\Gamma)$ does not show a gap around

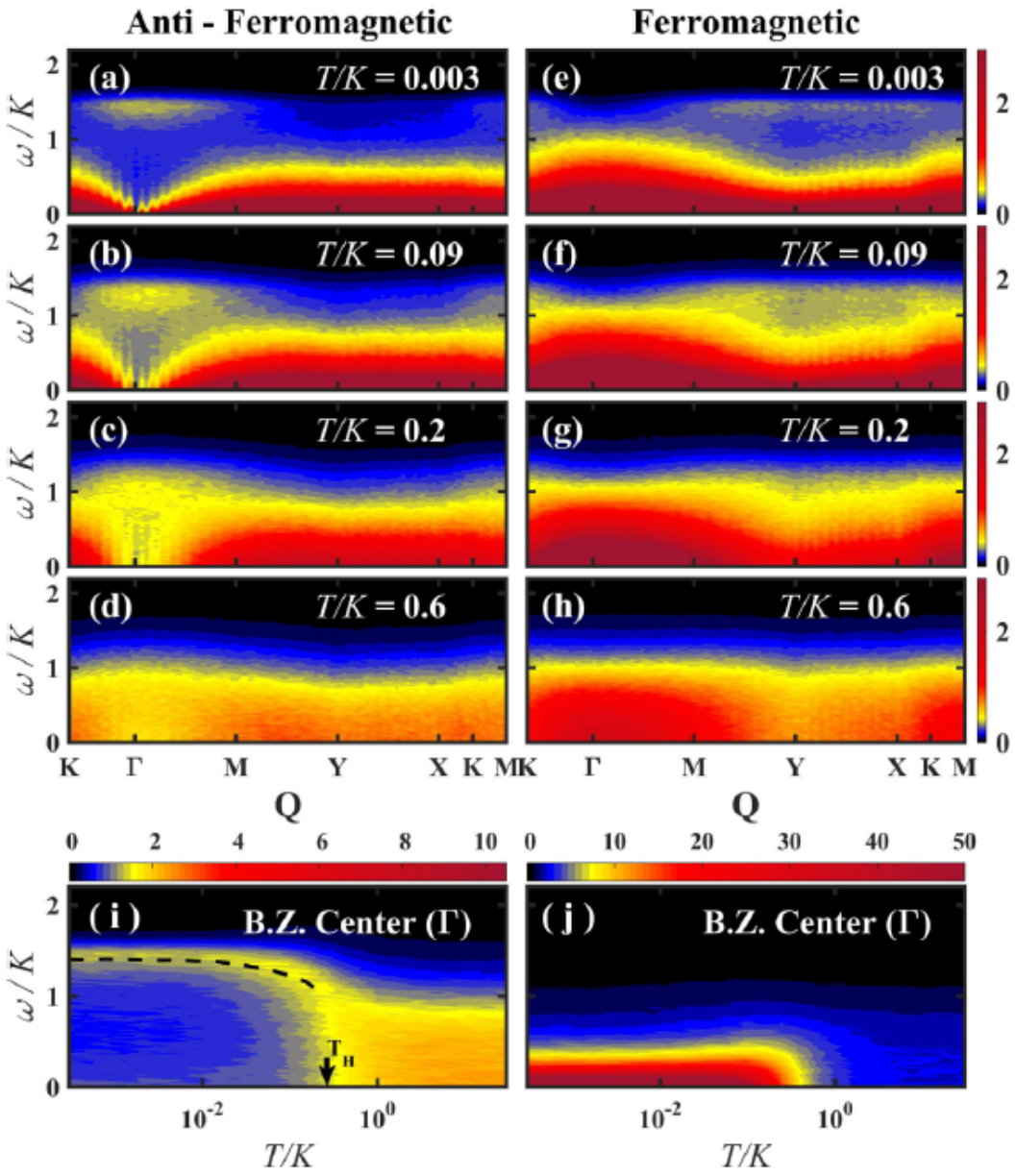

Figure 6.2: $S(\mathbf{q}, \omega)$ for several T for the (a)-(d) AFM and (e)-(h) FM cases. (i) and (j) display T dependences of $S(\mathbf{q}, \omega)$ for the AFM and FM cases, respectively. The dashed line in (i) represents the position of the high-energy peak. The figures are taken from Ref. [132].

$\omega \simeq 0$ at low T.

The lack of the gap is a clear difference between the classical and quantum cases. This difference will be reflected to $1/T_1$, although the calculations have not been done for the classical case. Note that the onsite (NN site) component of $1/T_1$ is proportional to $S(\mathbf{q}, \omega = 0)_{\mathrm{FM}} + (-)S(\mathbf{q}, \omega = 0)_{\mathrm{AFM}}$. Although the results in

Figs. 6.2(i) and 6.2(j) suggest that $1/T_1$ for the classical case increases below T_H in accordance with the quantum case, $1/T_1$ will not show a rapid decrease below T_L in contrast to the quantum case. Thus, several features at rather high T in the quantum case are reproduced in the classical correspondences, but the low-energy properties related to the Z_2 flux at low T are specific to the quantum Kitaev model.

6.1.2 Other calculations for the quantum Kitaev model

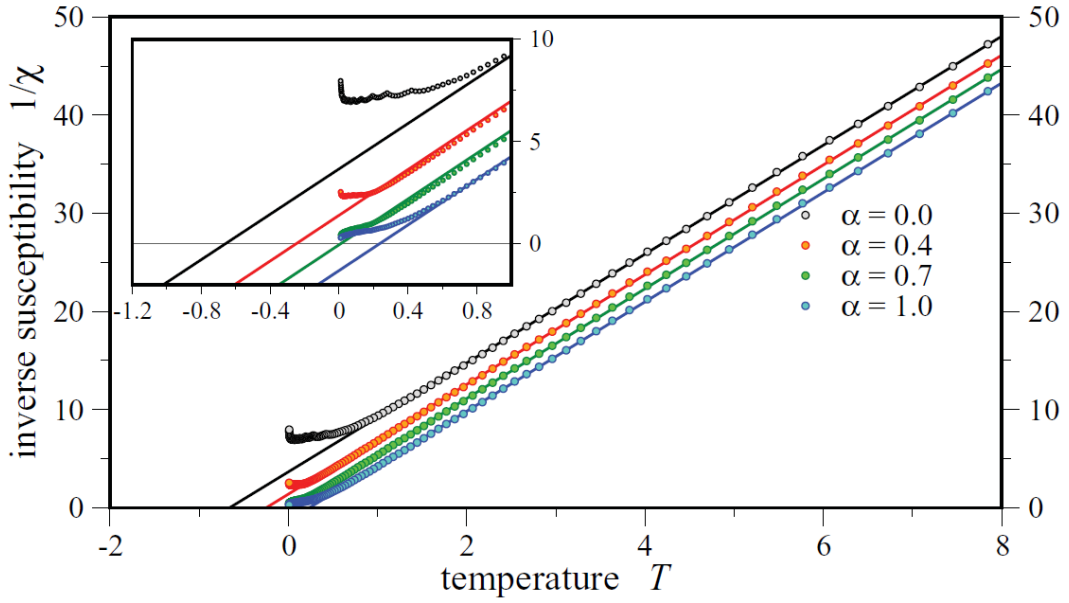

Figure 6.3: Inverse susceptibility $1/\chi$ for the Kitaev-Heisenberg model obtained by the PF-FRG approach. The result at $\alpha = 1.0$ corresponds to the pure Kitaev model. The figure is taken from Ref. [133].

Prior to our study, the magnetic susceptibility χ for the Kitaev-Heisenberg model was calculated by using a pseudofermion functional renormalization group (PF-FRG) approach [133, 134]. In the study, the Kitaev-Heisenberg Hamiltonian is parametrized as

$$\mathcal{H}_{\text{KitaevHeisenberg}} = (1-\alpha)\sum_{\langle j,j'\rangle} \mathbf{S}_j \cdot \mathbf{S}_{j'} - 2\alpha \sum_{\langle j,j'\rangle_\gamma} S_j^\gamma S_{j'}^\gamma. \tag{6.1}$$

In the PF-FRG approach, the ground state properties are explored by solving the coupled differential equations for one-particle irreducible m-particle vertex functions of pseudofermions with a positive integer m. The equations are solved with respect to the infrared frequency cutoff Λ for the free propagators of pseudofermions, starting from $\Lambda = \infty$ toward $\Lambda = 0$. At the end of the flow at $\Lambda = 0$ where the theory becomes cutoff free, the exact vertex functions are obtained if the equations are solved exactly [134]. In practice, up to two-loop contributions are taken into account [133]. In this method, finite-T properties are obtained by regarding Λ as T.

This is based on the assumption that T also works as an infrared cutoff, as the Matsubara frequency for $T > 0$ is discrete and the minimum value is nonzero. This scheme gives qualitatively correct results despite quantitative uncertainties [133].

The results of χ obtained by the PF-FRG approach for the Kitaev-Heisenberg model with several α are shown in Fig. 6.3. Here we concentrate on the case of the Kitaev model ($\alpha = 1$). χ for the Kitaev model obeys the Curie-Weiss form $\chi \propto 1/(T - T_{\rm CW})$ at high T, and starts to deviate while decreasing T. This behavior is consistent with our results shown in Figs. 4.12(a) and 5.2(a). However, there are quantitative differences between PF-FRG results and our results. For example, $T_{\rm CW} \simeq 0.22$ in the PF-FRG results in the scale of Eq. (6.1) with $\alpha = 1$ [133], whereas $T_{\rm CW} = 0.5$ in our results [rescaled in accordance with the definition of the Hamiltonian in Eq. (6.1)]. This difference might comes from the identification of T and Λ in the PF-FRG approach as noted above. In addition, the low-T behaviors of χ obtained in our results, a peak at slightly above $T_{\rm L}$ and substantial decrease around $T_{\rm L}$, are not captured in the PF-FRG results.

After our study, χ for the Kitaev-Heisenberg model was calculated by a high-T series expansions method [135]. The results were obtained for $T > 0.1$, which are consistent with our results.

Recently, a numerical method named the finite-T shifted Krylov subspace method for simulating spectra (FTKω) has been developed [136]. This method is based on the typicality approach and the shifted Krylov subspace method [136]. FTKω was applied to the Kitaev model on a 24-site cluster. The results for $S(\mathbf{q}, \omega)$ are compared with our CDMFT+CTQMC results in Chap. 4, as shown in Fig. 6.4. Note that $S(\mathbf{q}, \omega)$ shown in Figs. 6.4 and 6.5, including the CDMFT+CTQMC results, are multiplied by three compared to those in Eq. (3.44), due to the definition used in Ref. [136]. Overall, the results agree between two methods. However, there are small but non-negligible quantitative differences, which could be attributed to the finite-size effect in FTKω and the resolution of the MEM in CDMFT+CTQMC. Note that the effect of the cluster approximation in the latter is small, as discussed in Sec. 5.1.2.

$\mathbf{q}$ dependences of $S(\mathbf{q}, \omega)$ for the AFM Kitaev model with the isotropic interactions $J_x = J_y = J_z$ obtained by FTKω and CDMFT+CTQMC are compared in Fig. 6.5. Despite the discreteness in momentum space in FTKω, the results of FTKω and CDMFT+CTQMC are qualitatively consistent with each other. At $T = 0.1$, $S(\mathbf{q}, \omega)$ has a small (large) weight around the Γ point for small (large) ω, and it is almost independent of $\mathbf{q}$ in the intermediate-ω region. While increasing T, the over all tendency is the same but $\mathbf{q}$ dependence become weaker.

Very recently, another new method has been developed, which enables to calculate the real-time dynamical spin correlations $\langle S^{\gamma}_{j}(t) S^{\gamma}_{j'} \rangle$ for the Kitaev model at finite T [137]. The method has an advantage as it does not require the analytical continuation to obtain dynamical quantities as a function of real frequency, such as $S(\mathbf{q}, \omega)$.

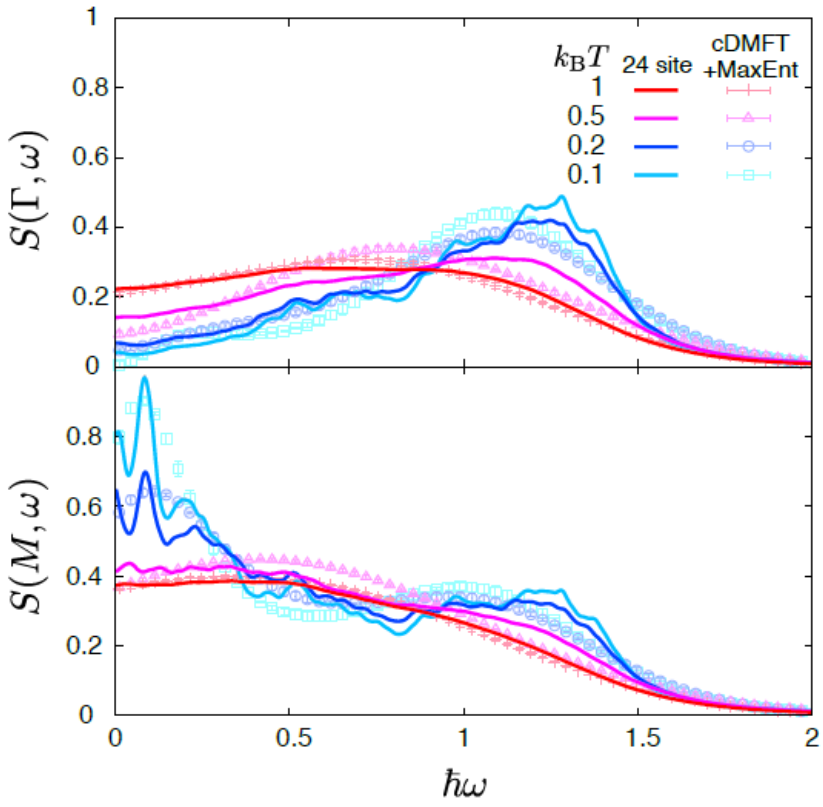

Figure 6.4: Comparison of $S(\mathbf{q},\omega)$ at the Γ and M points for the AFM case with the isotropic interactions $J_x = J_y = J_z$ between the FTKω results for a 24-site cluster and the CDMFT+CTQMC results supplemented by MaxEnt. The figures are taken from Ref. [136].

6.2 Comparison with experimental results

6.2.1 Dynamical spin structure factor

As introduced in Sec. 1.4.2, inelastic neutron scattering experiments were performed for powder samples of α-$RuCl_3$ [96]. The obtained spectra show a broad continuum up to $\sim$ 8 meV. In particular, the incoherent weight around 6.5 meV does not change below and above T_N, as shown in Figs. 1.12(a) and 1.12(b), respectively, suggesting that the response originates from not the interactions causing the magnetic order but the predominant Kitaev interactions. The incoherent response survives up to $\sim$ 70 K, well above T_N. These results are considered as a sign of fractionalized spin excitations in α-$RuCl_3$ as the proximity effect to the Kitaev QSL [96].

Subsequently, inelastic neutron scattering experiments were performed also for single crystal samples of α-$RuCl_3$ [74, 99, 138, 139], and $S(\mathbf{q},\omega)$ are closely examined including the $\mathbf{q}$ dependence. In these studies, the continuum was clearly observed and the Kitaev interactions are again considered to be crucial to explain it. Never-

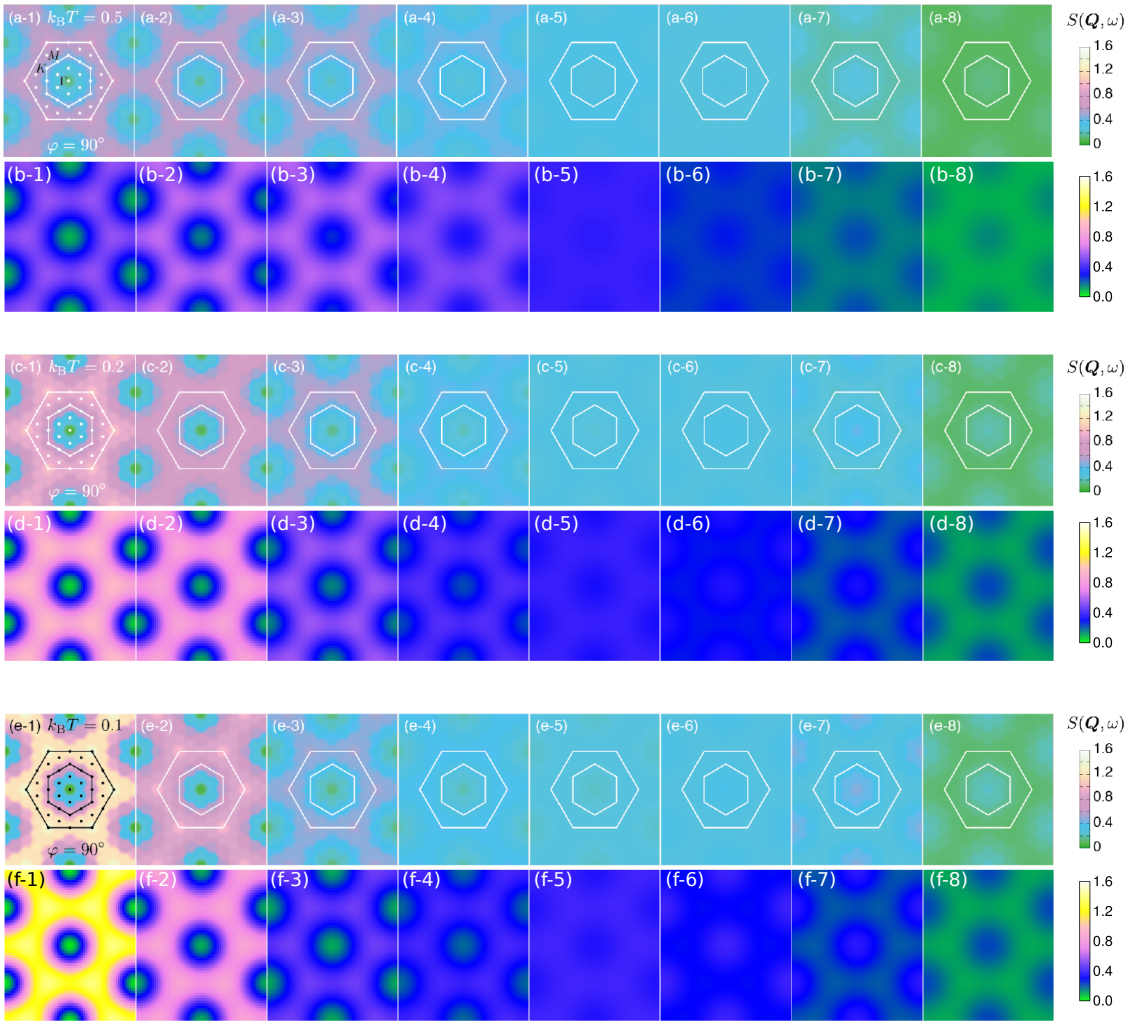

Figure 6.5: $\mathbf{q}$ dependence of $S(\mathbf{q},\omega)$ for the AFM Kitaev model averaged between the ω window of (a-1) [0.0, 0.1], (a-2) [0.2, 0.3], (a-3) [0.4, 0.5], (a-4) [0.6, 0.7], (a-5) [0.8, 0.9], (a-6) [1.0, 1.1], (a-7) [1.2, 1.3], and (a-8) [1.4, 1.5], and similarly for (b)-(f), at (a)(b) $T = 0.5$, (c)(d) $T = 0.2$, and (e)(f) $T = 0.1$. The results in (a)(c)(e) are obtained by FTKω and (b)(d)(f) by CDMFT+CTQMC. The figures are taken and modified from Ref. [136].

theless, the proper form of the Hamiltonian including the interactions beyond the Kitaev type, which reproduces the fine details of the results, is still controversial, even including the sign of the Kitaev interactions.

We here present an example of close comparison between our theoretical results and experimental data [74]. The comparison is shown in Fig. 6.6. In the experiment, the raw data includes phonon contributions in addition to magnetic contributions. To subtract the phonon contributions, the data at $T = 290$ K with the Bose factor correction are subtracted from the data at lower T in Fig. 6.6. Although our theory

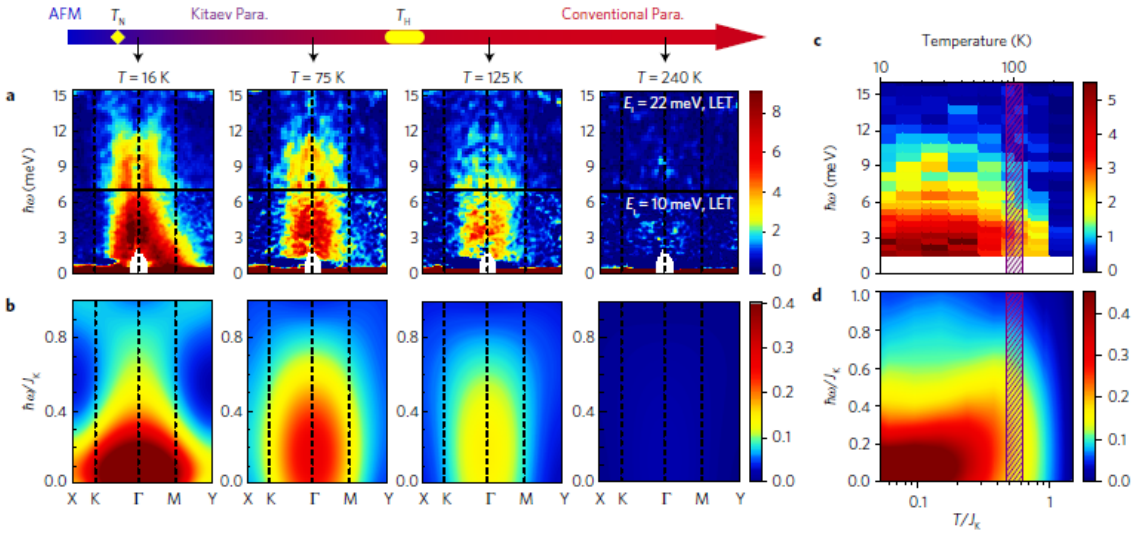

Figure 6.6: (a) Experimental results of $S(\mathbf{q},\omega)$ for α-$RuCl_3$ at $T = 16$, 75, 125, and 240 K, respectively. (b) Our theoretical results for the Kitaev model in the FM case with isotropic interaction at $T = 0.09$, 0.375, 0.69, and 1.32, which correspond to the T sets in (a) by assuming $J = 16.5$ meV. (c) and (d) display the T dependences of $S(\mathbf{q},\omega)$ at the Γ point in the experiment and our theory, respectively. The figures are taken from Ref. [74].

does not include the phonon contributions, the same procedure is applied also to the theoretical results. As shown in Fig. 6.6(a), the experimental result of $S(\mathbf{q},\omega)$ shows a broad incoherent response centered at the Γ point. While increasing T to $T = 75$ K and $T = 125$ K, the weight gradually decreases without notable change in the $\mathbf{q}$ and ω dependence, and the weight vanishes for higher T. These features of T, $\mathbf{q}$, and ω dependence are all consistent with our theoretical results, by taking $J = 16.5$ meV, as shown in Fig. 6.6(b). The T dependences of $S(\mathbf{q},\omega)$ at the Γ point are more closely compared in Figs. 6.6(c) and 6.6(d). The results clearly show that the incoherent weight grows below ~ 125 K in a similar fashion in both experimental and theoretical results.

Recently, inelastic neutron scattering experiments were performed for α-$RuCl_3$ under a magnetic field [139]. At zero field, the spectrum below the Néel temperature has relatively sharp dispersions originating from magnon excitations in addition to the incoherent response, but the dispersions disappear above the Néel temperature, leaving the incoherent response [74, 96, 99, 138, 139]. A similar change was observed while suppressing the magnetic order by the magnetic field, instead of increasing T. The result is interpreted as a signature of the field-induced Kitaev QSL [139].

6.2.2 NMR relaxation rate

NMR measurements have been done for α-$RuCl_3$ by several groups [80, 81, 140, 141]. Although the dichotomy between static and dynamical spin correlations might be blurred by additional interactions to the Kitaev model, we expect that the increase of $1/T_1$ without magnetic ordering can be a signature of the fractionalization in the Kitaev QSLs. In all results, peculiar behavior of $1/T_1$ was observed: $1/T_1$ increases while decreasing T and turns to decrease at a lower T without showing magnetic ordering. However, the estimate of the spin gap from the low-T behavior is controversial. Under the magnetic field, both gapless [81] and gapped QSLs [80, 140, 141] were reported. The gapless QSL behavior is not expected for the Kitaev model as well as its extensions [81]. Meanwhile, the gapped behavior is interpreted in line with the proximity to the Kitaev QSL [80, 140, 141], but the field dependences of the gap are scattered among the studies.

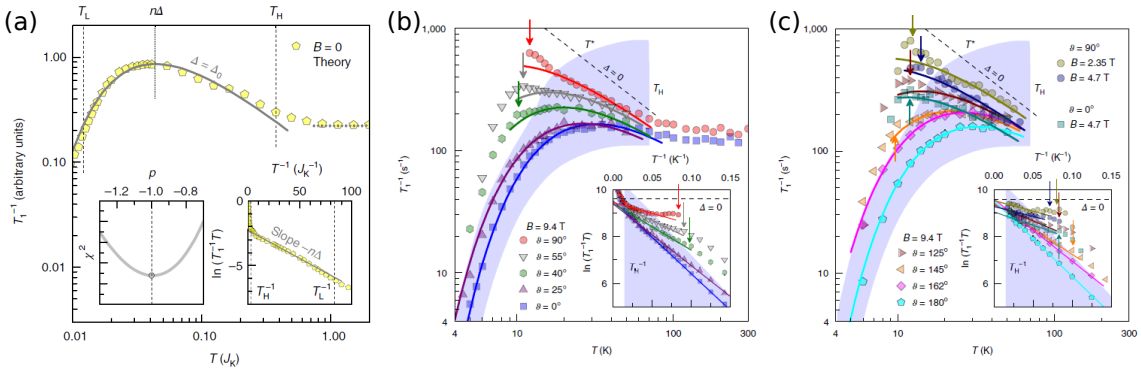

Figure 6.7: (a) Our theoretical results of $1/T_1$ for the Kitaev model with isotropic interactions. The solid curve represents the fitting to the results by Eq. (6.2). The left inset shows the goodness of fitting, χ^2, obtained by changing the parameter p in the equation, $1/T_1 \propto T^p \exp(-n\Delta/T)$. As shown in the inset, χ^2 takes a minimum almost at $p = -1$ [140]. The right inset shows the $\ln(T_1^{-1}T)$ as a function of $1/T$ for the same data with the main panel, to demonstrate the linear dependence of $\ln(T_1^{-1}T)$ on T^{-1}. (b) and (c) Experimental results of $1/T_1$ for α-$RuCl_3$ obtained by changing the magnetic field strength and the direction of the field, respectively. θ represents the angle of the magnetic field measured from the honeycomb plane. The solid curves shows the fitting by Eq. (6.2). The arrows indicate the magnetic transition temperatures, and the purple regions represent the T ranges used for fitting. The insets in (b) and (c) show the $\ln(T_1^{-1}T)$ as a function of $1/T$, similar to the right inset in (a). The figures are taken and modified from Ref. [140].

We here introduce a recent NMR study in which the experimental results are closely compared with our theoretical results [140]. In this study, it was pointed out that the T dependence of $1/T_1$ obtained in our study is well reproduced by the

empirical expression

$$1/T_1 \propto \frac{1}{T}\exp\left(-\frac{n\Delta}{T}\right), \tag{6.2}$$

as shown in Fig. 6.7(a). The fitting by setting the spin gap Δ at the two-flux gap gives $n = 0.67$. By fixing $n = 0.67$, the experimental results while varying the magnetic field were fitted by using Eq. (6.2), for the T range by excluding the critical region associated with the magnetic ordering. All the experimental results obtained for different magnetic field strengths and directions are well fit by Eq. (6.2), as shown in Figs. 6.7(b) and 6.7(c). In particular, in the cases for which the magnetic field suppresses the magnetic transition, the experimental data are excellently reproduced by the fitting down to the lowest T measured. Note that the change of the field direction corresponds to a change of the field strength effectively, as the g-factor is different for the in-plane and out-of-plane magnetic field. The fitting results indicate that the spin gap appears to be proportional to the cubic of the magnetic field strength except for the constant term. Note that the cubic dependence was predicted for the gap in the Majorana excitations by the perturbation theory [26], while the relation to the spin gap remains elusive beyond the perturbation.

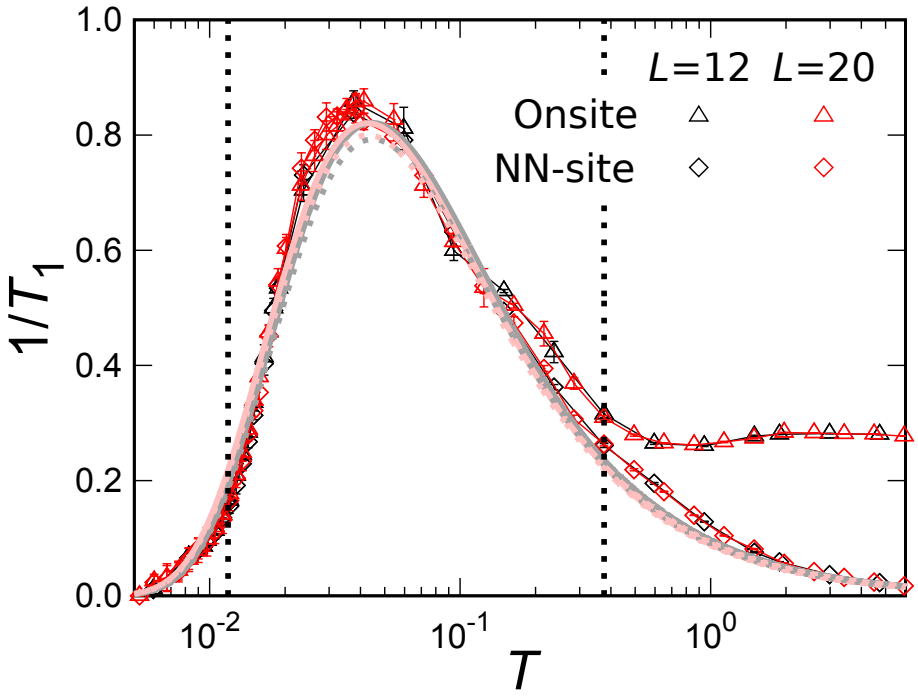

Figure 6.8: Fitting to our QMC+CTQMC results of $1/T_1$ by using Eq. (6.2). The data are same with those in Fig. 5.1(a). The solid (dotted) lines are for the onsite (NN site) component, whereas the gray (pink) lines are for $L = 12$ ($L = 20$). The vertical dotted lines represent $1/T_{\rm H}$ and $1/T_{\rm L}$ respectively.

Stimulated by this experimental study, we test the empirical formula in Eq. (6.2) for our numerical data. In Fig. 6.7(a), the data used for the fitting were those for

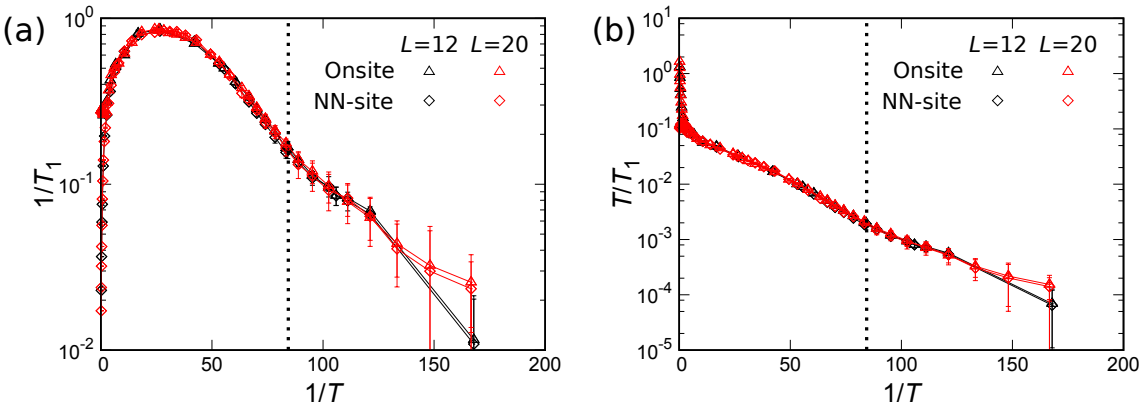

Figure 6.9: Semilog plots of the QMC+CTQMC results for (a) $1/T_1$ and (b) T/T_1 for the 2D honeycomb Kitaev model with the isotropic interactions, plotted as functions of $1/T$. The data are same with those in Fig. 5.1(a). The vertical dotted lines represent $1/T_{\rm L}$.

$T_{\rm L} < T < T_{\rm H}$ obtained by QMC+CTQMC. Here, we try the fitting by using the data for the entire T range below $T_{\rm H}$ including the data at much lower T than in Fig. 6.7(a). As shown in Fig. 6.8, the overall T dependence of $1/T_1$ is reproduced by Eq. (6.2), even down to the lowest T well below $T_{\rm L}$. However, we note that it is difficult to conclude the precise form of the low-T asymptotic behavior of $1/T_1$. For example, if $1/T_1$ at asymptotically low T is given by Eq. (6.2), $\log T/T_1$ is given by a linear function of $1/T$. Meanwhile, if we assume simply the form of $1/T_1 \propto \exp(-n\Delta/T)$, $\log 1/T_1$ is linear to $1/T$. But our theoretical results do not have sufficient precision at low T to tell which is plausible, as shown in Fig. 6.9.

Very recently, the NMR experiment was conducted also for a newly-found material $H_3LiIr_2O_6$ [63]. $1/(T_1T)$ measured for ^{7}Li and ^{1}H show different T dependences at high T. $1/(T_1T)$ for ^{7}Li shows a dip around $T = 50$ K, whereas that for ^{1}H shows a monotonic increase while decreasing T in the same T range. The difference was interpreted by the different form factors for ^{7}Li and ^{1}H. The increase of $1/T_1$ for ^{1}H appears to be consistent with our theoretical results, but the T range is narrower than the theory. The dip of $1/(T_1T)$ for ^{7}Li was ascribed to spin correlations beyond nearest-neighbor pairs, which vanish in the Kitaev model. While further decreasing T, $1/(T_1T)$ for ^{7}Li and ^{1}H show qualitatively the same T dependences; $1/(T_1T)$ only weakly depends on T below $T \simeq 20$ K. The $1/(T_1T)$ constant behavior is not predicted for the Kitaev model where $1/T_1$ decays exponentially. At lower T, $1/(T_1T)$ starts to decrease below $T \simeq \mu_{\rm B}B/k_{\rm B}$, where $\mu_{\rm B}$ is the Bohr magneton and B is the strength of the magnetic field. In addition, $1/T_1$ as a function of T/B for several B and for both ^{7}Li and ^{1}H almost collapse onto a single curve at low T, with multiplication of appropriate constant factors. Many causes have been discussed for the peculiar behavior at low T: for instance, effects of randomness or defects, such as stacking fault and randomness in the bond-dependent interactions, magnetic anisotropy, and additional interactions [63–65, 142].

6.2.3 Magnetic susceptibility

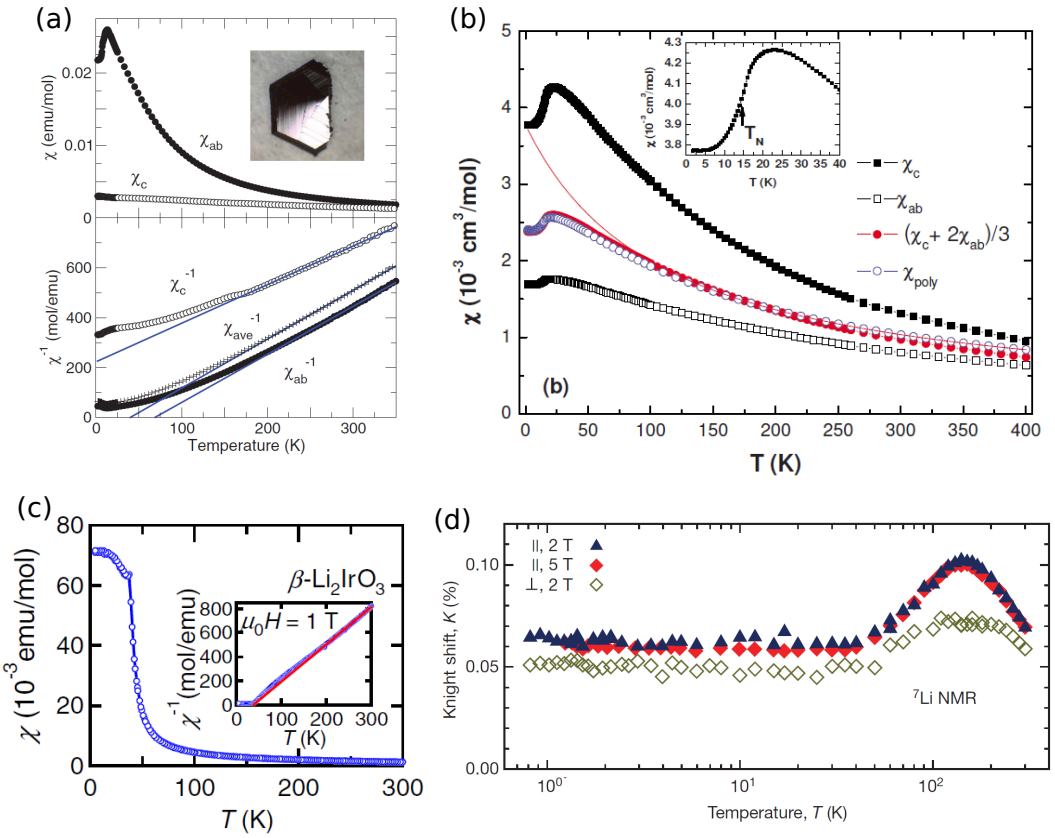

Figure 6.10: T dependences of the magnetic susceptibility χ of (a) α-$RuCl_3$, (b) Na_2IrO_3, and (c) β-Li_2IrO_3, and (d) the Knight shift of $H_3LiIr_2O_6$. The result in the magnetic field parallel (perpendicular) to the honeycomb plane is represented as χ_{ab} (χ_c) in (a) and (b), and as $\parallel$ ($\perp$) in (d). χ_{poly} in (b) represents the data for a polycrystalline sample. The solid lines in (a) and (b) and the inset of (c) represent the Curie-Weiss fit to χ at high T. The figures are taken and modified from Ref. [55, 63, 71, 86].

Fig. 6.10 summarizes the T dependences of the magnetic susceptibility χ of α-$RuCl_3$, Na_2IrO_3, and β-Li_2IrO_3 and the Knight shift K of $H_3LiIr_2O_6$ [55, 63, 71, 86]. K provides a measure of the magnetic susceptibility, avoiding extrinsic effects, such as magnetic impurities. χ and K both obey the Curie-Weiss law at high T, and start to deviate from it between 100 K and 200 K. As introduced in Sec. 1.3, these materials show magnetic orders at low T except for $H_3LiIr_2O_6$. α-$RuCl_3$ shows the magnetic phase transition at 7 K (or 10-15 K depending on samples), which corresponds to the peak of χ [71]. Na_2IrO_3 and β-Li_2IrO_3 show the magnetic phase transitions at 15 K and 38 K, respectively. In the case of Na_2IrO_3, χ shows a peak at $T \simeq 23$ K and then decreases on lowering T even above the Néel temperature, as shown in the inset of Fig. 6.10(b).

Compared to $S(\mathbf{q},\Gamma)$ and $1/T_1$, it is rather difficult to find clear indication of the proximity to the Kitaev QSL solely by χ. For $S(\mathbf{q},\Gamma)$ and $1/T_1$, we found peculiar behaviors associated with the Kitaev QSL in the wide energy and T ranges. On the other hand, in the same T region, χ shows just a deviation from the Curie-Weiss behavior, which is commonly seen in frustrated magnets and not characteristic to the Kitaev model. The most characteristic feature of χ in our numerical results for the Kitaev model is the rapid decrease of χ around $T_{\rm L}$ ($T_{\rm c}$) in the 2D honeycomb (3D hyperhoneycomb) case, as shown in Chap. 5. However, such behavior at very low T might be affected by other interactions, or hidden by magnetic orders in the real materials. For Na_2IrO_3 in Fig. 6.10(b), even though the peak and subsequent decrease of χ at low T on decreasing T is observed above $T_{\rm N}$, it is difficult to interpret it as a sign of the proximity to the Kitaev QSL, as similar behavior is also widely seen in frustrated magnets associated with the growth of short-range spin correlations.

We note that, in Figs. 6.10(a), 6.10(b), and 6.10(d), for which the data were measured for single crystal samples, a rather strong magnetic anisotropy is observed between the in-plane and out-of-plane magnetic fields. Such an anisotropy is not understood by the pure Kitaev model. The magnetic anisotropy in the candidate materials were examined by comparing the observed magnetic order and theoretical prediction of the magnetic order for an extended Kitaev model [143]. The anisotropy of χ for α-$RuCl_3$ was also used to estimate the parameters of the effective Hamiltonian, by comparing it with the theoretical estimate obtained by a high-T expansion [144].

6.3 Summary of this chapter

In this chapter, we have discussed our theoretical results obtained in the previous chapters in comparison with other theoretical results for the Kitaev model and experimental results for the Kitaev candidate materials. In the comparison with the classical version of the Kitaev model, we found that the high-T and large-ω behaviors are common to the quantum and classical cases. On the other hand, there are significant differences in the low-T and small-ω properties, which are associated with gap opening in the Z_2 flux excitations in the quantum case. Meanwhile, in the comparison with other theoretical results for the quantum version, we found that our results for χ, which are exact within the statistical errors, show not only quantitatively but also qualitatively different behavior compared to those obtained by the previous PF-FRG study. On the other hand, the overall behaviors in our results for $S(\mathbf{q},\omega)$ are well reproduced by the FTKω calculations for a 24-site cluster.

We also compared our results with the experimental results of $S(\mathbf{q},\omega)$, $1/T_1$, and χ for the Kitaev materials. Our results for the Kitaev model well explain the high-T behaviors of $S(\mathbf{q},\omega)$ and $1/T_1$ in experiments. On the other hand, the low-T features of $1/T_1$ and χ in our results are masked by the magnetic ordering or modified by unknown reasons in the candidate materials. However, when the magnetic orders are suppressed by applying the magnetic field, peculiar behaviors were experimentally observed for $S(\mathbf{q},\omega)$ and $1/T_1$, which are, at least, qualitatively similar to out results

for the Kitaev model at zero field. The agreement suggests the possibility of field-induced Kitaev QSLs. For further comparison, it is highly desired to obtain reliable theoretical results in a magnetic field for the pure and extended Kitaev models.

7
Summary

In this thesis, we have theoretically clarified spin dynamics at finite T of the Kitaev model, which serves as an important clue on experimental identification of the Kitaev QSL behavior in real materials. To achieve this, we have developed new numerical techniques, the CDMFT and CTQMC methods, based on the Majorana fermion representation. We computed the dynamical spin structure factor $S(\mathbf{q}, \omega)$, the NMR relaxation rate $1/T_1$, and the magnetic susceptibility χ for the Kitaev models on both 2D honeycomb and 3D hyperhoneycomb structures. We found that the fractionalization of spin degree of freedom into matter fermions and Z_2 fluxes strongly affects the T and energy dependence of the dynamical quantities through the different energy scales of the fractional excitations. These characteristic features are not seen in conventional paramagnets, and hence, they will be useful for the identification of the Kitaev QSL behavior in candidate materials. We also clarified that the effects of fractionalization are commonly seen in both 2D and 3D cases, except for the low-T behavior corresponding to the freezing of Z_2 fluxes; dynamical quantities show critical behaviors associated with the peculiar phase transition between the high-T paramagnetic and low-T QSL phases in the 3D case, while they show just crossover behaviors in the 2D case.

In Chap. 1, we gave an overview of previous efforts to search for QSLs both experimentally and theoretically. After briefly discussing the previous studies for general QSLs, we reviewed the recent intensive studies for the Kitaev model as a new and attractive route to realize QSLs in real materials. Clarifying open problems through the review, we also presented the purpose of this thesis.

In Chap. 2, we introduced the Kitaev model and a Majorana fermion representation used in the following numerical calculations.

In Chap. 3, we introduced numerical methods used in this thesis. Among them, Majorana CDMFT and Majorana CTQMC were newly developed in this thesis and applied to the Kitaev model. We showed how to compute the dynamical spin correlations by combining Majorana CDMFT and Majorana CTQMC (CDMFT+CTQMC) and Majorana QMC and Majorana CTQMC (QMC+CTQMC). We also introduced the MEM to compute the real-frequency dependence.

In Chap. 4, we presented the results obtained by the CDMFT+CTQMC method for the Kitaev model on the 2D honeycomb lattice. First, we performed benchmark of the CDMFT method in comparison with the QMC. We confirmed that the results by CDMFT precisely reproduce the results by QMC down to just above the low-T crossover temperature T_{L} where the CDMFT results show an artificial phase transition because of its mean-field nature. We also presented the cluster size dependence of the CDMFT+CTQMC results. Next, on the basis of the benchmark, we applied

the CDMFT+CTQMC method in the qualified T range above $T_{\rm L}$. We calculated the experimentally-measurable quantities, $S(\mathbf{q},\omega)$, $1/T_1$, and χ. Our main finding is that all these dynamical quantities show peculiar behavior reflecting the fractionalization of spin degree of freedom. The most prominent feature is the dichotomy between static and dynamical spin correlations as a consequence of the spin fractionalization. The dichotomy appears clearly in the increase of $1/T_1$ below $T_{\rm H}$ where the fractionalization sets in, despite the saturation of static spin correlations. We find similar contrasting behavior also in the T and energy dependence of $S(\mathbf{q},\omega)$: While incoherent response around $\omega \sim J$ appears below $T_{\rm H}$, a quasi-elastic peak of $S(\mathbf{q},\omega)$ around $\omega = 0$ rapidly grows toward $T_{\rm L}$. Meanwhile, χ deviates from the Curie-Weiss law below $T_{\rm H}$, despite the growth of the $1/T_1$. Our results suggest that these peculiar behaviors are found universally in the fractionalized paramagnetic region irrespective of the anisotropy in the system. On the other hand, we also clarified interesting behaviors that depend on the anisotropy at lower T. When one of the three bond-dependent interactions is stronger than the other two, the spin dynamics shows peculiar T and energy dependences distinct from those in the isotropic case as follows. The most characteristic behavior is that as lowering T below $T_{\rm H}$, $S(\mathbf{q},\omega)$ develops a δ-function like peak, which is well separated from the incoherent continuum. We also showed that the strong suppression of χ at low T are qualitatively explained by the two-site dimer model on the strong bond. In contrast, when the anisotropy is opposite, i.e., when the two types of bonds become stronger, the results are qualitatively unchanged from those for the isotropic case, while the effect of anisotropy appears in the $\mathbf{q}$ dependence in $S(\mathbf{q},\omega)$ and the different components in $1/T_1$ and χ.

In Chap. 5, we presented the results by the QMC+CTQMC method for the Kitaev models on the 2D honeycomb and 3D hyperhoneycomb structures. We investigated the behavior of $S(\mathbf{q},\omega)$, $1/T_1$, and χ of the Kitaev model in all T including below $T_{\rm L}$, where the CDMFT is not applicable. We found that $1/T_1$ shows a peak slightly above $T_{\rm L}$ and decays to zero on further decreasing T, reflecting the gap opening in the flux excitations. We also revealed that the quasi-elastic peak of $S(\mathbf{q},\omega)$ becomes shaper and shifts to a nonzero ω corresponding to the gap opening below $T_{\rm L}$. χ also shows a peak slightly above $T_{\rm L}$ followed by a substantial decrease around $T_{\rm L}$, and finally converges to a nonzero value as $T \to 0$. We discussed the influence of thermally fluctuating Z_2 fluxes, with focusing on the differences arising from the spatial dimensions. In the 2D honeycomb case, everything changes smoothly while lowering T, reflecting the crossover associated with particlelike Z_2 flux excitations. In contrast, in the 3D hyperhoneycomb case, the system exhibits a phase transition by the proliferation of looplike Z_2 flux excitations, which leads to singular behaviors in the dynamical properties. We found that the dichotomy between static and dynamical spin correlations, which begins below the high-T crossover at $T_{\rm H}$ associated with itinerant matter fermions, persists down to the low-T region, in a more peculiar form reflecting thermally excited Z_2 fluxes; while the dichotomy in the higher-T region is rather universal independent of the spatial dimension, the low-T one appears differently between 2D and 3D, reflecting the different nature of the localized Z_2 flux excitations. We showed that the T derivatives of the $1/T_1$ and χ provide good

probes for fluctuating Z_2 fluxes in both 2D and 3D cases.

In Chap. 6, we discussed our theoretical results obtained in Chaps. 4 and 5 in comparison with other theoretical results for the Kitaev model and experimental results for candidate materials. First, by comparing our results with the results for the classical version of the Kitaev model, we found that the high-T and large-ω properties obtained in our results are commonly seen in the classical counterpart. On the other hand, the low-T and small-ω properties mainly related to the Z_2 flux are specific to the quantum case. Next, we showed a comparison with the results for a 24-site cluster obtained by FTKω, which reproduce well our results despite the discreteness in momentum space. In comparison with experiments, we found that our theoretical results well explain the available data of $S(\mathbf{q},\omega)$, $1/T_1$, and χ for the Kitaev candidate materials. We showed that the peculiar behavior we found for $S(\mathbf{q},\omega)$ and $1/T_1$, the appearance of the broad incoherent response centered at the Γ point and the increase of $1/T_1$ below $T_{\rm H}$, are indeed observed experimentally in the paramagnetic state above the critical temperature for magnetic ordering. We also discussed several recent experimental efforts to find the Kitaev QSL behavior by suppressing the magnetic orders by a magnetic field. For instance, we introduced an experimental study of $1/T_1$ under the magnetic field, which shows good agreement down to the lowest T measured with our theoretical results at zero field. This appears to support the realization of the field-induced Kitaev QSLs. T dependence of χ obtained in our theoretical results are also observed in experiments, at least, qualitatively. The deviation from the Curie-Weiss law at high T is commonly observed among candidate materials, and the decrease of χ at low T is observed in some materials. Nevertheless, it is difficult to interpret these behaviors as the sign of the Kitaev QSL, as they are commonly seen in frustrated magnetic systems.

The outcomes of this thesis will bring about a great impact on understanding of the Kitaev QSL both theoretically and experimentally. Our findings of peculiar behavior of experimentally measurable quantities, $S(\mathbf{q},\omega)$, $1/T_1$, and χ, will stimulate experimental exploration of Kitaev QSLs. Indeed, after our theoretical studies, several experiments have been performed, e.g., for $S(\mathbf{q},\omega)$ and $1/T_1$, and the data have been analyzed in comparison with our results. The comparisons suggest the proximity effects to the Kitaev QSL, as discussed in Chap. 6. Similar collaborative studies between theory and experiment are in progress, and we believe that our findings will significantly contribute to future development in this rapidly growing field.

Finally, let us discuss remaining issues. An important open problem is to clarify the behavior of the Kitaev model in an applied magnetic field. As discussed in Chap. 6, the possibility of the Kitaev QSLs in an applied magnetic field has been intensively explored for the candidate materials. In addition to the experiments discussed in Chap. 6, very recently, a thermal transport measurement for α-$RuCl_3$ also suggested that the Kitaev QSL with peculiar topological properties is realized under a magnetic field [145]. Nevertheless, the nature of the field-induced disordered state is unclear thus far. In this situation, theoretical studies of the Kitaev model in a magnetic field are of great importance, but they are not easy since the exact solution is no longer available for nonzero fields. The Majorana CDMFT method

newly developed in this thesis provides a framework which enables to incorporate the external magnetic field to the Kitaev model beyond the exact solvability. Another important issue is to consider the effect of additional interactions to the Kitaev ones existing in real materials. There have been many theoretical studies for such extended Kitaev models, but the unbiased results were limited to those obtained by the exact diagonalization on small clusters. It may also be intriguing to study the Kitaev models with impurities and randomness in the exchange couplings, for exploring the origin of the peculiar behaviors found in $H_3LiIr_2O_6$. It will be interesting to extend the CTQMC method for the applications to such extended models.

A
Kitaev Hamiltonian in reciprocal space

In this Appendix, we discuss the eigenstates of the flux free state in the Majorana fermion representation of the Kitaev model in Eq. (1.10). In Eq. (1.10), the flux free state is given by taking all $u^{\gamma}_{j,j'} = 1$ for $j \in b$ and $j' \in w$; namely, the Hamiltonian is given as

$$\mathcal{H}^{\text{flux free}}_{\text{Kitaev}} = i\frac{J_x}{4}\sum_{(j,j')_x} c_j c_{j'} + i\frac{J_y}{4}\sum_{(j,j')_y} c_j c_{j'} + i\frac{J_z}{4}\sum_{(j,j')_z} c_j c_{j'} \tag{A.1}$$

$$= \frac{1}{4}\sum_{j,j'} H_{j,j'} c_j c_{j'}, \tag{A.2}$$

where $H_{j,j'}$ is a pure-imaginary Hermitian matrix. This Hamiltonian has translational symmetry, and hence, $H_{j,j'}$ depends only on the relative position of the sites j and j'. By Fourier transformation, we obtain

$$\begin{aligned}\mathcal{H}^{\text{flux free}}_{\text{Kitaev}} &= \frac{1}{4}\sum_{s,s',m,m'} H_{m,m'}(s,s') c_{s,m} c_{s',m'} \\ &= \frac{1}{2}\sum_{m,m',\mathbf{k}} \tilde{H}_{m,m'}(\mathbf{k}) d_{-\mathbf{k},m} d_{\mathbf{k},m'} \\ &= {\sum_{m,m',\mathbf{k}}}' \tilde{H}_{m,m'}(\mathbf{k}) \left(d^{\dagger}_{\mathbf{k},m} d_{\mathbf{k},m'} - \frac{1}{2}\delta_{m,m'} \right).\end{aligned} \tag{A.3}$$

In the first line of Eq. (A.3), instead of the site index j, we use the unitcell index s and the sublattice index m. A schematic picture of the unitcell is shown in Fig. A.1. In the second line, $\tilde{H}_{m,m'}(\mathbf{k})$ and $d_{\mathbf{k},m}$ are defined as

$$\tilde{H}_{m,n}(\mathbf{k}) = \sum_{s} H_{m,m'}(s,0) e^{-i\mathbf{k}\cdot\mathbf{r}_s}, \tag{A.4}$$

$$d_{\mathbf{k},m} = \frac{1}{\sqrt{2N}}\sum_{s} e^{-i\mathbf{k}\cdot\mathbf{r}_s} c_{s,m}, \tag{A.5}$$

respectively, where N is the number of sites. $\tilde{H}_{m,m'}(\mathbf{k})$ is a 2×2 matrix of the form

$$\tilde{H}_{m,n}(\mathbf{k}) = \begin{pmatrix} 0 & a(\mathbf{k}) \\ a(\mathbf{k})^* & 0 \end{pmatrix} \tag{A.6}$$

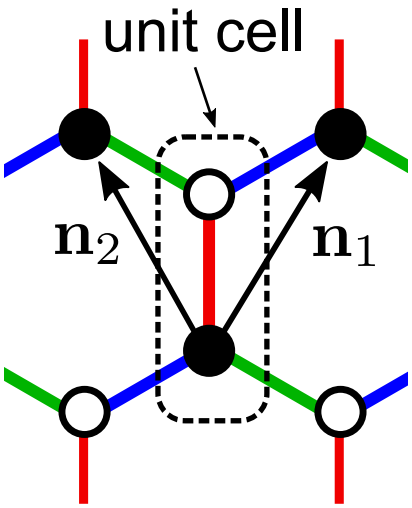

Figure A.1: Schematic picture of a unitcell and the lattice translation vectors of the honeycomb lattice.

with

$$a(\mathbf{k}) = \frac{i}{2}(J_x e^{-i\mathbf{k}\cdot\mathbf{n}_1} + J_y e^{-i\mathbf{k}\cdot\mathbf{n}_2} + J_z), \tag{A.7}$$

where $\mathbf{n}_1$ and $\mathbf{n}_2$ are the lattice translation vectors shown in Fig. A.1. In the third line of Eq. (A.3), the sum $\sum'$ is taken for either one of $\mathbf{k}$ and $-\mathbf{k}$. Note that $\tilde{H}_{m,m'}(\mathbf{k}) = -\tilde{H}_{m',m}(-\mathbf{k})$ and $d_{-\mathbf{k},m} = d^\dagger_{\mathbf{k},m}$. By diagonalizing Eq. (A.6), the eigenvalue is given as

$$\epsilon(\mathbf{k}) = \pm|a(\mathbf{k})|. \tag{A.8}$$

$\epsilon(\mathbf{k})$ can be zero if J_γ satisfies the following three relations simultaneously:

$$|J_x| \leq |J_y| + |J_z|, \tag{A.9}$$
$$|J_y| \leq |J_z| + |J_x|, \tag{A.10}$$
$$|J_z| \leq |J_x| + |J_y|. \tag{A.11}$$

In this case, the Majorana spectrum $\epsilon(\mathbf{k})$ has gapless excitations. Otherwise, it is fully gapped in the entire Brillouin zone. The results is summarized as the phase diagram in Fig. 1.2.

B

Plots of $1/T_1$ and χ in the T-linear scale

In Chaps. 4 and 5, we show the NMR relaxation rate $1/T_1$ and the magnetic susceptibility χ as functions of $\ln T$ in Figs. 4.11, 4.12, 4.13, 5.2, and 5.6. For convenience, we present them in the T-linear scale in Figs. B.1-B.5.

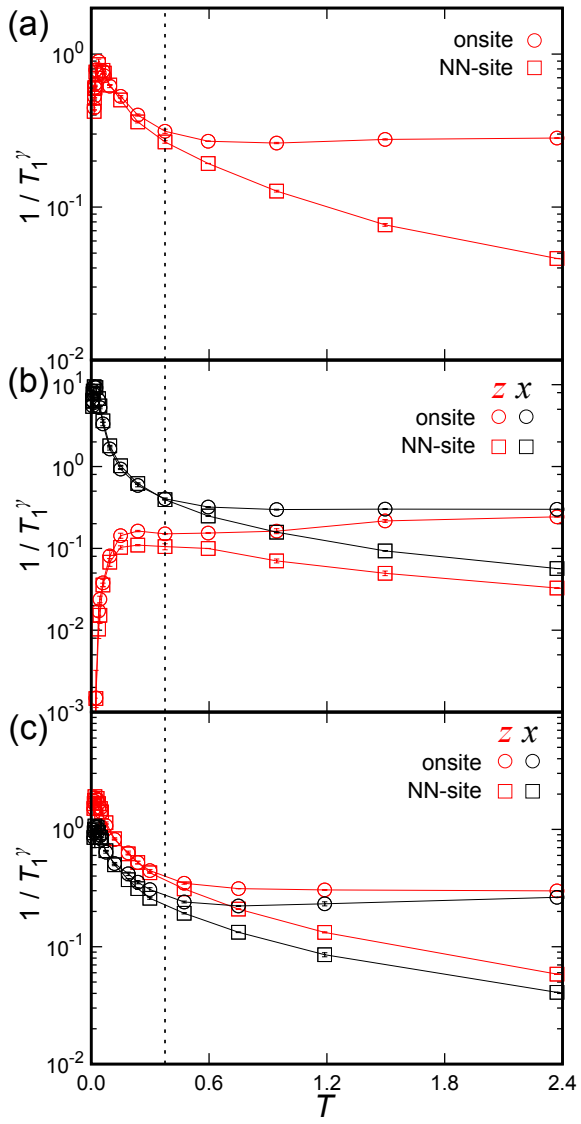

Figure B.1: The same plots as Fig. 4.11 in the main text in the T-linear scale. The vertical dotted line indicate $T_{\rm H}$ which is common for each α.

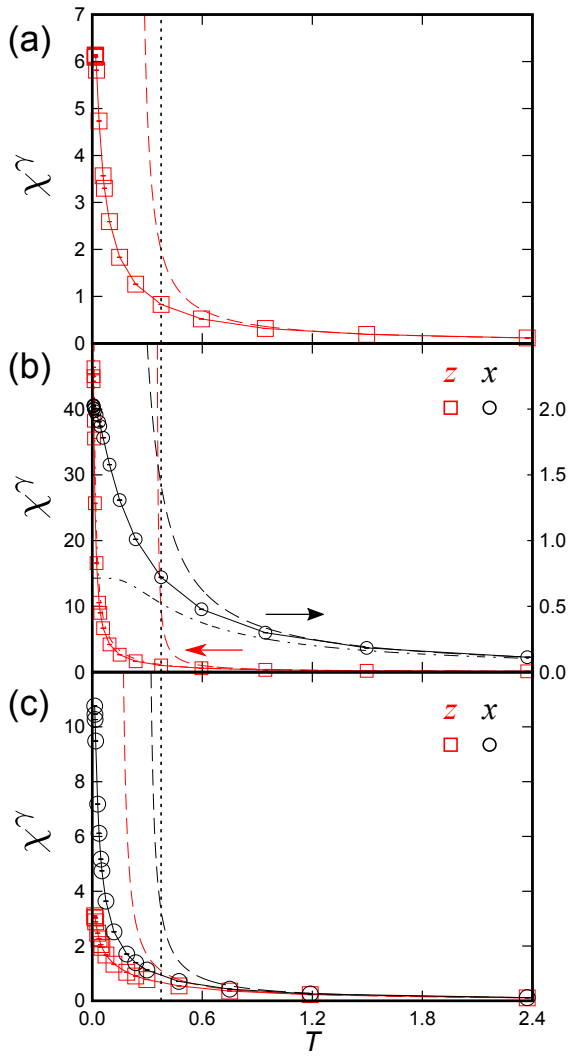

Figure B.2: The same plots as Fig. 4.12 in the main text in the T-linear scale. The vertical dotted line indicate $T_{\rm H}$ which is common for each α.

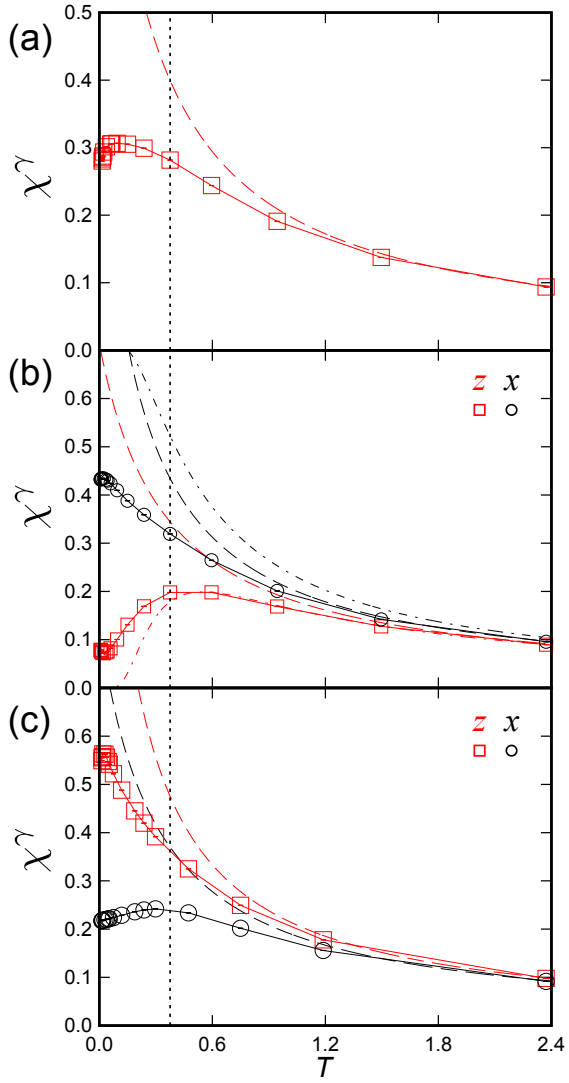

Figure B.3: The same plots as Fig. 4.13 in the main text in the T-linear scale. The vertical dotted line indicate $T_{\rm H}$ which is common for each α.

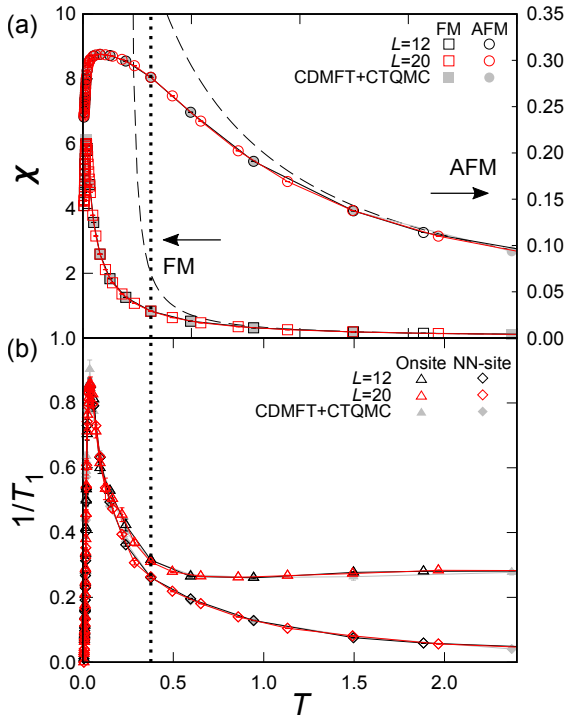

Figure B.4: The same plots as Fig. 5.2 in the main text in the T-linear scale. The vertical dotted line indicate $T_{\rm H}$.

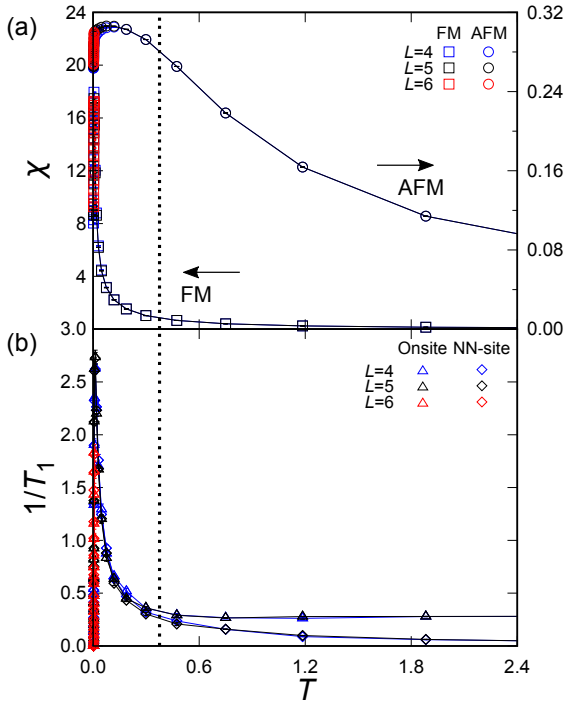

Figure B.5: The same plots as Fig. 5.5 in the main text in the T-linear scale. The vertical dotted line indicate $T_{\rm H}$.

C
Benchmark of the maximum entropy method

In Chaps. 4 and 5, we calculate $S^{\gamma}_{j,j'}(\omega)$ from $\langle S^{\gamma}_{j}(\tau)S^{\gamma}_{j'}\rangle$ by the MEM introduced in Sec. 3.4. In this Appendix, we examine the accuracy of the MEM by comparing $S^{\gamma}(\Gamma,\omega)$ at sufficiently low-T with the analytical solution in the ground state. We also examine the accuracy in the limit of decoupled one-dimensional chains, i.e., $\alpha = 1.5$ ($J_z = 0$), where $S^{\gamma}_{j,j'}(\omega)$ can be obtained directly without the MEM.

First, we examine the accuracy of the MEM for the data at sufficiently low T in comparison with the analytical solution in the ground state [98]. Figure C.1(a) shows $S^{z}(\Gamma,\omega)$ obtained by the Majorana QMC+CTQMC method for the FM case with $\alpha = 1.0$ at $T \simeq 0.0053$. The QMC+CTQMC result agrees well with the analytical solution in the ground state shown in Fig. C.1(b). In particular, the QMC+CTQMC result reproduces the characteristic features of the ground-state result; the two flux gap $\Delta \simeq 0.065$, the sharp peak at $\omega \simeq 0.1$, and the broad incoherent response extending to $\omega \simeq 1.5$.

Figure C.2 shows $S^{z}(\Gamma,\omega)$ obtained by the Majorana CDMFT+CTQMC method for the FM case with $\alpha = 0.8$ at $T = 0.003$. In the ground state, the energy required to flip a single η_r is $\Delta \simeq 0.042$ at $\alpha = 0.8$. Reflecting the flux gap, $S^{z}(\Gamma,\omega)$ at low T has a δ-function like peak at $\Delta \simeq 0.042$ [98]. As shown in Fig. C.2, our CDMFT+CTQMC result shows a peak at this energy, which is considered to precisely reproduce the low-energy structure of the dynamical spin structure factor.

Next, we show the comparison in the limit of decoupled one-dimensional chains, i.e., $\alpha = 1.5$ ($J_z = 0$). In this limit, the Kitaev Hamiltonian in Eq. (1.1) is written only by itinerant matter fermions $\{c\}$, in the form of Eq. (1.10) with $J_z = 0$. In this noninteracting problem, following Ref. [146], we can calculate $S^{x}_{j,j'}(\omega)$ by considering the real-time evolution (RTE) of $\langle S^{x}_{j}(t)S^{x}_{j'}\rangle$, instead of the imaginary-time correlation $\langle S^{x}_{j}(\tau)S^{x}_{j'}\rangle$, as

$$S^{x}_{j,j'}(\omega) = \int_{-\infty}^{\infty} dt e^{i\omega t - \epsilon|t|}\langle S^{x}_{j}(t)S^{x}_{j'}\rangle. \tag{C.1}$$

We call this method as the RTE in the following. In the RTE calculations, we consider an xy chain with 600 sites under the open boundary condition and take a sufficiently small $\epsilon = 0.04$ in Eq. (C.1).

On the other hand, $S^{z}_{j,j'}(\omega)$ has a nonzero value only for the onsite component, which is given by $4\langle S^{z}_{j}(\tau)S^{z}_{j}\rangle = \langle c_j(\tau)c_j\rangle$. Hence, $S^{z}_{j,j}(\omega)$ is obtained as

$$S^{z}_{j,j}(\omega) = \frac{1}{2(1+e^{-\beta\omega})}D(\omega), \tag{C.2}$$

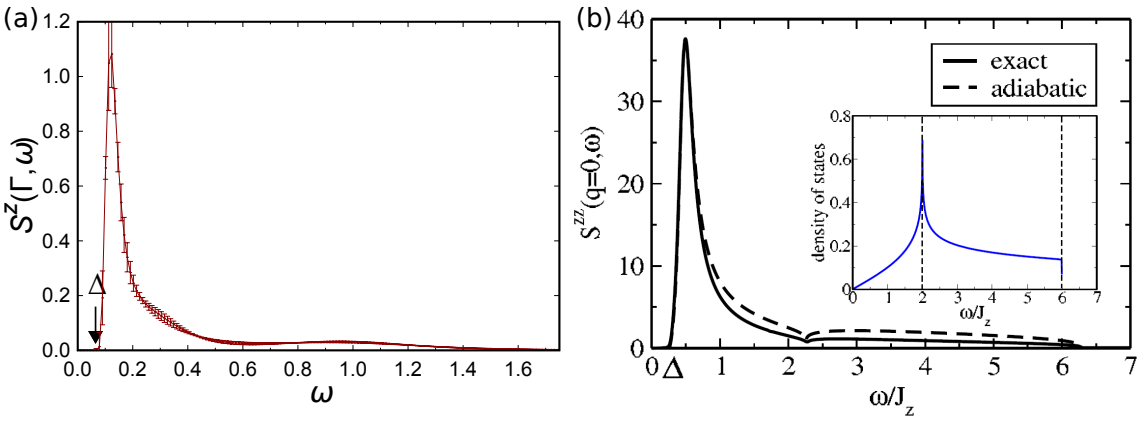

Figure C.1: (a) $S^z(\Gamma,\omega)$ obtained by the QMC+CTQMC method for the FM case with $\alpha = 1.0$ at $T \simeq 0.0053$. (b) Analytical result of $S^z(\Gamma,\omega)$ for the FM case with $\alpha = 1.0$ in the ground state (solid curve in the main panel). In (b), the value of $x(y)$ axis is multiplied by $4(12\pi)$ compared to that in (a) due to the different definition. The figure in (b) is taken from Ref. [90].

where $D(\omega)$ is the DOS for itinerant matter fermions in the one-dimensional limit:

$$D(\omega) = \frac{1}{\pi\sqrt{1.5^2 - \omega^2}}. \tag{C.3}$$

We call this method to estimate $S^z_{j,j}(\omega)$ the exact-DOS in the following.

Figure C.3 shows the results of $S^\gamma_{j,j'}(\omega)$ obtained by the MEM, RTE, and exact-DOS methods for the FM case with $\alpha = 1.5$ ($J_x = J_y = 1.5$ and $J_z = 0$). We present both onsite and NN-site components for $S^x_{j,j'}(\omega)$, while only the onsite one for $S^z_{j,j'}(\omega)$. We find that overall ω dependence of $S^\gamma_{j,j'}(\omega)$ is well reproduced by the MEM. In particular, the agreement is excellent in the low ω region; the growth of $S^x_{j,j'}(\omega = 0)$ on decreasing T, which contributes to $1/T_1$, is well reproduced by the MEM. On the other hand, the relatively sharp structures at $\omega \sim 1.5$ are blurred in the MEM results for both $\gamma = x$ and z, presumably because $\langle S^\gamma_j(\tau) S^\gamma_{j'}\rangle$ is more insensitive to $S^\gamma_{j,j'}(\omega)$ in the larger ω region. Nevertheless, as shown in Figs. C.3(e) and C.3(f), the MEM results reproduce the broad incoherent peak of $S^x_{j,j}(\omega) - S^x_{\rm NN}(\omega)$.

From these observations, we consider that the MEM results for $S(\mathbf{q},\omega)$ and $1/T_1$ in Chaps. 4 and 5 are accurate enough to discuss the T and ω dependences.

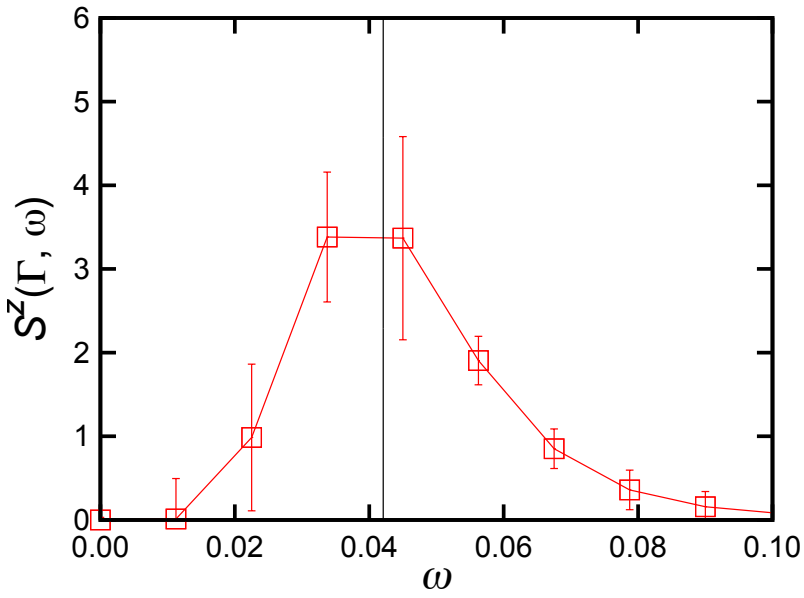

Figure C.2: $S^z(\Gamma, \omega)$ obtained by the Majorana CDMFT+CTQMC method for the FM case for $\alpha = 0.8$ at $T = 0.003$. Vertical line at $\omega \sim 0.042$ represents the value of flux gap of the ground state calculated exactly.

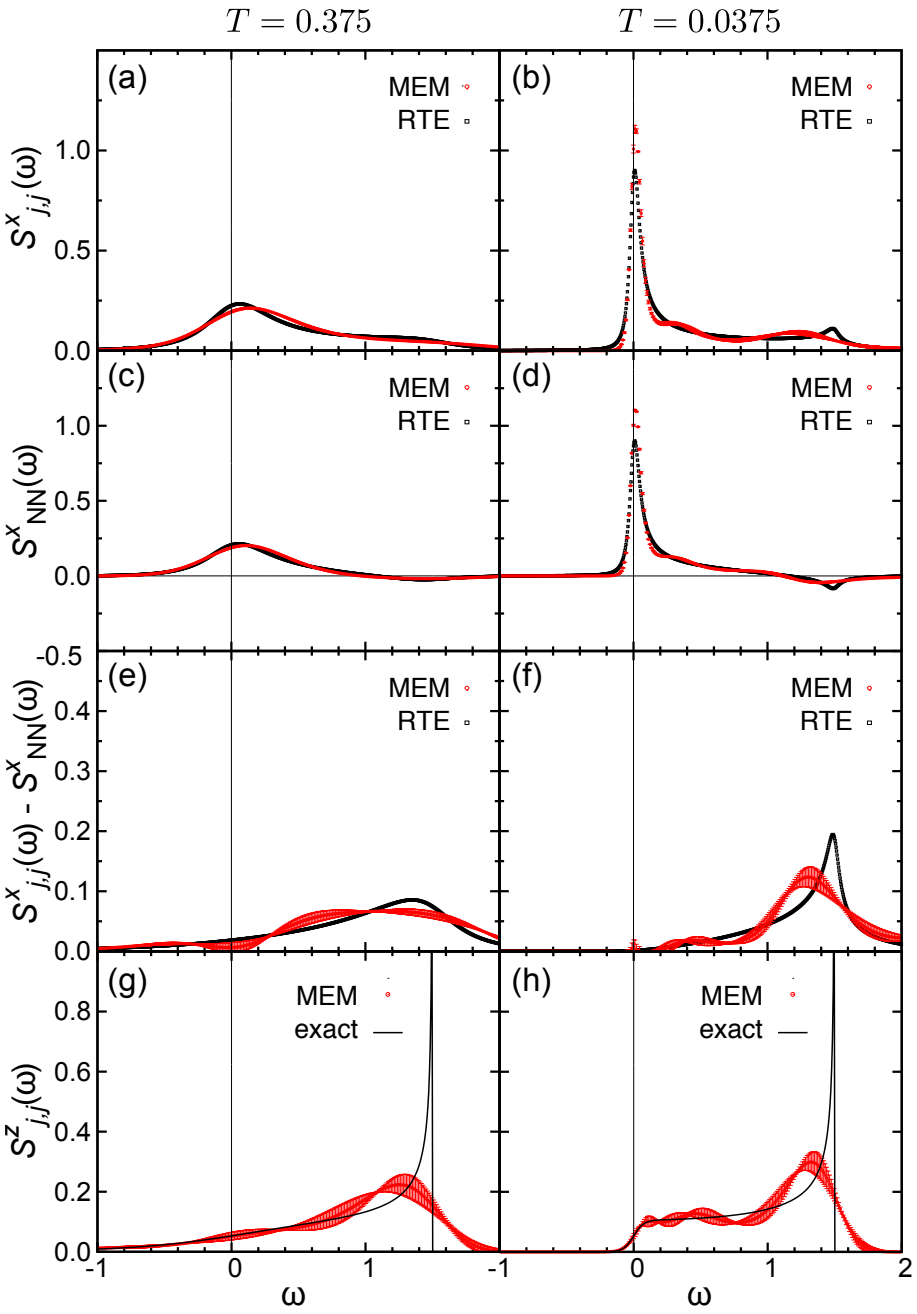

Figure C.3: Comparison between the MEM, RTE, and exact-DOS results for (a)(b) $S^x_{j,j}(\omega)$, (c)(d) $S^x_{\rm NN}(\omega)$, (e)(f) $S^x_{j,j}(\omega) - S^x_{\rm NN}(\omega)$, and (g)(h) $S^z_{j,j}(\omega)$ at (a)(c)(e)(g) $T = 0.375$ and (b)(d)(f)(h) $T = 0.0375$.

D
Low-T behavior of χ

In this Appendix, we examine the low-T asymptotic behavior of the magnetic susceptibility χ for the Kitaev model. In the gapped phase with the strong anisotropy of the interactions (see the ground-state phase diagram in Fig. 1.2), χ is expected to converge to the $T = 0$ value exponentially as both the flux and Majorana excitations are gapped. In fact, such behavior was analytically obtained in the anisotropic limit (the so-called toric code model) [31]. On the other hand, in the gapless phase where the anisotropy of the interactions is weak, gapless Majorana excitations possibly results in polynomial T dependence of χ at low T. As the dispersion of the Majorana fermions have Dirac cones, it is expected that the energy develops with T^3 at low T in the gapless phase. As χ^γ is given by Eq. (3.53), it is plausible that χ^γ has also T^3 dependence up to a constant.

To confirm the low-T asymptotic behaviors, we here numerically calculated χ in the subspace of $\{\eta_r = 1\}'$, $\chi^{\{\eta_r=1\}'}$, on the periodic lattice composed of 240^2 two-site unit cells in Fig. A.1. As the flux excitations are exponentially suppressed at low T, it is sufficient to consider only the subspace of $\{\eta_r = 1\}'$ for the current purpose.

Figure D.1 shows the result with the isotropic interactions $J_x = J_y = J_z = \pm 1$. For both FM and AFM cases, $\chi^{\{\eta_r=1\}'}$ converges to a nonzero value as $T \to 0$ below $T \simeq 0.02$. The convergence reflects the exponential suppression of the flux excitation of $\eta_{r_0} = -1$ for $T < \Delta$, where $\Delta \simeq 0.065$ is the two-flux excitation gap in the ground state [26, 98]. When examining the low-T data more closely, $\chi^{\{\eta_r=1\}'}$ for the FM case shows a peak at $T \simeq 0.0012$ and turns to decrease, as shown in Fig. D.1(b). The decrease at low T is expected to be associated with the Majorana excitations in the flux-free ground state. We test the least-square fitting by assuming $\chi^{\{\eta_r=1\}'} = C_0 + C_1 T^p$ with $p = 1$, 2, and 3 for the data at $T < 0.009$ where the contribution from the state with $\eta_{r_0} = -1$ is sufficiently small. Although the fitting with $p = 3$, which is expected from the above argument, appears to reproduce well the results, we cannot exclude the possibility of $p = 1$ and 2, as shown in Fig. D.1(b); root mean squares of the differences between the numerical results and fittings are 0.00039, 0.00031, and 0.00027 for $p = 1$, 2, and 3 respectively. For the AFM case, we only observe monotonic decrease of $\chi^{\{\eta_r=1\}'}$ in the low-T region as shown in Fig. D.1(c). In this case, the similar power-law fitting for the data at $T < 0.009$ does not reproduce the results for all p, as shown in Fig. D.1(c). The reason is not clear, but we may need further lower-T data for the analysis.

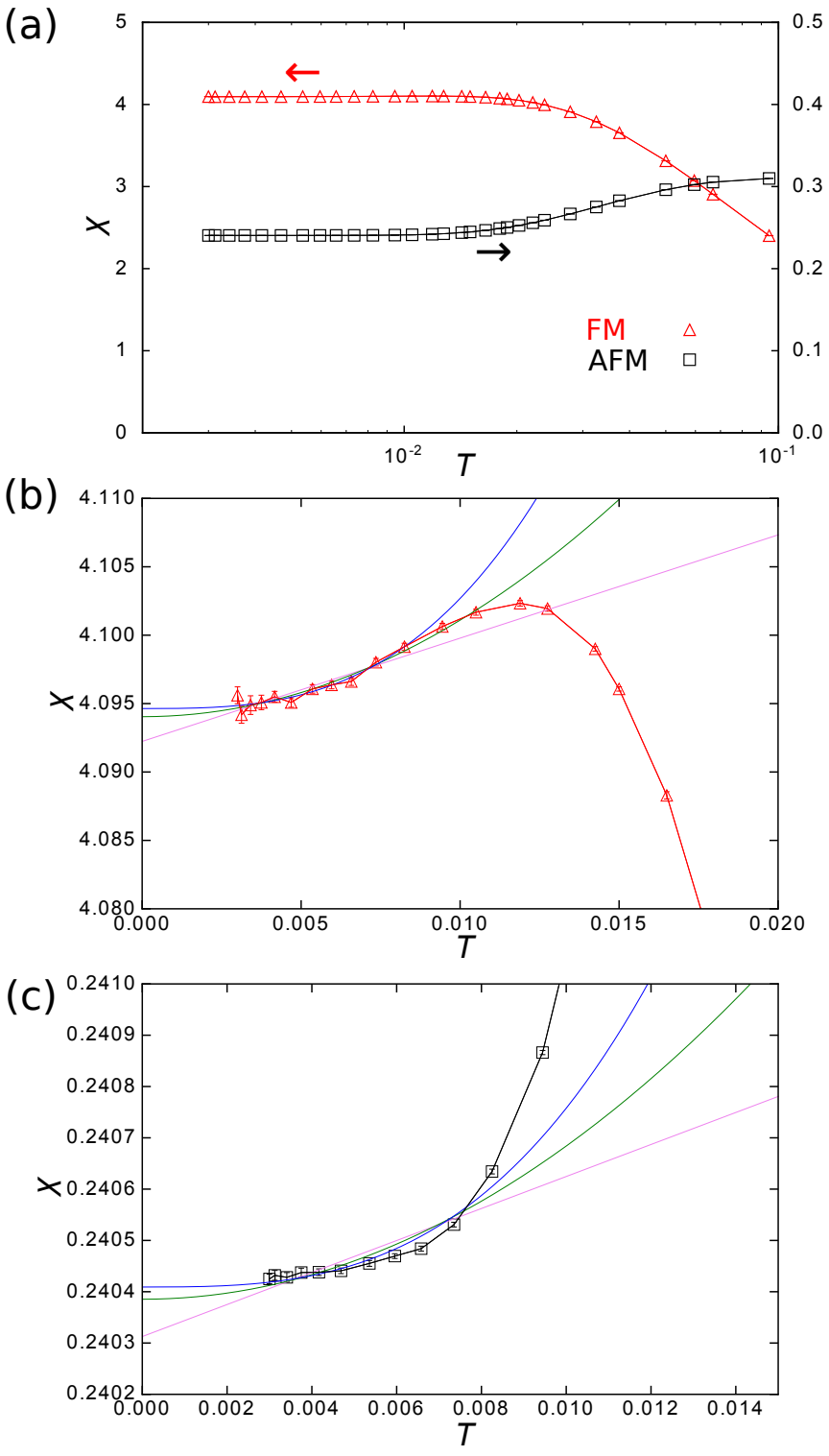

Figure D.1: (a) T dependences of $\chi^{\{\eta_r=1\}'}$ for the FM and AFM cases. (b) and (c) Low-T behaviors of $\chi^{\{\eta_r=1\}'}$ for the (b) FM and (c) AFM cases. The magenta, green, and blue curves represent the fitting results by assuming $\chi^{\{\eta_r=1\}'} = C_0 + C_1 T^p$ with $p = 1$, 2, and 3, respectively.

E

Convergence of the hybridization expansion in QMC+CTQMC calculations

In this Appendix, we discuss the convergence of the QMC+CTQMC calculations with respect to the expansion order d in Eq. (3.34). For this purpose, we examine the histogram of d obtained in the QMC+CTQMC calculations. We calculate the histogram $P(d)$ by taking the Monte Carlo average of $P(d)^{\{\eta_r\}'}$, which is the histogram obtained in the CTQMC calculation for a given $\{\eta_r\}'$, as

$$P(d) = \frac{1}{N_{\rm MC}} \sum_{\{\eta_r\}' \in \text{MC samples}} P(d)^{\{\eta_r\}'}, \tag{E.1}$$

where $N_{\rm MC}$ is the number of the Monte Carlo samples. Note that $P(d)$ are normalized so that $\sum_d P(d) = 1$.

Figure E.1 shows the results of the histograms. While $P(d)$ is localized around $d = 0$ at sufficiently high $T \simeq 0.94$, it shifts to a larger d region on decreasing T. At each T, $P(d)$ has a single peak structure, and decays quickly away from the peak. The maximum values of d appearing our CTQMC sampling are $d = 5$, 15, 37, and 66 for $T \simeq 0.94$, 0.094, 0.019, and 0.0083, respectively. In the CTQMC calculations, as described in Sec. 3.3, we set the cutoff for d as $d_{\rm cutoff} = 25 + 1.125 * \beta$. The results above indicate that the cutoff values are large enough to ensure the convergence of the CTQMC calculations.

In the hybridization expansion, the Monte Carlo average of the expansion order is related with the kinetic energy connecting the impurity sites and bath [147]. In the present case for the Kitaev model, for each CTQMC calculation for a given $\{\eta_r\}'$, we obtain

$$\begin{aligned} 2\langle d\rangle^{\{\eta_r\}'} = \beta(&J_x(\langle S^x_j S^x_{j''}\rangle^{\{\eta_r\}'} + \langle S^x_{j'} S^x_{j'''}\rangle^{\{\eta_r\}'}) \\ &+ J_y(\langle S^y_j S^y_{j''''}\rangle^{\{\eta_r\}'} + \langle S^y_{j'} S^y_{j'''''}\rangle^{\{\eta_r\}'})), \end{aligned} \tag{E.2}$$

where j and j' are the sites on the z bond r_0, whereas $j''(j'''')$ and $j'''(j''''')$ are the neighboring sites of j and j' connected by the x (y) bond, respectively. When the negative sign problem is negligible, the Monte Carlo average of the expansion order $\langle d\rangle^{\{\eta_r\}'}$ coincides with the center of mass of the histogram $\sum_d dP(d)^{\{\eta_r\}'}$. In the calculations in Fig. E.1, the negative sign is almost negligible; the ratio of the negative sign is less than 10^{-5} for $T \simeq 0.083$ and $T \simeq 0.019$, and practically zero for $T \simeq 0.94$ and $T \simeq 0.094$. Thus, we replace $\langle d\rangle^{\{\eta_r\}'}$ in Eq. (E.2) with $\sum_d dP(d)^{\{\eta_r\}'}$,

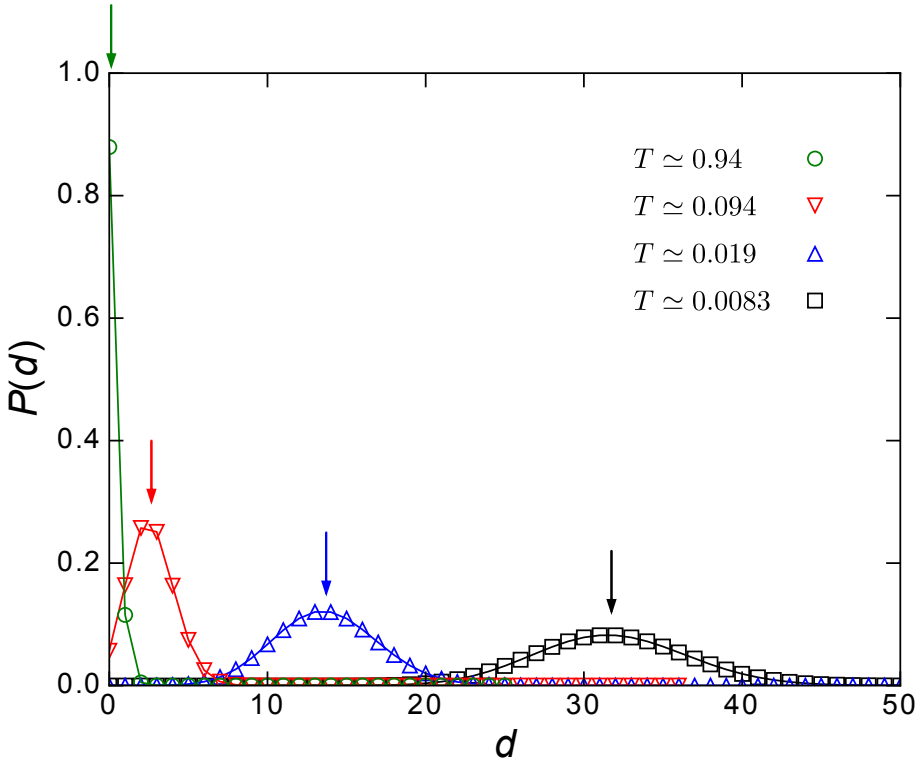

Figure E.1: Histogram of the expansion order d in the QMC+CTQMC calculations. The results for Eq. (E.1) are shown for several T. The arrows indicate the values of right hand side of Eq. (E.3) at each T.

by neglecting the negative sign problem. Then, we obtain

$$\sum_d dP(d) = \beta(J_x\langle S_j^x S_{j'}^x\rangle_{\rm NN} + J_y\langle S_j^y S_{j'}^y\rangle_{\rm NN}). \tag{E.3}$$

This relation is readily seen in Fig. E.1; the values of the right hand side of Eq. (E.3) are indicated by the arrows, whose locations well coincide with the peak positions of the histograms $P(d)$.

References

[1] P. Anderson, Materials Research Bulletin **8**, 153 (1973).

[2] X. G. Wen, Phys. Rev. B **40**, 7387 (1989).

[3] X. G. WEN, International Journal of Modern Physics B **04**, 239 (1990).

[4] X. G. Wen and Q. Niu, Phys. Rev. B **41**, 9377 (1990).

[5] D. C. Tsui, H. L. Stormer, and A. C. Gossard, Phys. Rev. Lett. **48**, 1559 (1982).

[6] X.-G. Wen, Advances in Physics **44**, 405 (1995).

[7] M. Oshikawa and T. Senthil, Phys. Rev. Lett. **96**, 060601 (2006).

[8] S. A. Kivelson, D. S. Rokhsar, and J. P. Sethna, Phys. Rev. B **35**, 8865 (1987).

[9] T. Senthil and M. P. A. Fisher, Phys. Rev. B **62**, 7850 (2000).

[10] P. W. ANDERSON, Science **235**, 1196 (1987).

[11] P. A. Lee, Science **321**, 1306 (2008).

[12] L. Balents, Nature **464**, 199 (2010).

[13] Y. Shimizu, K. Miyagawa, K. Kanoda, M. Maesato, and G. Saito, Phys. Rev. Lett. **91**, 107001 (2003).

[14] T. Itou, A. Oyamada, S. Maegawa, M. Tamura, and R. Kato, Phys. Rev. B **77**, 104413 (2008).

[15] Z. Hiroi, M. Hanawa, N. Kobayashi, M. Nohara, H. Takagi, Y. Kato, and M. Takigawa, Journal of the Physical Society of Japan **70**, 3377 (2001).

[16] M. P. Shores, E. A. Nytko, B. M. Bartlett, and D. G. Nocera, Journal of the American Chemical Society **127**, 13462 (2005).

[17] Y. Okamoto, H. Yoshida, and Z. Hiroi, Journal of the Physical Society of Japan **78**, 033701 (2009).

[18] Y. Okamoto, M. Nohara, H. Aruga-Katori, and H. Takagi, Phys. Rev. Lett. **99**, 137207 (2007).

[19] Y. Zhou, K. Kanoda, and T.-K. Ng, Rev. Mod. Phys. **89**, 025003 (2017).

[20] L. Savary and L. Balents, Reports on Progress in Physics **80**, 016502 (2017).

[21] K. I. Kugel ' and D. I. Khomskii, Phys. Usp. **25**, 231 (1982).

[22] D. I. Khomskii and M. V. Mostovoy, Journal of Physics A: Mathematical and General **36**, 9197 (2003).

[23] G. Khaliullin, Progress of Theoretical Physics Supplement **160**, 155 (2005).

[24] Z. Nussinov and J. van den Brink, Rev. Mod. Phys. **87**, 1 (2015).

[25] A. M. Oleś, Acta Phys. Polon. A. **127**, 163 (2015).

[26] A. Kitaev, Annals of Physics **321**, 2 (2006).

[27] G. Jackeli and G. Khaliullin, Phys. Rev. Lett. **102**, 017205 (2009).

[28] E. H. Lieb, Phys. Rev. Lett. **73**, 2158 (1994).

[29] G. Baskaran, S. Mandal, and R. Shankar, Phys. Rev. Lett. **98**, 247201 (2007).

[30] H. Yao and S. A. Kivelson, Phys. Rev. Lett. **99**, 247203 (2007).

[31] J. Nasu, T. Kaji, K. Matsuura, M. Udagawa, and Y. Motome, Phys. Rev. B **89**, 115125 (2014).

[32] M. Hermanns and S. Trebst, Phys. Rev. B **89**, 235102 (2014).

[33] M. Hermanns, K. O'Brien, and S. Trebst, Phys. Rev. Lett. **114**, 157202 (2015).

[34] J. Nasu and Y. Motome, Physics Procedia **75**, 755 (2015).

[35] K. O'Brien, M. Hermanns, and S. Trebst, Phys. Rev. B **93**, 085101 (2016).

[36] J. Nasu and Y. Motome, Journal of Physics: Conference Series **683**, 012037 (2016).

[37] P. A. Mishchenko, Y. Kato, and Y. Motome, Phys. Rev. B **96**, 125124 (2017).

[38] B. J. Kim, H. Jin, S. J. Moon, J.-Y. Kim, B.-G. Park, C. S. Leem, J. Yu, T. W. Noh, C. Kim, S.-J. Oh, J.-H. Park, V. Durairaj, G. Cao, and E. Rotenberg, Phys. Rev. Lett. **101**, 076402 (2008).

[39] K. Foyevtsova, H. O. Jeschke, I. I. Mazin, D. I. Khomskii, and R. Valentí, Phys. Rev. B **88**, 035107 (2013).

[40] V. M. Katukuri, S. Nishimoto, V. Yushankhai, A. Stoyanova, H. Kandpal, S. Choi, R. Coldea, I. Rousochatzakis, L. Hozoi, and J. van den Brink, New Journal of Physics **16**, 013056 (2014).

[41] Y. Yamaji, Y. Nomura, M. Kurita, R. Arita, and M. Imada, Phys. Rev. Lett. **113**, 107201 (2014).

[42] H.-S. Kim and H.-Y. Kee, Phys. Rev. B **93**, 155143 (2016).

[43] S. M. Winter, Y. Li, H. O. Jeschke, and R. Valentí, Phys. Rev. B **93**, 214431 (2016).

[44] R. Sano, Y. Kato, and Y. Motome, Phys. Rev. B **97**, 014408 (2018).

[45] H. Liu and G. Khaliullin, Phys. Rev. B **97**, 014407 (2018).

[46] F.-Y. Li, Y.-D. Li, Y. Yu, A. Paramekanti, and G. Chen, Phys. Rev. B **95**, 085132 (2017).

[47] J. G. Rau and M. J. P. Gingras, Phys. Rev. B **98**, 054408 (2018).

[48] S.-H. Jang, R. Sano, Y. Kato, and Y. Motome, arXiv:1807.01443.

[49] J. Chaloupka, G. Jackeli, and G. Khaliullin, Phys. Rev. Lett. **105**, 027204 (2010).

[50] J. Chaloupka, G. Jackeli, and G. Khaliullin, Phys. Rev. Lett. **110**, 097204 (2013).

[51] J. G. Rau, E. K.-H. Lee, and H.-Y. Kee, Phys. Rev. Lett. **112**, 077204 (2014).

[52] P. Schmoll and R. Orús, Phys. Rev. B **95**, 045112 (2017).

[53] T. Okubo, K. Shinjo, Y. Yamaji, N. Kawashima, S. Sota, T. Tohyama, and M. Imada, Phys. Rev. B **96**, 054434 (2017).

[54] M. Gohlke, R. Verresen, R. Moessner, and F. Pollmann, Phys. Rev. Lett. **119**, 157203 (2017).

[55] Y. Singh and P. Gegenwart, Phys. Rev. B **82**, 064412 (2010).

[56] Y. Singh, S. Manni, J. Reuther, T. Berlijn, R. Thomale, W. Ku, S. Trebst, and P. Gegenwart, Phys. Rev. Lett. **108**, 127203 (2012).

[57] R. Comin, G. Levy, B. Ludbrook, Z.-H. Zhu, C. N. Veenstra, J. A. Rosen, Y. Singh, P. Gegenwart, D. Stricker, J. N. Hancock, D. van der Marel, I. S. Elfimov, and A. Damascelli, Phys. Rev. Lett. **109**, 266406 (2012).

[58] H. Gretarsson, J. P. Clancy, X. Liu, J. P. Hill, E. Bozin, Y. Singh, S. Manni, P. Gegenwart, J. Kim, A. H. Said, D. Casa, T. Gog, M. H. Upton, H.-S. Kim, J. Yu, V. M. Katukuri, L. Hozoi, J. van den Brink, and Y.-J. Kim, Phys. Rev. Lett. **110**, 076402 (2013).

[59] S. Hwan Chun, J.-W. Kim, J. Kim, H. Zheng, C. Stoumpos, C. . D. Malliakas, J. . F. Mitchell, K. Mehlawat, Y. Singh, Y. Choi, T. Gog, A. Al-Zein, M. M. Sala, M. Krisch, J. Chaloupka, G. Jackeli, G. Khaliullin, and B. J. Kim, Nature Physics **11**, 462 (2015).

[60] X. Liu, T. Berlijn, W.-G. Yin, W. Ku, A. Tsvelik, Y.-J. Kim, H. Gretarsson, Y. Singh, P. Gegenwart, and J. P. Hill, Phys. Rev. B **83**, 220403 (2011).

[61] F. Ye, S. Chi, H. Cao, B. C. Chakoumakos, J. A. Fernandez-Baca, R. Custelcean, T. F. Qi, O. B. Korneta, and G. Cao, Phys. Rev. B **85**, 180403 (2012).

[62] S. C. Williams, R. D. Johnson, F. Freund, S. Choi, A. Jesche, I. Kimchi, S. Manni, A. Bombardi, P. Manuel, P. Gegenwart, and R. Coldea, Phys. Rev. B **93**, 195158 (2016).

[63] K. Kitagawa, T. Takayama, Y. Matsumoto, A. Kato, R. Takano, Y. Kishimoto, S. Bette, R. Dinnebier, G. Jackeli, and H. Takagi, Nature **554**, 341 (2018).

[64] K. Slagle, W. Choi, L. E. Chern, and Y. B. Kim, Phys. Rev. B **97**, 115159 (2018).

[65] I. Kimchi, J. P. Sheckelton, T. M. McQueen, and P. A. Lee, Nature Communications **9**, 4367 (2018).

[66] J. Knolle, R. Moessner, and N. B. Perkins, arXiv:1807.09670.

[67] K. W. Plumb, J. P. Clancy, L. J. Sandilands, V. V. Shankar, Y. F. Hu, K. S. Burch, H.-Y. Kee, and Y.-J. Kim, Phys. Rev. B **90**, 041112 (2014).

[68] A. Koitzsch, C. Habenicht, E. Müller, M. Knupfer, B. Büchner, H. C. Kandpal, J. van den Brink, D. Nowak, A. Isaeva, and T. Doert, Phys. Rev. Lett. **117**, 126403 (2016).

[69] S. Sinn, C. H. Kim, B. H. Kim, K. D. Lee, C. J. Won, J. S. Oh, M. Han, Y. J. Chang, N. Hur, H. Sato, B.-G. Park, C. Kim, H.-D. Kim, and T. W. Noh, Scientific Reports **6**, 39544 (2016).

[70] Y. Kubota, H. Tanaka, T. Ono, Y. Narumi, and K. Kindo, Phys. Rev. B **91**, 094422 (2015).

[71] J. A. Sears, M. Songvilay, K. W. Plumb, J. P. Clancy, Y. Qiu, Y. Zhao, D. Parshall, and Y.-J. Kim, Phys. Rev. B **91**, 144420 (2015).

[72] R. D. Johnson, S. C. Williams, A. A. Haghighirad, J. Singleton, V. Zapf, P. Manuel, I. I. Mazin, Y. Li, H. O. Jeschke, R. Valentí, and R. Coldea, Phys. Rev. B **92**, 235119 (2015).

[73] H. B. Cao, A. Banerjee, J.-Q. Yan, C. A. Bridges, M. D. Lumsden, D. G. Mandrus, D. A. Tennant, B. C. Chakoumakos, and S. E. Nagler, Phys. Rev. B **93**, 134423 (2016).

[74] S.-H. Do, S.-Y. Park, J. Yoshitake, J. Nasu, Y. Motome, Y. Kwon, D. T. Adroja, D. J. Voneshen, K. Kim, T.-H. Jang, J.-H. Park, K.-Y. Choi, and S. Ji, Nature Physics **13**, 1079 (2017).

[75] M. Ziatdinov, A. Banerjee, A. Maksov, T. Berlijn, W. Zhou, H. B. Cao, J.-Q. Yan, C. A. Bridges, D. G. Mandrus, S. E. Nagler, A. P. Baddorf, and S. V. Kalinin, Nature Communications **7**, 13774 (2016).

[76] B. Zhou, Y. Wang, G. B. Osterhoudt, P. Lampen-Kelley, D. Mandrus, R. He, K. S. Burch, and E. A. Henriksen, Journal of Physics and Chemistry of Solids (2018), https://doi.org/10.1016/j.jpcs.2018.01.026.

[77] R. Yadav, N. A. Bogdanov, V. M. Katukuri, S. Nishimoto, J. van den Brink, and L. Hozoi, Scientific Reports **6**, 37925 (2016).

[78] I. A. Leahy, C. A. Pocs, P. E. Siegfried, D. Graf, S.-H. Do, K.-Y. Choi, B. Normand, and M. Lee, Phys. Rev. Lett. **118**, 187203 (2017).

[79] A. U. B. Wolter, L. T. Corredor, L. Janssen, K. Nenkov, S. Schönecker, S.-H. Do, K.-Y. Choi, R. Albrecht, J. Hunger, T. Doert, M. Vojta, and B. Büchner, Phys. Rev. B **96**, 041405 (2017).

[80] S.-H. Baek, S.-H. Do, K.-Y. Choi, Y. S. Kwon, A. U. B. Wolter, S. Nishimoto, J. van den Brink, and B. Büchner, Phys. Rev. Lett. **119**, 037201 (2017).

[81] J. Zheng, K. Ran, T. Li, J. Wang, P. Wang, B. Liu, Z.-X. Liu, B. Normand, J. Wen, and W. Yu, Phys. Rev. Lett. **119**, 227208 (2017).

[82] R. Hentrich, A. U. B. Wolter, X. Zotos, W. Brenig, D. Nowak, A. Isaeva, T. Doert, A. Banerjee, P. Lampen-Kelley, D. G. Mandrus, S. E. Nagler, J. Sears, Y.-J. Kim, B. Büchner, and C. Hess, Phys. Rev. Lett. **120**, 117204 (2018).

[83] Y. Kasahara, K. Sugii, T. Ohnishi, M. Shimozawa, M. Yamashita, N. Kurita, H. Tanaka, J. Nasu, Y. Motome, T. Shibauchi, and Y. Matsuda, Phys. Rev. Lett. **120**, 217205 (2018).

[84] Z. Zhu, I. Kimchi, D. N. Sheng, and L. Fu, Phys. Rev. B **97**, 241110 (2018).

[85] P. A. McClarty, X.-Y. Dong, M. Gohlke, J. G. Rau, F. Pollmann, R. Moessner, and K. Penc, Phys. Rev. B **98**, 060404 (2018).

[86] T. Takayama, A. Kato, R. Dinnebier, J. Nuss, H. Kono, L. S. I. Veiga, G. Fabbris, D. Haskel, and H. Takagi, Phys. Rev. Lett. **114**, 077202 (2015).

[87] K. A. Modic, T. E. Smidt, I. Kimchi, N. P. Breznay, A. Biffin, S. Choi, R. D. Johnson, R. Coldea, P. Watkins-Curry, G. T. McCandless, J. Y. Chan, F. Gandara, Z. Islam, A. Vishwanath, A. Shekhter, R. D. McDonald, and J. G. Analytis, Nature Communications **5**, 4203 (2014).

[88] A. Biffin, R. D. Johnson, S. Choi, F. Freund, S. Manni, A. Bombardi, P. Manuel, P. Gegenwart, and R. Coldea, Phys. Rev. B **90**, 205116 (2014).

[89] A. Biffin, R. D. Johnson, I. Kimchi, R. Morris, A. Bombardi, J. G. Analytis, A. Vishwanath, and R. Coldea, Phys. Rev. Lett. **113**, 197201 (2014).

[90] J. Nasu, M. Udagawa, and Y. Motome, Phys. Rev. Lett. **113**, 197205 (2014).

[91] J. Nasu, M. Udagawa, and Y. Motome, Phys. Rev. B **92**, 115122 (2015).

[92] K. Mehlawat, A. Thamizhavel, and Y. Singh, Phys. Rev. B **95**, 144406 (2017).

[93] L. J. Sandilands, C. H. Sohn, H. J. Park, S. Y. Kim, K. W. Kim, J. A. Sears, Y.-J. Kim, and T. W. Noh, Phys. Rev. B **94**, 195156 (2016).

[94] G. Khaliullin, P. Horsch, and A. M. Oleś, Phys. Rev. B **70**, 195103 (2004).

[95] L. J. Sandilands, Y. Tian, K. W. Plumb, Y.-J. Kim, and K. S. Burch, Phys. Rev. Lett. **114**, 147201 (2015).

[96] A. Banerjee, C. A. Bridges, J.-Q. Yan, A. A. Aczel, L. Li, M. B. Stone, G. E. Granroth, M. D. Lumsden, Y. Yiu, J. Knolle, S. Bhattacharjee, D. L. Kovrizhin, R. Moessner, D. A. Tennant, D. G. Mandrus, and S. E. Nagler, Nature Materials **15**, 733 (2016).

[97] J. Nasu, J. Knolle, D. . L. Kovrizhin, Y. Motome, and R. Moessner, Nature Physics **12**, 912 (2016).

[98] J. Knolle, D. L. Kovrizhin, J. T. Chalker, and R. Moessner, Phys. Rev. Lett. **112**, 207203 (2014).

[99] A. Banerjee, J. Yan, J. Knolle, C. A. Bridges, M. B. Stone, M. D. Lumsden, D. G. Mandrus, D. A. Tennant, R. Moessner, and S. E. Nagler, Science **356**, 1055 (2017).

[100] P. A. Fleury and R. Loudon, Phys. Rev. **166**, 514 (1968).

[101] B. S. Shastry and B. I. Shraiman, Phys. Rev. Lett. **65**, 1068 (1990).

[102] J. Knolle, G.-W. Chern, D. L. Kovrizhin, R. Moessner, and N. B. Perkins, Phys. Rev. Lett. **113**, 187201 (2014).

[103] B. Perreault, J. Knolle, N. B. Perkins, and F. J. Burnell, Phys. Rev. B **92**, 094439 (2015).

[104] A. Glamazda, P. Lemmens, S.-H. Do, Y. S. Choi, and K.-Y. Choi, Nature Communications **7**, 12286 (2016).

[105] N. Furukawa, Journal of the Physical Society of Japan **63**, 3214 (1994).

[106] G. Kotliar, S. Y. Savrasov, G. Pálsson, and G. Biroli, Phys. Rev. Lett. **87**, 186401 (2001).

[107] J. Nilsson and M. Bazzanella, Phys. Rev. B **88**, 045112 (2013).

[108] W. Metzner and D. Vollhardt, Phys. Rev. Lett. **62**, 324 (1989).

[109] A. Georges, G. Kotliar, W. Krauth, and M. J. Rozenberg, Rev. Mod. Phys. **68**, 13 (1996).

[110] M. Udagawa, H. Ishizuka, and Y. Motome, Phys. Rev. Lett. **108**, 066406 (2012).

[111] P. Werner, A. Comanac, L. de' Medici, M. Troyer, and A. J. Millis, Phys. Rev. Lett. **97**, 076405 (2006).

[112] Z.-X. Li, Y.-F. Jiang, and H. Yao, Phys. Rev. B **91**, 241117 (2015).

[113] A. N. Rubtsov, V. V. Savkin, and A. I. Lichtenstein, Phys. Rev. B **72**, 035122 (2005).

[114] L. Boehnke, H. Hafermann, M. Ferrero, F. Lechermann, and O. Parcollet, Phys. Rev. B **84**, 075145 (2011).

[115] R. Levy, J. LeBlanc, and E. Gull, Computer Physics Communications **215**, 149 (2017).

[116] W. H. Press, S. A. Teukolsky, W. T. Vetterling, and B. P. Flannery, Numerical Recipes in C (2Nd Ed.): The Art of Scientific Computing (Cambridge University Press, New York, NY, USA, 1992).

[117] M. Jarrell and J. Gubernatis, Physics Reports **269**, 133 (1996).

[118] $S^p_{\rm NN}(\omega)$ for the FM case ($S^p_{\rm NN}(\omega)_{\rm FM}$) and the AFM case ($S^p_{\rm NN}(\omega)_{\rm AFM}$) satisfy the relation $S^p_{\rm NN}(\omega)_{\rm FM} = -S^p_{\rm NN}(\omega)_{\rm AFM}$. Nevertheless, $S^p_{\rm NN}(\omega)_{\rm FM}$ and $S^p_{\rm NN}(\omega)_{\rm AFM}$ obtained by the present numerical procedure violates the relation because of the precision of the MEM. In the data presented in Chaps. 4 and 5, we calculate $S^p_{\rm NN}(\omega)_{\rm FM}$ by the procedure, and $S^p_{j,j'}(\omega)_{\rm AFM}$ are set as $S^p_{j,j'}(\omega)_{\rm AFM} = -S^p_{j,j'}(\omega)_{\rm FM}$.

[119] T. Moriya, Progress of Theoretical Physics **16**, 641 (1956).

[120] J. Yoshitake, J. Nasu, and Y. Motome, Phys. Rev. Lett. **117**, 157203 (2016).

[121] χ^x for the AFM case at $\alpha = 0.8$ also shows similar behavior, but it is qualitatively explained by the Curie-Weiss law in Eq. (4.2) for this case.

[122] Thermal averages $\langle \eta_{r_0} \rangle$ obtained by the CTQMC calculations deviate from 1 even in the uniform case, although we fix $P(\eta_{r_0} = 1) = 1$ in the CDMFT. This is because the statistical weight of $\eta_{r_0} = -1$ is nonzero in the two-site impurity problem in the CTQMC calculations. Such a discrepancy of $\langle \eta_{r_0} \rangle$ between the CDMFT and CTQMC solutions never occurs when we do not fix $P(\eta_{r_0})$ by hand.

[123] D. Hirobe, M. Sato, Y. Shiomi, H. Tanaka, and E. Saitoh, Phys. Rev. B **95**, 241112 (2017).

[124] J. Yoshitake, J. Nasu, Y. Kato, and Y. Motome, Phys. Rev. B **96**, 024438 (2017).

[125] J. Nasu, J. Yoshitake, and Y. Motome, Phys. Rev. Lett. **119**, 127204 (2017).

[126] N. P. Breznay, A. Ruiz, A. Frano, W. Bi, R. J. Birgeneau, D. Haskel, and J. G. Analytis, Phys. Rev. B **96**, 020402 (2017).

[127] A. Ruiz, A. Frano, N. P. Breznay, I. Kimchi, T. Helm, I. Oswald, J. Y. Chan, R. J. Birgeneau, Z. Islam, and J. G. Analytis, Nature Communications **8**, 961 (2017).

[128] P. Lampen-Kelley, A. Banerjee, A. A. Aczel, H. B. Cao, M. B. Stone, C. A. Bridges, J.-Q. Yan, S. E. Nagler, and D. Mandrus, Phys. Rev. Lett. **119**, 237203 (2017).

[129] A. Smith, J. Knolle, D. L. Kovrizhin, J. T. Chalker, and R. Moessner, Phys. Rev. B **92**, 180408 (2015).

[130] G. Baskaran, D. Sen, and R. Shankar, Phys. Rev. B **78**, 115116 (2008).

[131] C. Price and N. B. Perkins, Phys. Rev. B **88**, 024410 (2013).

[132] A. M. Samarakoon, A. Banerjee, S.-S. Zhang, Y. Kamiya, S. E. Nagler, D. A. Tennant, S.-H. Lee, and C. D. Batista, Phys. Rev. B **96**, 134408 (2017).

[133] J. Reuther, R. Thomale, and S. Trebst, Phys. Rev. B **84**, 100406 (2011).

[134] J. Reuther and P. Wölfle, Phys. Rev. B **81**, 144410 (2010).

[135] R. R. P. Singh and J. Oitmaa, Phys. Rev. B **96**, 144414 (2017).

[136] Y. Yamaji, T. Suzuki, and M. Kawamura, arXiv:1802.02854.

[137] M. Udagawa, Phys. Rev. B **98**, 220404 (2018).

[138] K. Ran, J. Wang, W. Wang, Z.-Y. Dong, X. Ren, S. Bao, S. Li, Z. Ma, Y. Gan, Y. Zhang, J. T. Park, G. Deng, S. Danilkin, S.-L. Yu, J.-X. Li, and J. Wen, Phys. Rev. Lett. **118**, 107203 (2017).

[139] A. Banerjee, P. Lampen-Kelley, J. Knolle, C. Balz, A. A. Aczel, B. Winn, Y. Liu, D. Pajerowski, J. Yan, C. A. Bridges, A. T. Savici, B. C. Chakoumakos, M. D. Lumsden, D. A. Tennant, R. Moessner, D. G. Mandrus, and S. E. Nagler, npj Quantum Materials **3**, 8 (2018).

[140] N. Janša, A. Zorko, M. Gomilšek, M. Pregelj, K. W. Krämer, D. Biner, A. Biffin, C. Rüegg, and M. Klanjšek, Nature Physics **14**, 786 (2018).

[141] Y. Nagai, T. Jinno, Y. Yoshitake, J. Nasu, Y. Motome, M. Itoh, and Y. Shimizu, arXiv:1810.05379.

[142] Y. Li, S. M. Winter, and R. Valentí, Phys. Rev. Lett. **121**, 247202 (2018).

[143] J. Chaloupka and G. Khaliullin, Phys. Rev. B **94**, 064435 (2016).

[144] P. Lampen-Kelley, S. Rachel, J. Reuther, J.-Q. Yan, A. Banerjee, C. A. Bridges, H. B. Cao, S. E. Nagler, and D. Mandrus, Phys. Rev. B **98**, 100403 (2018).

[145] Y. Kasahara, T. Ohnishi, Y. Mizukami, O. Tanaka, S. Ma, K. Sugii, N. Kurita, H. Tanaka, J. Nasu, Y. Motome, T. Shibauchi, and Y. Matsuda, Nature **559**, 227 (2018).

[146] O. Derzhko, T. Krokhmalskii, and J. Stolze, Journal of Physics A: Mathematical and General **33**, 3063 (2000).

[147] K. Haule, Phys. Rev. B **75**, 155113 (2007).